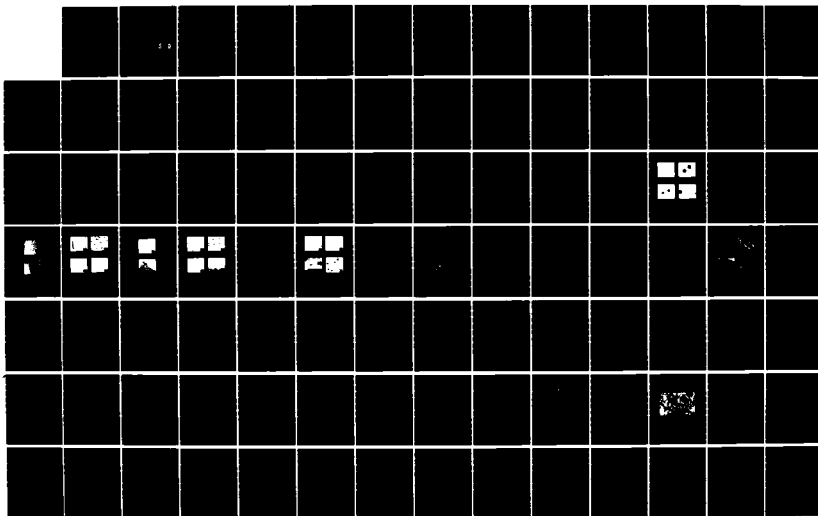
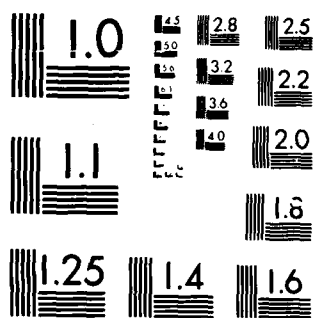


AD-A164 158

SYNTHESIS AND PROPERTIES OF ELEVATED TEMPERATURE P/M
ALUMINUM ALLOYS(U) NORTHWESTERN UNIV EVANSTON IL DEPT 1/2
OF MATERIALS SCIENCE AND E... H E FINE ET AL. 30 NOV 85
UNCLASSIFIED AFOSR-TR-85-1258 AFOSR-82-0005 F/G 11/6 ML





MICROCOPY RESOLUTION TEST CHART
 NATIONAL BUREAU OF STANDARDS 1963-A

UNCLASSIFIED

SECURITY CLASSIFICATION OF THIS PAGE (When Data Entered)

REPORT DOCUMENTATION PAGE.		READ INSTRUCTIONS BEFORE COMPLETING FORM
1. REPORT NUMBER AFOSR-TR- 85-1258	2. GOVT ACCESSION NO.	3. RECIPIENT'S CATALOG NUMBER
4. TITLE (and Subtitle) SYNTHESIS AND PROPERTIES OF ELEVATED TEMPERATURE P/M ALUMINUM ALLOYS	5. TYPE OF REPORT & PERIOD COVERED Final Report 10/1/81 - 9/30/85	
6. AUTHOR(s) Morris E. Fine Julia R. Weertman	7. CONTRACT OR GRANT NUMBER(s) AFOSR-82-0005	
8. PERFORMING ORGANIZATION NAME AND ADDRESS Northwestern University Dept. of Materials Science & Engineering Evanston, Illinois 60201	9. PROGRAM ELEMENT, PROJECT, TASK AREA & WORK UNIT NUMBERS 2306/A1 61102F	
10. CONTROLLING OFFICE NAME AND ADDRESS Air Force Office of Scientific Research Bolling AFB, Building 410 Washington, D. C. 20332	11. REPORT DATE 11/30/85	
12. MONITORING AGENCY NAME & ADDRESS (if different from Controlling Office)	13. NUMBER OF PAGES 110	
	14. SECURITY CLASS. (of this report) Unclassified	
	15. DECLASSIFICATION/DOWNGRADING SCHEDULE	
16. DISTRIBUTION STATEMENT (of this Report) This document has been approved for public release and sale ; its distribution is unlimited		
17. DISTRIBUTION STATEMENT (of the abstract entered in Block 20, if different from Report) DTIC ELECTE FEB 12 1986 S D		
18. SUPPLEMENTARY NOTES		
19. KEY WORDS (Continue on reverse side if necessary and identify by block number) Ostwald ripening (coarsening), aluminum-iron cerium alloy, aluminum- zirconium-vanadium alloy, aluminum-iron-molybdenum-vanadium alloy		
20. ABSTRACT (Continue on reverse side if necessary and identify by block number) The microstructure of the aluminum base-iron-cerium and iron-molybdenum-vanadium alloys, which were developed for use up to 316 degrees centigrade, is not stable at 425 degrees centigrade (three-quarters of the absolute melting temperature of aluminum). Metastable dispersed phases are replaced by stable phases and particles of these coarsen rather rapidly with time. Creep loading accelerates these processes. Trialuminum-zirconium was predicted to be a preferable disper- sed phase for strengthening aluminum for the 425 C temperature range because of good lattice matching with the aluminum matrix giving a low interfacial energy.		

AD-A164 158

DTIC FILE COPY

DD FORM 1 JAN 73 1473 EDITION OF 1 NOV 65 IS OBSOLETE

UNCLASSIFIED

SECURITY CLASSIFICATION OF THIS PAGE (When Data Entered)

86

UNCLASSIFIED

SECURITY CLASSIFICATION OF THIS PAGE(When Data Entered)

> This is true for the thermodynamically stable tetragonal phase but especially true for the metastable cubic phase. Dilute alloys were prepared by arc melting and these were aged to form precipitate dispersed phase. Substitution of vanadium for zirconium improved the lattice parameter matching for both cubic and tetragonal trialuminum-zirconium as well as increasing the stability of the cubic form. The coarsening rates of the particles at 425 C were 100 to 1000 times slower than for the aluminum-iron-cerium or molybdenum alloys, the aluminum-zirconium-vanadium alloy being better than the binary aluminum-zirconium alloy in this respect. These alloys are very promising as the basis for better high temperature aluminum alloys.

UNCLASSIFIED

SECURITY CLASSIFICATION OF THIS PAGE(When Data Entered)

FINAL REPORT

on

SYNTHESIS AND PROPERTIES OF ELEVATED TEMPERATURE
P/M ALUMINUM ALLOYS

covering period

1 October 1981 to 30 September 1985

by

Morris E. Fine and Julia R. Weertman

30 November 1985

This research was supported by the Air Force Office of Scientific
Research, Air Force Systems Command USAF under Grant No. AFOSR-82-0005

DEPARTMENT OF MATERIALS SCIENCE AND ENGINEERING
THE TECHNOLOGICAL INSTITUTE
NORTHWESTERN UNIVERSITY
EVANSTON, ILLINOIS 60201

Approved for public release; distribution unlimited

TABLE OF CONTENTS

	<u>Pg. No.</u>
SUMMARY	1
INTRODUCTION	1
Al base-Zr-V ALLOYS FOR USE AT HIGH TEMPERATURES	6
PARTICLE COARSENING STUDIES OF AN RSP P/M Al-Fe-Ce ALLOY ..	50
EFFECT OF PLASTIC DEFORMATION ON THE COARSENING KINETICS OF DISPERSOIDS IN A RAPIDLY SOLIDIFIED Al-Fe-Ce ALLOY ..	82
LIST OF PROFESSIONAL PERSONNEL	109

AIR FORCE OFFICE OF SCIENTIFIC RESEARCH (AFOSR)

NOTI

THI

ADDS

IS

THI

THI

Accession For	
NTIS CRA&I	<input checked="" type="checkbox"/>
DTIC TAB	<input type="checkbox"/>
Unannounced	<input type="checkbox"/>
Justification	
By	
Distribution	
Availability Codes	
Dist	Avail and/or Special
A-1	

SUMMARY

The microstructure of the aluminum base-iron-cerium and iron-molybdenum-vanadium alloys, which were developed for use up to 316 degrees centigrade, is not stable at 425 degrees centigrade (three-quarters of the absolute melting temperature of aluminum). Metastable dispersed phases are replaced by stable phases and particles of these coarsen rather rapidly with time. Creep loading accelerates these processes.

Trialuminum-zirconium was predicted to be a preferable dispersed phase for strengthening aluminum for the 425 C temperature range because of good lattice matching with the aluminum matrix giving a low interfacial energy. This is true for the thermodynamically stable tetragonal phase but especially true for the metastable cubic phase. Dilute alloys were prepared by arc melting and these were aged to form precipitate dispersed phase. Substitution of vanadium for zirconium improved the lattice parameter matching for both cubic and tetragonal trialuminum-zirconium as well as increasing the stability of the cubic form. The coarsening rates of the particles at 425 C were 100 to 1000 times slower than for the aluminum-iron-cerium or molybdenum alloys, the aluminum-zirconium-vanadium alloy being better than the binary aluminum-zirconium alloy in this respect. These alloys are very promising as the basis for better high temperature aluminum alloys.

INTRODUCTION

The objective of this research was to provide basic data needed to design a high temperature aluminum base alloy useful to the highest possible temperature and to evaluate the stability of some high temperature aluminum base alloys developed in recent years.

By analogy with the dispersion strengthened Ni-base superalloys which are useful to three-quarters of the absolute melting temperature of Ni, one may anticipate development of a dispersion strengthened Al base alloy useful to approximately 425°C or 800°F. For an alloy to be useful at this temperature, its microstructure must be stable even in the presence of fatigue or creep loading. Thus the phases present must resist deleterious transformations and not undergo undue coarsening. If the particle coarsening is bulk diffusion controlled, then the effective average particle radius cubed, \bar{r}^3 , is proportional to $(\sigma DC_0 t)$ where t is time, C_0 is the solubility limit, D is the diffusivity of the rate controlling element, and σ is the interfacial energy between the particle and matrix. Thus the product σDC_0 needs to be small.

Plastic deformation is known to accelerate phase transformations as well as particle coarsening. Thus it is not sufficient to study the stability of the microstructure at elevated temperatures only in the absence of an applied stress. Any microstructural changes due to long time creep or fatigue exposures at high temperature must also be known.

Specifically, the following topics were investigated:

1. The Al-Fe-Ce alloys developed by Alcoa under AFML sponsorship was the subject of the Ph.D. thesis of Lynette Angers (who is now at Alcoa Research Center). The research included phase identification, particle size and shape measurements (after

various aging treatments including creep and fatigue). This alloy is designed for the 316°C range where it has excellent properties but on aging at 425°C metastable phases are replaced by stable phases and these phases coarsen rapidly. The rate is accelerated by creep loading but not by fatigue loading.

2. Similar studies were made on the Al-Fe-Mo-V alloy developed by Pratt & Whitney under AFML sponsorship. These were done by Terence Wilkinson, now at Rexnord-Milwaukee, (M.S. thesis) and Dr. J. L. Horng, now at Materials Research Lab-ITRI, Taiwan, (Postdoctoral and Graduate Research Assistant). The binary Al-Fe system was also included in this study. With the Al-Fe-Mo-V alloy again at 425°C, there was a gradual transformation from a metastable dispersed phase (Al_3Fe) to the stable dispersed phase ($\text{Al}_{13}\text{Fe}_4$). Both probably contain some Mo and V. While the particle coarsening rate of the particles at 425°C is a little slower in the Al-Fe-Mo-V alloy than in the Al-Fe-Ce alloys, it still appears to be too rapid.
3. Because of the similarity of crystal structures between Al and Al_3Zr , this system was selected for study. Addition of V was found to reduce the lattice mismatch between Al_3Zr and Al so that Al-Zr-V ternary alloys were also studied. This was the Ph.D. thesis research of Michael Zedalis, now at Allied Corp. Precipitation of Al_3Zr and $\text{Al}_3(\text{V,Zr})$ in Al and coarsening of the precipitates in dilute alloys were studied. In 2 vol.% Al_3Zr and $\text{Al}_3(\text{V}_{.075}\text{Zr}_{.125})$ alloys, on aging at 425°C, the first phase appearing is a coherent coplanar cubic Ll_2 structured precipitate (γ' in the Ni-base superalloys has the Ll_2 structure). While this phase is metastable, it does not transform on long time aging at 425°C; however, cold working and aging at 600°C converted the precipitate to the tetragonal DO_{23} structure.

Figure 1 compares the particle coarsening rates at 425°C of the Al_3Zr and $\text{Al}_3(\text{V,Zr})$ dispersed Al alloys with those in the Al-Fe-Ce alloy and

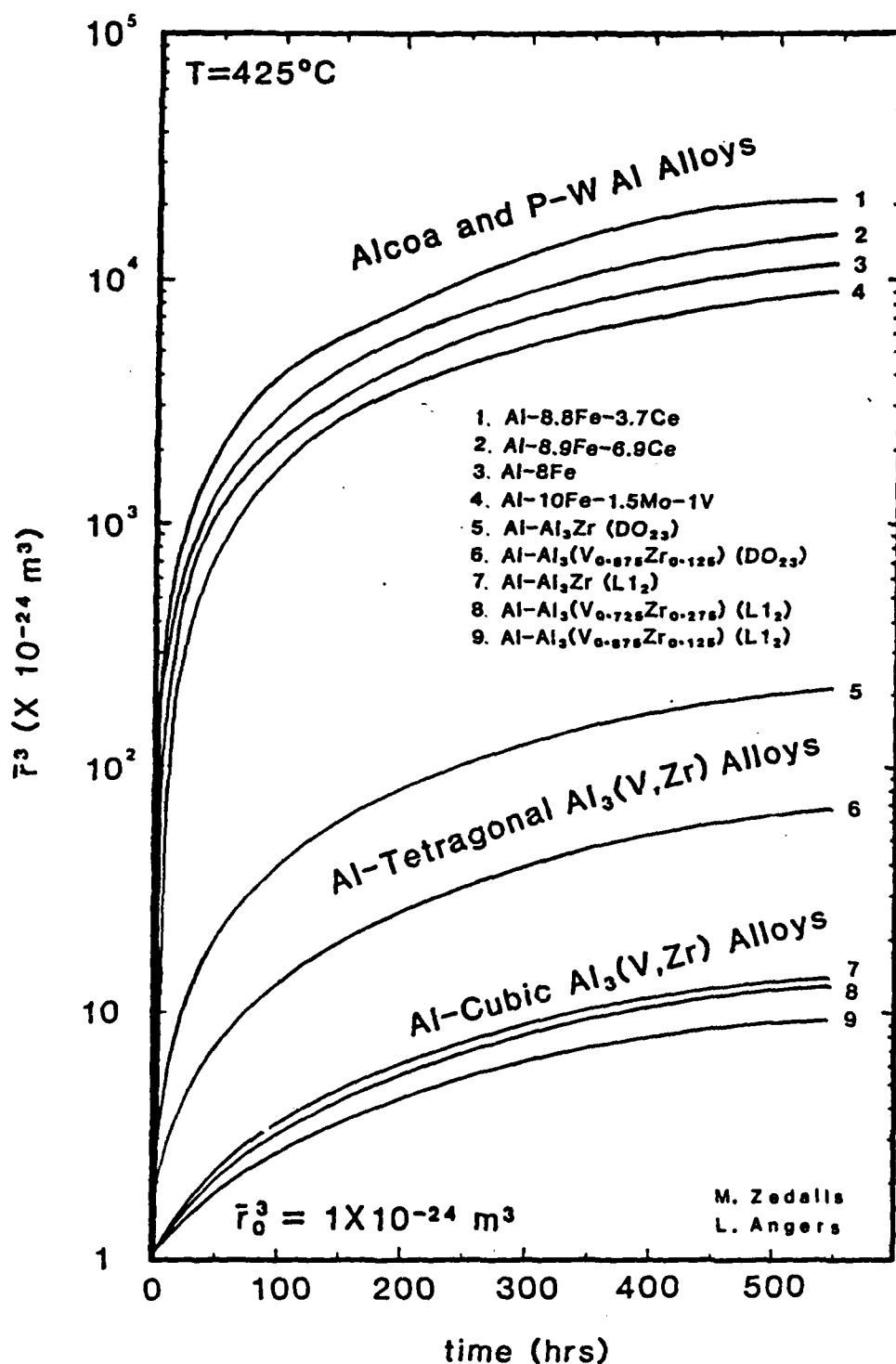


Fig. 1

Comparison of particle coarsening rates for a number of alloys at 425°C . All curves have been corrected to zero volume fraction of dispersed phase using the multiplication factor of Brailsford and Wynblatt.¹⁰ All curves have been shifted so \bar{r}_0 is $1 \times 10^{-8} \text{ m}$. Note the logarithmic scale for \bar{r}^3 .

Al-Fe-Mo-V alloy developed under the AFML high temperature alloy program. A correction has been made for the effect of volume fraction on the coarsening rate following Brailsford and Wynblatt. Plots for both the metastable cubic $L1_2$ structured and the stable tetragonal DO_{23} structured Al_3Zr and $Al_3(V,Zr)$ phases are shown. The very much slower particle coarsening rates for the $Al_3(V,Zr)$ dispersed alloys are evident. While the particle coarsening rates for the fully coherent but metastable $L1_2$ structured $Al_3(V,Zr)$ phases are the slowest of all, the DO_{23} structured $Al_3(V,Zr)$ phase still represents a great improvement over the previously developed alloys. Note that the ordinate is plotted on a log scale. Thus this system is very promising as the basis for development of high temperature Al alloys.

The balance of this report consists of the following papers which have been prepared for submitting to Metallurgical Transactions for publication:

1. Al base-Zr-V Alloys for Use at High Temperatures, M. S. Zedalis and M. E. Fine.
2. Particle Coarsening Studies of an RSP P/M Al-Fe-Ce Alloy, L. Angers, M. E. Fine, and J. R. Weertman.
3. Effect of Plastic Deformation on the Coarsening Kinetics in a Rapidly Solidified Al-Fe-Ce Alloy, L. Angers, M. E. Fine, and J. R. Weertman.

In addition, the following papers have been published and are available in the literature:

1. "Coarsening Rate of θ Precipitates in Al-11Mg Alloy", S. I. Kwun and M. E. Fine, Metall. Trans. 16A, 709 (1985).
2. "Elastic Moduli of Al_3Zr ", M. S. Zedalis, M. V. Ghatge, and M. E. Fine, Scripta Metall. 19, 647 (1985).
3. "Lattice Parameter Variation of $Al_3(Ti,V,Zr,Hf)$ in Al-2 at.% (Ti,V,Zr,Hf) Alloys", M. Zedalis and M. E. Fine, Scripta Metall. 17, 1247 (1983).

4. "Lattice Parameters of $\text{Al}_3(\text{Zr}_x\text{Ti}_{1-x})$ vs. x in Al-2 at.% (Ti+Zr) Alloys", S. Tsunekawa and M. E. Fine, Scripta Metall. 16, 391 (1982).

Al base-Zr-V ALLOYS FOR USE AT HIGH TEMPERATURES

M. S. Zedalis* and M. E. Fine

Department of Materials Science & Engineering and
Materials Research Center, Northwestern University
Evanston, IL 60201 USA

ABSTRACT

The coarsening rates of both cubic and tetragonal Al_3Zr precipitates in Al were measured. The tetragonal Al_3Zr coarsened 16 times faster than the cubic modification in keeping with the fact that the latter is coherent and coplanar with the matrix while the former forms a semicoherent interface with the matrix giving a larger interfacial energy. Partial substitution of V for Zr reduced the precipitate-matrix mismatch for both phases and slowed both coarsening rates as well as retarding the cubic to tetragonal transformation. Reducing strain and interfacial energy no doubt is the origin of this effect. Since the cubic particles are spherical, their volume fraction is small, and the coherency strains are small, this would appear to be an ideal system for testing the Lifshitz-Slyozov-Wagner theory of diffusion controlled Ostwald ripening. While the theory seems to hold, the calculated diffusivity of Zr in Al is much higher than the value reported in the literature. Because of the low coarsening rates of the dispersed particles, the Al-Zr-V system shows promise as the basis for a high temperature Al alloy.

* Present address: Allied Corporation, Metals & Ceramics Laboratory,
Morristown, NJ 07960

I. INTRODUCTION

It seems possible to develop Al-base alloys useful in the temperature range 375-425°C in view of the behavior of the nickel-base alloys which resist degradation of mechanical properties to approximately 75% of their absolute melting temperature. For high temperature Al alloys, the dispersed hardening phase must not undergo phase transformation to an undesirable phase during long time exposure at the temperature of interest. Also, if the lattice disregistry across the precipitate/matrix boundary is small, then strong interfaces with low interfacial energy, σ , are expected to exist. Ostwald ripening or particle coarsening occurs in the later stages of precipitation. The larger precipitate particles grow at the expense of smaller ones with attendant reduction of the total interfacial free energy. Thus low σ is desirable for the particles to resist coarsening. The kinetics of diffusion controlled coarsening were correctly treated for dilute dispersions of spherical particles neglecting strain energy by Lifshitz and Slyozov¹ and Wagner² (LSW theory) who predicted that the average precipitate size should increase in accordance to the relationship

$$\bar{r}^3 - \bar{r}_0^3 = k(t - t_0) \quad (1)$$

where \bar{r} is the average particle radius at time t , \bar{r}_0 is the extrapolated value corresponding to t_0 , and k represents the rate constant given by

$$k = \frac{8\sigma DC_0 V_m^2}{9RT} \quad (2)$$

where D is the diffusivity of the rate-controlling solute, C_0 is the solubility limit of that component in the matrix, ν is the stoichiometric factor and V_m is the molar volume of the dispersed phase. For non-dilute solutions, Eqs.(1) and (2) still hold but with another multiplication factor which increases

with volume fraction.^{3,4} Thus, the ideal dispersed phase should have low interfacial energy, diffusivity and solubility limit, i.e., low σDC_0 , to prevent overaging during long time creep exposure.

Of course, irrespective of the rate controlling mechanism for Ostwald ripening, a reduction in the total interfacial energy drives the process and thus a decrease in σ should slow the ripening rate. A number of intermetallic compounds were suggested by one of the authors⁵ as candidates for elevated temperature Al alloys based on similarities in structure with aluminum. Thus a good possibility of obtaining low values of σ exists. For the Al_3Zr ⁶ and Al_3Ti ^{6,7} tetragonal phases, the lattice mismatches along the a-axis are less than 1% and approximately 5% respectively when compared to Al. It was also suggested⁵ that careful selection of alloying elements could further reduce the mismatch, thereby reducing σ .

In a review article, Adam⁸ subsequently suggested several Al-base systems containing transition elements for potential elevated temperature use based on low reported values of DC_0 with Zr giving the lowest.

The equilibrium structures of Al_3Zr and Al_3Ti are tetragonal, DO_{23} -type and DO_{22} -type crystal structures, respectively.^{6,7} In dilute Al-Zr alloys an intermediate Ll_2 structured cubic phase forms initially on aging of supersaturated solid solutions.⁹

While the mismatch between the a lattice parameters of Al and tetragonal Al_3Zr is slightly less than 1%, the c lattice parameter of Al_3Zr is approximately 4 times a(Al), the actual ratio $c(Al_3Zr)/a(Al)$ being 4.28. It was reasoned that a lower interfacial might result if this ratio were nearer to 4. Substitution of Ti for Zr in $Al_3X(DO_{23})$ was found to reduce this ratio¹⁰, with $c(Al_3Zr_{0.25}Ti_{0.75})/a(Al)$ being 4.20. However, the mismatch in the a parameters increased to 3%. Increasing the Ti fraction beyond 0.75 resulted

in transformation to the DO_{22} structure with poorer overall mismatch. Subsequently¹¹ V and Hf substitution for Zr as well as Ti singly and in combination were investigated. The best overall mismatch with an Al matrix was obtained for an $Al(V_{0.875}Zr_{0.125})$ phase. Substitution of V for Zr was found to have little effect on the mismatch in the a direction while the ratio $c[Al_3(V_{0.875}Zr_{0.125})]/a(Al)$ was reduced to 4.20. This gave an average total mismatch, δ , defined as

$$\delta = \frac{2[a(Al) - a(Al_3X)]}{3a(Al)} + \frac{[c(Al_3X) - 4a(Al)]}{12a(Al)} \quad (3)$$

of 0.0239 compared to 0.0288 for Al_3Zr . Again increasing the V ratio beyond 0.875 resulted in transformation to the DO_{22} -type structure and poorer overall mismatch.

The objective of the present study was to compare the Ostwald ripening kinetics of the metastable cubic (Ll_2) as well as the equilibrium tetragonal (DO_{23}) Al_3Zr and $Al_3(V_{0.875}Zr_{0.125})$ precipitates in dilute Al alloys. The coarsening data are discussed in terms of the LSW theory. Since the metastable phases in each alloy were found to be extremely persistent prior to transformation, the decomposition from the supersaturated solid solutions and transformation were studied. Because of the low rates of Ostwald ripening, both Ll_2 and DO_{23} structured $Al_3(V,Zr)$ dispersed phases show promise for use in elevated temperature Al alloys.

II. EXPERIMENTAL PROCEDURES

As previously^{10,11}, alloys of the compositions shown in Table I were prepared by arc melting 5 gram samples in a gettered argon atmosphere using a tungsten electrode and a water cooled copper cathode crucible. The cooling rate was rapid enough so that dilute supersaturated solid solutions were

produced, i.e., the melting and rapid freezing and cooling served as the solution treatment. The Al was 99.996% pure, the V was Johnson-Mathey spectrochemical grade, and the Zr was cut from a crystal bar prepared by thermal reduction of iodides. Chemical analyses were obtained on alloys 1Z and 1VZ with the analyzed compositions being close to the nominal compositions.

In the binary Al-Zr and Al-V systems the maximum solubilities occur at the peritectic temperatures and are 0.28 wt.% Zr¹² and 0.37 wt.% V¹³, respectively. The alloy concentrations were selected to give approximately 1 vol.% of tetragonal precipitate at the aging temperature of 375°C.

Following aging at 375°C, a combination of cubic ($L1_2$) cellular and spherical precipitates were observed in the Al-Zr alloy. The cellular mode of precipitation was suppressed by cold working prior to aging or by pre-aging for a short time ($\frac{1}{2}$ or 1 hr) at 500°C. To obtain a uniform dispersion of tetragonal (DO_{23}) Al_3Zr precipitates, it was necessary to 95% cold roll the samples and anneal at a 600°C for 50 hrs. For the Al-V-Zr alloy (1VZ) an additional 5% cold rolling and annealing for 50 hrs at 600°C were necessary to completely transform the precipitates to the tetragonal (DO_{23}) structure. Aging of all specimens was carried out in a vacuum of better than 5×10^{-6} torr with the temperature being controlled to $\pm 1^\circ C$. Since quenched in dislocation loops may be confused with coherent spherical precipitates in TEM studies, all specimens were air cooled following aging to prevent formation of such loops.

Foils for TEM examination were prepared by spark machining, mechanically thinning, and finally electropolishing in a solution of 80% CH_3OH - 20% HNO_3 at 95 mA and $-70^\circ C$. The foils were examined in a Hitachi H-700H electron microscope operated at 175 kV. Electron diffraction was used to measure the lattice parameter of the metastable, cubic ($L1_2$) phase simultaneously with the coarsening studies at 425°C. The techniques outlined by Hirsch et al.¹⁴ and

Edington¹⁵ were employed. Working with a well-aligned microscope, selected area diffraction (SAD) patterns were obtained from areas in the matrix containing a relatively large number of precipitates. Once the major zone axis of the crystal and superlattice reflections were identified, the specimens were tilted to obtain a symmetrically intense pattern about the transmitted beam. Since the accuracy of electron diffraction is largely limited by the immediate operating conditions, Al matrix reflections were used as a standard to determine the exact specimen to film distance. After symmetric patterns were recorded, spacings between matrix and superlattice reflections were measured on a densitometer as well as on enlarged images ($\sim 10\times$). For the few cases where Kikuchi lines could be resolved, spacings between these lines were also measured. The expected errors in this study are less than 0.5%.

Particle size measurements were made from dark-field electron micrographs obtained by using superlattice reflections where the particle diameter was taken as the line of no contrast. To obtain average particle sizes and particle size distributions, approximately 400 to 800 particles were measured. The particle size distribution functions, $\sigma^2 h(\rho)$, were empirically calculated according to reference 17,

$$\sigma^2 h(\rho) = \frac{N(r, r+r)}{\sum N(r, r+r)} \frac{\bar{r}}{\Delta r} \frac{9}{4} \quad (4)$$

A basic computer program was written to assist and expedite the analysis of these parameters as well as record the data in formatted plotting files.

To estimate the Zr concentration in the Al solid solution and its effect on the lattice parameter of the Al solid solution at 425°C, x-ray diffraction was performed at that temperature on powder samples of the Al solid solution containing either the metastable, cubic ($L1_2$) Al_3Zr phase or the equilibrium, tetragonal (DO_{22}) Al_3Zr phase. Alloy samples were powdered with an automatic

filing machine, and the fraction passing through a 150-mesh screen ($\sim 100 \mu\text{m}$) was collected for x-ray analysis. To remove any residual stresses incurred during filing, specimens were annealed at 330°C for 4 hrs. The powders were then mixed with silicon powder, which acts as an x-ray peak position standard, and diffraction data were obtained with $\text{CuK}\alpha$ radiation in a Norelco x-ray diffractometer with an attached MRC heating stage. Temperatures were maintained at $425 \pm 10^\circ\text{C}$ while data were being acquired. A continuous x-ray scan was taken to locate the approximate position of both matrix and precipitate peaks and only peak positions corresponding to the higher order planes were analyzed using a 10 second count time in the step scan mode at increments of 0.02° . Interplanar spacing equations were used to calculate the lattice parameters of the Al solid solution. Specimen alignment errors were determined by the lattice parameter calculated for the Si standard and were corrected for by an additive process.

III. RESULTS AND DISCUSSION

A. Solute Concentration in the Al-Zr System Containing the Metastable, Cubic (Ll_2) Al_3Zr Phase

Utilization of the LSW theory of volume diffusion controlled coarsening requires knowledge of the equilibrium solute concentration in the matrix, C_0 . In the Al-Zr system, when there is equilibrium at temperature T with the tetragonal (DO_{23}) phase being present, C_0 may be obtained directly from the equilibrium phase diagram. However, when the metastable, cubic (Ll_2) Al_3Zr phase is present, thermodynamics predicts that the solubility limit in the Al solid solution matrix is greater than that given by the equilibrium phase diagram.

The dissolved Zr concentration in the Al matrix in metastable equilibrium

with cubic Al_3Zr at 425°C was estimated by x-ray diffraction analyses as shown in Fig. 1. The open circle corresponds to the lattice parameter of pure Al at 425°C after correcting for thermal expansion.¹⁸ The closed circle represents the lattice parameter measured for the Al(ss) in equilibrium with the tetragonal Al_3Zr phase at $425 \pm 10^\circ\text{C}$. Thus, based on the lattice parameter measured for the Al(ss) containing the metastable Al_3Zr phase at $425 \pm 10^\circ\text{C}$, it is possible to predict by a Vegard's law extrapolation that the Zr concentration in solution at 425°C is 0.0426 a/o Zr. An appropriate solvus line for the Al solid solution in equilibrium with cubic Al_3Zr may then be drawn predicting, for 375 and 400°C , C_0 values of 0.0380 and 0.0395 at.%, respectively.

B. Lattice Disregistry Between the Al(ss) and Cubic (Ll_2) Al_3Zr and $\text{Al}_3(\text{Zr,V})$ Phases

For measuring the lattice parameter mismatch between the Al(ss) and the cubic $\text{Al}_3(\text{Zr,V})$ precipitates with varying Zr/V ratio, selected area electron diffraction (SAD) patterns were obtained from areas in the matrix containing a relatively high density of particles. Once the major zone axis of the crystal and superlattice reflections were identified, the specimens were tilted slightly to minimize the deviation vector. At this orientation, the Kikuchi lines and first order reflections are coincident and the Bragg condition is uniquely satisfied. Typical SAD patterns are shown in Fig. 2.

The results of the electron diffraction analyses of specimens containing Al_3Zr , $\text{Al}_3(\text{V}_{0.725}\text{Zr}_{0.275})$ and $\text{Al}_3(\text{V}_{0.975}\text{Zr}_{0.125})$ precipitates, isothermally aged at 425°C for various lengths of time are shown in Fig. 3. The horizontal dashed line represents the lattice parameter of Al. The values of δ were determined directly from the differences in spacing of the Ll_2 and matrix spots for long aging times. As shown in Fig. 3, the improved lattice matching previously reported for the equilibrium, tetragonal $\text{Al}_3(\text{V}_{0.975}\text{Zr}_{0.125})$

phase with the Al matrix over the unalloyed $\text{Al}_3\text{Zr}^{11}$ is also found in the respective metastable, cubic (Ll_2) phases.

The value of the Ll_2 Al_3Zr lattice parameter is seen to increase with aging time. This affect was carefully checked to make sure it is not spurious. A similar result for β' NiAl precipitates in Fe-Ni-Al alloys was obtained by H. Calderon (private communication). This effect is not seen with the Al-V-Zr samples where the mismatch is smaller. It might be due to a change in composition of the precipitate with aging or to an increase in imperfection concentration at or near the interface to reduce coherency strain energy.

Assuming Vegard's Law, the lattice parameter variation of cubic $\text{Al}_3(\text{V}_x\text{Zr}_{1-x})$ at various concentrations of x is predicted in Fig. 4. The lattice parameters of cubic (Ll_2) Al_3X -type intermetallic phases may be estimated from the atomic sizes¹⁹ of the elements assuming close packing of hard spheres or the ordered FCC unit cell. For body-centered cubic elements, such as Li, Nb, Ta and V, the atomic radii must be modified by the Goldschmidt factor, i.e., 3% atomic radius expansion on transforming from BCC to FCC crystal structures. The calculated lattice parameters and degrees of registry compared to unalloyed Al, for a number of possible cubic Al_3X -type compounds, are listed in Table 2. The calculated lattice parameter for the cubic Al_3Zr phase in Table 2 is somewhat larger than that measured by electron diffraction (0.431 nm versus 0.410 nm). Of all the compounds listed, only Al_3V has a smaller lattice parameter than Al. Thus V addition to Al_3Zr is predicted to reduce the mismatch with the matrix as already shown to occur in Fig. 4.

C. Isothermal Aging of Al-Zr and Al-V-Zr Supersaturated Solid Solutions at 375°C

The precipitation studies were initially done by isothermally aging alloys 1Z and 22V at 375°C. Neither electron nor light microscopy revealed the presence

of any second phase particles in the as-cast microstructure. As shown in Fig. 5, decomposition from the supersaturated solid solution was observed in both alloys to occur by a discontinuous mode of precipitation, the product being cubic $L1_2$ structured Al_3X and the depleted solid solution. This agrees with previous studies performed on the Al-Zr²⁰⁻²² and Al-Hf²³⁻²⁴ systems. Migrating grain boundaries act as natural sinks for solute atoms and leave cellular precipitates behind in their wakes. Even following 300 hrs of aging at 375°C, selected area electron diffraction revealed that the precipitates remained cubic ($L1_2$) in structure with no evidence of the DO_{19} structure.

D. Decomposition of the Al-Zr and Al-V-Zr Solid Solutions on Isothermal Aging at 450°C after 95% Cold Rolling

To eliminate discontinuous precipitation and accelerate the precipitation process, a second set of samples were initially cold rolled 95% prior to isothermal aging at 450°C. Cold rolling was found to enhance the kinetics of decomposition of the dilute Al-Zr solid solution from that previously reported^{9,21-24} for aging at 450°C. This also occurred for the Al-V-Zr supersaturated solid solution. Again, neither optical nor electron microscopy revealed the presence of any particles in the as-cast and rolled samples. In the Al-Zr alloy following 0.5 hrs of aging at 450°C, spherical, approximately 15 nm $L1_2$ particles appeared in a rather inhomogeneous distribution throughout the matrix. They were typically associated with dislocations and subgrain boundaries. Following 5 hrs aging, spherical Al_3Zr particles were often seen connected by dislocations, Fig. 6a. Such connecting dislocations may act as conduits for solute diffusion and may assist in the coalescence of spherical precipitates and formation of rod-shaped precipitates such as seen in Fig. 6b. Numerous models have been proposed to explain the formation of these rods; however, weak beam-dark field micrographs, Fig. 6c, support the model proposed by Nes.² Here, precipitation on a dislocation associated with helical climb

appears to be responsible for the formation of these rod-shaped precipitates. Furthermore, the associated interfacial dislocation network and the absence of matrix strain contrast are indicative of a precipitate which is semi-coherent.

The present results thus support both models proposed independently, for the formation of rod-shaped $L1_2$ precipitates (not the "fan-shaped" cellular decomposition product). Izumi and Oelschlagel^{21,22} proposed that the formation of rod-shaped precipitates are a result of coalescence of particles. Some rod-shaped precipitates shown in Fig. 6b appear to be the direct result of coalescence. As predicted by the Gibbs-Thomson-Fruendlich equation, the small radii of curvature at the neck of coalesced precipitates will rapidly increase eventually resulting in the formation of a well defined rod-shaped precipitate particle. As already mentioned, precipitation on a dislocation associated with helical climb is seen in Fig. 6c. Through the generation of vacancies, such helical dislocations wrapped around the precipitate may promote a preferential growth direction as well as enhance the growth kinetics by sweeping up nearby solute atoms with their wandering tails with subsequent rapid pipe diffusion.

The first appearance of the equilibrium, tetragonal Al_3Zr phase was observed after 15 hrs of aging at 450°C. After 20 hrs. of aging, the DO_{23} precipitates were platelike with faceted caps, Fig. 6d, and in some cases demonstrated an orientation within the Al matrix identical to that found by Izumi and Oelschlagel²¹, i.e.,

$$\langle 001 \rangle_{Al_3Zr} // \langle 001 \rangle_{Al} \qquad (100)_{Al_3Zr} // (100)_{Al}$$

Following 50 hrs of aging (data not shown), the major axes of some of the tetragonal particles were observed to also lie along $[111]$ directions.

An identical study was performed on the Al-V-Zr alloy containing the $Al_3(V_{0.875}Zr_{0.125})$ phase. Though the overall sequence of decomposition was

identical to that observed for the unalloyed Al_3Zr phase, the kinetics were appreciably more sluggish. For the cubic $\text{Al}_3(\text{V}_{0.875}\text{Zr}_{0.125})$ phase coalescence and the formation of rod-shaped precipitates was not observed until after 20 hrs of aging at 450°C (Fig. 7a). This is in comparison to 13.5 hrs of aging for the binary Al-Zr alloy. The tetragonal phase was not observed until after 100 hrs of aging (Fig. 7b) compared to 15 hrs for the binary alloy.

The present results thus show that reducing the lattice disregistry decreases the decomposition kinetics (or increases the stability) of cubic Ll_2 particles. The cubic Al_3Zr and $\text{Al}_3(\text{V}_{0.875}\text{Zr}_{0.125})$ precipitates have mismatches of approximately $1.0 \pm 0.2\%$ and $-0.1 \pm 0.2\%$, respectively.

The increased stability of the metastable cubic (Ll_2) $\text{Al}_3(\text{V}_{0.875}\text{Zr}_{0.125})$ precipitates versus the cubic Al_3Zr precipitates are attributable to reduced matrix/precipitate strain energy and/or lower interfacial energy. The presence of strain energy or interfacial dislocations will increase the total free energy of the system and make it more unstable.

For the cubic Al_3Zr particles, the average particle radius approaches 16 nm prior to the initial observance of the equilibrium, tetragonal phase; however, this average radius is approximately 20 nm for the $\text{Al}_3(\text{V}_{0.875}\text{Zr}_{0.125})$ particles. As subsequently described, since the growth rate of the latter is slower, this corresponds to a much longer transformation initiation time.

E. Decomposition of the Al-Zr Supersaturated Solid Solution: 95% Cold Rolled and Isothermally Aged at 600°C

With Al-Zr specimens initially cold rolled 95% and isothermally aged at 600°C , copious precipitation was observed almost immediately in the form of small, approximately 10 nm spherical Ll_2 type particles. Following 12 hrs of aging at 600°C , some of the particles were observed to be lenticular in shape and oriented along $[110]$ directions (Fig. 8a). It is apparent that these lenticular particles are growing at a faster rate than the smaller spherical

particles. Weak beam-dark field imaging revealed a strong interaction between such particles and glissile dislocations. Sharp lines of no-contrast are observed in some of the precipitates and thought to be antiphase domain boundaries (APB), Figs. 8a and c. The authors were not able to identify the crystal structure of these lenticular precipitates; however, the appearance of such a sharp line of no contrast is similar to the APB's observed in AuCu_3 specimens²⁵ supporting Ryum's model for the transformation from the cubic (Ll_2) phase to an imperfect tetragonal (DO_{23}) phase by the formation of an APB with a displacement vector $R = a/2 [110]$ on $\{100\}$ type planes.²⁶

An imperfect DO_{23} -type crystal structure may be formed from an Ll_2 -type structure by an atomic displacement of $a/2 [110]$ on particular (001) planes of the Ll_2 lattice.²⁷ Based on the analysis by Weatherly²⁸ of the formation of APB's in Al-Cu alloys, it was concluded that precipitate coalescence and precipitate/dislocation interaction are two modes of forming an antiphase domain boundary in a precipitate. An APB may be formed if glissile dislocations in the matrix have sufficient enough energy to cut through the precipitate. Since a transformation occurs which lowers the free energy, then negative energy is required for this cutting. Weak beam-dark field imaging, Fig. 6, appears to show a dislocation actually cutting a large lenticular Ll_2 particle.

With continued aging, Fig. 8d, all of the particles were observed to become lenticular in shape prior to forming the equilibrium tetragonal structure, as verified by electron diffraction.

F. Coarsening Kinetics of the Cubic (Ll_2) Al_3Zr and $\text{Al}_3(\text{V,Zr})$ Precipitates

The coarsening kinetics of the binary cubic (Ll_2) Al_3Zr precipitates isothermally aged at 375°C, 400°C and 425°C are shown in Fig. 9. Particles associated with dislocations were not included in the analyses. The particle sizes for short aging times are, of course, dependent on the prior treatment.

As predicted by the LSW theory of VDC coarsening, a linear relationship between the cube of the average particle radius and time is more or less obtained at all temperatures investigated. Through a least squares analysis, the coarsening rates k in Eq. (1) and the coefficient of linearity were calculated and are reported in Table III. Typical micrographs at various aging times and temperatures are shown in Fig. 10.

Some particle size distributions (PSD) for the cubic Al_3Zr precipitates at each temperature investigated are given in Fig. 11. At least 500 particles were measured for each distribution curve. The solid line in each figure represents the "quasi-steady-state" distribution predicted by the LSW theory of Ostwald ripening and given by the function

$$f(r,t) = g(t) \rho^2 h(\rho) \quad (5)$$

where $g(t)$ is a function of time only, $\rho = r/\bar{r}$ and $h(\rho)$ is given by

$$h(\rho) = \left[\frac{3}{(\rho + 3)} \right]^{7/3} \left[\frac{-3/2}{(\rho - 3/2)} \right]^{11/3} \exp\left[\rho / (\rho - 3/2) \right] \quad (6)$$

when $\rho < 3/2$; $h(\rho) = 0$ when $\rho \geq 3/2$.

Of the distributions shown, only that for 200 hrs at 375°C obeys the LSW distribution function which predicts a rapid drop off in number of particles at sizes greater than the most probably size. The others (such as 400 hrs at 425°C) have more symmetrical distributions; however, the distribution for 400 hrs at 400°C is askew in the opposite sense.

The coarsening kinetics of the cubic (Ll_2) $\text{Al}_3(\text{V}_{0.875}\text{Zr}_{0.125})$ phase isothermally aged at 425°C is also shown in Fig. 9. Table III also gives the calculated coarsening rate constants and values of the coefficient of linearity. Typical micrographs of the cubic $\text{Al}_3(\text{V}_{0.875}\text{Zr}_{0.125})$ phase at various times during aging are shown in Fig. 12 and some measured particle size distributions are given in Fig. 13.

In keeping with the lower mismatch, the coarsening rate for the cubic $\text{Al}_3(\text{V}_{0.275}\text{Zr}_{0.125})$ precipitates is slower than for Al_3Zr . Again, the distributions shown do not obey the LSW distribution function even though there is a reasonable fit of the \bar{r}^3 versus t data to a straight line.

In an effort to reach a later stage of aging to see if the LSW size distribution was achieved, a sample with $\text{Al}_3(\text{V}_{0.725}\text{Zr}_{0.275})$ particles was pre-aged for 1 hr at 500°C prior to aging at 425°C . As shown in Fig. 14, there does seem to be good agreement with predictions of the LSW theory. The rate constant determined from straight line drawn through the \bar{r}^3 versus t data plot was $2.26 \times 10^{-26} \text{ m}^3/\text{hr}$ with a coefficient of linearity of 0.99. The rate constant is intermediate between that for cubic Al_3Zr and $\text{Al}_3(\text{V}_{0.975}\text{Zr}_{0.125})$ in keeping with the intermediate value of mismatch.

G. Temperature Dependence of Ostwald Ripening

The coarsening rate constant, k , predicted by the LSW theory of VDC coarsening is given by the expanded expression

$$k = \frac{8\sigma C_o V_m^2 D_o \exp(-Q/RT)}{9\sqrt{RT}} \quad (7)$$

Rearranging terms and taking logarithms gives the linear equation

$$\ln(KT/C_o) = \ln A - (Q/RT) \quad (8)$$

where $\ln A$ is the y-intercept given by

$$\ln A = \ln (8/9)(\sigma D_o V_m^2)/(\sqrt{RT}) \quad (9)$$

Thus, from a plot of $\ln(KT/C_o)$ versus $1/T$, assuming A is constant, it is possible to empirically determine the activation energy, Q , for Zr diffusion in the Al matrix if the diffusion of Zr is indeed controlling coarsening. The value of the activation energy for Al diffusion in the Ni-base systems determined in this manner by Ardell and Nicholson¹⁷ was found to be in excellent

agreement with the value of activation energy determined by conventional methods.

By the radiotracer technique²⁸, values for D_0 and Q of $7.28 \times 10^4 \text{ mm}^2/\text{sec}$ and 242 KJ/mole, respectively, were determined for the diffusivity of Zr in Al. However, recent measurements²⁹ of the decomposition of supersaturated Al-Zr solid solutions indicate that diffusion of Zr in Al occurs at a much faster rate than predicted. Jones²⁹ suggested values of D_0 and Q of approximately $30 \text{ mm}^2/\text{sec}$ and 186 KJ/mole, respectively. Recently, Hori et al.³⁰ investigated the early growth rates of Al_3Zr precipitates in Al-0.22 w/o Zr alloys and proposed an activation energy of approximately 217 KJ/mole.

A plot of $\ln(KT/C_0)$ versus $1/T$, corresponding to the coarsening rates measured for the cubic (Ll_2) Al_3Zr particles at 375°C, 400°C and 425°C, is shown in Fig. 15. From a least squares analysis, an effective activation energy for Zr diffusion in the Al matrix was calculated to be 221.5 KJ/mole. This is close to the value determined by Hori et al. Since particles near grain boundaries or dislocations were not counted, such accelerated coarsening of particles is not thought to be the origin of the difference between the present value and the radiotracer Q for diffusion of Zr in Al.

H. Calculation of the Effective Interfacial Energies

Since the Al-Zr alloy studied is dilute and the particles are spherical, an accurate calculation of the interfacial energy between Al_3Zr and the Al from the LSW equation for VDC was anticipated. Assuming the radiotracer measured D at 640°C is accurate but assuming the correct value of Q is 221.5 KJ/mole, a D_0 of $5400 \text{ mm}^2/\text{sec}$ is computed. This gives D_{Zr} at 425°C of $1.4 \times 10^{-13} \text{ m}^2/\text{sec}$. With C_0 of 43 moles Zr/ m^3 and V_m of $4.13 \times 10^{-5} \text{ m}^3/\text{mole}$ and taking Wagner's stoichiometric factor $\nu = 1$, an interfacial energy of 4 J/ m^2 is calculated. This is a hundred times larger or more than expected for

the interfacial energy between the coherent cubic Al_3Zr and the Al matrix. If the radiotracer Q is used to determine D at 425°C , the agreement is even worse. Similar studies on Ni-base alloys^{17,31,32} and Fe-Ni-Al alloys^{33,34} where similar coherent precipitates form have yielded σ values of 0.01 to 0.03 J/m^2 . We are not able to explain this discrepancy at this time. Ostwald ripening occurs much more rapidly than predicted. One suggestion is that there is a gross error in the radiotracer determination of D. Accelerated diffusion due to imperfections is not thought to be the source of the discrepancy since 95% cold rolling prior to aging at 450°C was found to increase the rate constant by only a factor of two.

Reducing the mismatch and thus σ by adding V does, however, reduce the coarsening rate in keeping with the predictions of the LSW theory but, of course, since Ostwald ripening is driven by reduction in total surface energy any theory for Ostwald ripening must make the same prediction.

I. Coarsening Kinetics of Tetragonal Al_3Zr and $\text{Al}_3(\text{V}_{0.875}\text{Zr}_{0.125})$ Precipitates

The coarsening kinetics of the tetragonal (DO_{23}) Al_3Zr and $\text{Al}_3(\text{V}_{0.875}\text{Zr}_{0.125})$ precipitates isothermally aged at 425°C after cold working and aging at 600°C are shown in Fig. 16. Typical microstructures after 20 and 400 hrs of aging are shown in Fig. 17. Since the tetragonal (DO_{23}) Al_3Zr platelets have been observed^{9,21} to have $\{100\}$ habit planes, TEM foils were tilted, whenever possible, to obtain a $\langle 001 \rangle$ zone axis. For the tetragonal plates, one half of the particle's width cubed, r^3 , is plotted versus time. The larger extrapolated initial particles size for the $\text{Al}_3(\text{V}_{0.875}\text{Zr}_{0.125})$ phase is the result of the double preaging treatment employed to obtain a homogeneous dispersion of tetragonal precipitates.

The tetragonal (DO_{23}) $\text{Al}_3(\text{V}_{0.875}\text{Zr}_{0.125})$ particles coarsen in volume three times more slowly at 425°C than the (DO_{22}) Al_3Zr particles. This is most likely

due to a reduction in overall mismatch (Eq.3) from 2.8 to 2.4% with a resulting reduction in the average interfacial energy of the particles. At 425°C, the tetragonal (DO_{23}) Al_3Zr phase coarsens in volume 16 times faster than cubic (LL_2) Al_3Zr phase while tetragonal $\text{Al}_3(\text{V}_{0.875}\text{Zr}_{0.125})$ phase coarsens 8 times faster than cubic $\text{Al}_3(\text{V}_{0.875}\text{Zr}_{0.125})$ phase. These differences between the cubic (LL_2) and tetragonal (DO_{23}) particle coarsening rates are most certainly related to the higher average interfacial energies for the tetragonal particles.

Normalized experimental histograms of particle widths for each of the tetragonal phases at 20 and 200 hrs are shown in Figs. 18a-d. For comparison, the steady state particle size distribution, $\rho^2 h(\rho)$, predicted by the LSW theory of VDC coarsening is included. As may be observed, an opposite skewness and particle sizes much larger than the predicted maximum size were found. Similar disparities in the experimental histograms determined for other metallic systems containing nonspherical precipitates have been observed.³⁵⁻³⁸ Presently, no theoretical treatments are available which adequately treat diffusion controlled coarsening of nonspherical particles. In addition, an interface mechanism control of coarsening must be considered for the DO_{23} platelets. Thus based on the present results, we are not able to determine the rate controlling mechanism for Ostwald ripening of the tetragonal (DO_{23}) phase particles. While straight lines for an r^3 versus t relationship may be drawn through the data, essentially similar agreement may be obtained between r^2 and t . Thus, Fig. 16 may not be taken as proof for the LSW theory of volume diffusion controlled coarsening (VDC) for this case.

There were no major changes in the average aspect ratios of the particles, i.e., average width to length ratio. For the tetragonal Al_3Zr phase, this varied from 5.1 for 50 hrs of aging to 4.7 for 405 hrs of aging. Similarly,

the average aspect ratio of the tetragonal $\text{Al}_3(\text{V}_{0.875}\text{Zr}_{0.125})$ particles varied from 2.9 for 50 hrs of aging to 2.4 for 400 hrs of aging. Since the particles are thickening and lengthening at about the same rate, the ledge growth mechanism proposed for the shape coarsening of θ' particles in Al-Cu alloys proposed by Merle and Fouquet^{36,37} does not occur in the present system.

IV. FINAL DISCUSSION

Whether or not volume diffusion controls the rate of Ostwald ripening, reduction in the interfacial energy between the particles and matrix should reduce the ripening rate. This was borne out by the experimental results. Substituting vanadium for most of the zirconium reduced the mismatch between the cubic (Ll_2) Al_3X phase and the matrix as well as the mismatch between the tetragonal (DO_{23}) Al_3X phase and the matrix. In both cases slower Ostwald ripening resulted. Further, the transformation of the Ll_2 to the DO_{23} phase was much more sluggish in the Al-V-Zr alloy. The free energy change for the reaction $\alpha_{\text{Co}} + \text{Ll}_2 \rightarrow \alpha_{\text{Co}} + \text{DO}_{23}$ was reduced due to reduction in strain and interfacial energy. This is a very important principle which has consequences in other systems.

For Ostwald ripening of cubic Al_3Zr and cubic $\text{Al}_3(\text{V}_{0.975}\text{Zr}_{0.125})$, VDC coarsening is proposed to be the rate controlling process even though calculations of the interfacial energy from the LSW theory are much too high. If the diffusivity of Zr is actually close to that for V or Fe in Al^β , then a very reasonable predicted value for σ would result.

Finally, does better lattice matching between the dispersed phase and matrix possibly lead to a better high temperature alloy? Of course, extensive dispersed phase coarsening at the temperature of application possibly accelerated by creep or fatigue deformation would lead to overaging and reduction in

strength and also possibly ductility. Thus a reduced particle coarsening rate is desirable. It is of interest to compare the present Al-Zr and Al-Zr-V alloys to a binary Al-Fe alloy. Presently, the Al-Fe system is the basis for development of a new series of high temperature Al alloys. The equilibrium dispersed phase in these systems at 425°C is Al_3Fe which is incoherent with the matrix. In an Al-8 w/o Fe alloy* the coarsening rate at 425°C, corrected to 1% volume fraction of dispersed phase⁴, is 50 times faster than even tetragonal $\text{DO}_{23} \text{Al}_3\text{Zr}$. Thus the cubic (Ll_2) and tetragonal (DO_{23}) Al_3X phase suitably alloyed to give good matching with the lattice parameter of the matrix are very promising as the basis for improved high temperature Al base alloys.

ACKNOWLEDGEMENTS

The authors are pleased to acknowledge the support of the Air Force Office of Scientific Research, USAF, under Grant No. AFOSR 82-0005B. The use of the Central Facilities of Northwestern University's Materials Research Center sponsored under the NSF-MRL program (Grant No. DMR82-16972) is greatly appreciated. Profs. M. Meshii and J. B. Cohen gave much assistance with the electron microscopy and x-ray diffraction, respectively. The authors acknowledge very helpful discussions with Prof. Julia R. Weertman, Dr. Lynette Angers, Dr. Hector Calderon and Mr. In-Bae Kwon in our research group. Dr. Colin Adam, Allied Corporation, gave helpful advice.

* This alloy, furnished by Alcoa Technical Center, was prepared by forging rapidly solidified powders. The coarsening rates were determined at Northwestern by Dr. Jain-Long Horng and Dr. Lynette Angers.

REFERENCES

1. I. M. Lifshitz and V. V. Slyozov: J. Phys. Chem. Solids, 1961, vol. 19, p. 35.
2. C. Wagner: Z. Elektrochem., 1961, vol. 65, p. 581.
3. P. W. Voorhees and M. E. Glicksman: Metall. Trans. A, 1984, vol. 15A, p. 1081.
4. A. D. Brailsford and P. Wynblatt: Acta Metall., 1979, vol. 27, p. 489.
5. M. E. Fine: Metall. Trans. A, 1975, vol. 6A, p. 625.
6. G. Brauer: Z. anorg. ally. Chem., 1939, vol. 242, p. 1.
7. F. J. J. van Loo and G. D. Rieck: Acta Metall., 1973, vol. 21, p. 61.
8. C. M. Adam: in Rapidly Solidified Amorphous and Crystalline Alloys, B. H. Kear, B. C. Giessen and M. Cohen, eds., Elsevier Science Pub. Co., Inc., 1982, pp. 411-422.
9. E. Nes: Acta Metall., 1972, vol. 20, p. 499.
10. S. Tsunekawa and M. E. Fine: Scr. Metall., 1982, vol. 16, p. 391.
11. M. Zedalis and M. E. Fine: Scr. Metall., 1983, vol. 17, p. 1247.
12. D. J. McPherson and M. Hansen: Trans. ASM, 1954, vol. 46, p. 354.
13. A. Roth: Z. Metallkunde, 1940, vol. 32, p. 356.
14. P. Hirsch, A. Howie, R. B. Nicholson, D. W. Pashley and M. J. Whalen: in Electron Microscopy of Thin Crystals, Robert E. Krieger Pub. Co., Inc., New York, 1977, pp. 124-128.
15. J. W. Edington: in Practical Electron Microscopy in Materials Science, Von Nostrand Reinhold Co., New York, 1976, pp. 83-84.
16. D. J. H. Cockayne, I. L. F. Ray and M. J. Whelan: Phil. Mag., 1969, vol. 20, p. 1265.
17. A. J. Ardell and R. B. Nicholson: J. Phys. Chem. Solids, 1966, vol. 27, p. 1793.
18. L. A. Willey, Alcoa Research Labs, 1957, cited in Aluminum, vol. I, 1967.
19. N. F. M. Henry and K. Lonsdale: in International Tables for X-ray Crystallography, 1952, vol. 1, pp. 79-90.
20. E. Nes and N. Ryum: Scr. Metall., 1971, vol. 5, p. 987.

21. N. Ryum: *Acta Metall.*, 1969, vol. 17, p. 269.
22. O. Izumi and D. Oelschlagel: *Scr. Metall.*, 1969, vol. 3, p. 619.
23. M. Sundberg, R. Sundberg and B. Jacobson: *Jernkontoret Ann.*, 1971, vol. 155, p. 1.
24. E. Nes and H. Billdal: *Acta Metall.*, 1977, vol. 25, p. 1031.
25. R. M. Fisher and M. J. Marcinkowski: *Phil. Mag.*, 1960, Ser. 8, vol. 8, p. 1385.
26. N. Ryum: *J. Mat. Sci.*, 1975, vol. 10, p. 2075.
27. P. A. Flinn: *Trans. TMS-AIME*, 1960, vol. 218, p. 145.
28. T. Marumo, S. Fujikawa and Ken-ichi Hirano: *J. Japan Inst. Light Metals*, 1973, vol. 23, No. 1, p. 17.
29. H. Jones: in Rapid Solidification Processing - Principles and Technologies II, R. Mehrabian, B. H. Kear and M. Cohen, eds., Claitor's Pub. Div., Baton Rouge, La., 1980, pp. 306-316.
30. S. Hori, S. Saji and T. Kobayashi: in *Technol. Report*, Osaka University, 1978, vol. 28, p. 359.
31. A. J. Ardell: *Acta Metall.*, 1968, vol. 16, p. 511.
32. P. K. Rastaogi and A. J. Ardell: *Acta Metall.*, 1971, vol. 19, p. 321.
33. H. Calderon and M. E. Fine: *Mat. Sci. Eng.*, 1984, vol. 63, p. 197.
34. H. A. Calderon, J. R. Weertman and M. E. Fine: *Scr. Metall.*, 1984, vol. 18, p. 587.
35. J. D. Boyd and R. B. Nicholson: *Acta Metall.*, 1971, vol. 19, p. 1379.
36. P. Merle and F. Fouquet: *Acta Metall.*, 1981, vol. 29, p. 1919.
37. P. Merle and F. Fouquet: *Acta Metall.*, 1981, vol. 29, p. 1929.
38. D. Janoff and M. E. Fine: *Mat. Sci. Eng.*, 1984, vol. 64, p. 67.

Table I. Compositions of Alloys.

Alloy	Nominal		Analyzed	
	Weight	Percent	Weight	Percent
	Zr	V	Zr	V
1Z	0.75	-	0.79	0.00
1VZ	0.10	0.40	0.10	0.35
2VZ	0.23	0.34	-	-

Table II. Estimated Lattice Parameter and Disregistry of Cubic (Li_2) Al_3 X-Phases Compared to the Lattice Parameter of Al.

Element	Atomic Radius ¹⁹ (nm)**	Calculated Lattice Parameter	Calculated Lattice
		a, Al_3 X-type (nm)	Disregistry (%)***
Li*	0.157	0.424	4.67
Hf	0.156	0.426	5.29
Nb*	0.147	0.411	1.50
Ta*	0.147	0.410	1.37
Ti	0.145	0.407	0.57
V*	0.135	0.393	-2.91
Zr	0.162	0.431	6.42
Y	0.178	0.454	12.00

* refers to BCC elements whose atomic radii have been modified by the Goldschmidt Factor, i.e., 3% atomic radii expansion in BCC to FCC crystal morphology change.

** Atomic radius is equal to one-half of the interatomic distance.

*** Lattice disregistry calculated from $100(a_z - a_0)/a_0$, where a_z is the lattice parameter of the Al_3 X-type phase and a_0 is the lattice parameter of pure Al.

Table III. Measured Coarsening Rate Constants and Coefficients of Linearity for the Cubic (Li_2) Particles Aged at 375°C, 400°C and 425°C.

Cubic Phase	Temperature (°C)	Mismatch (δ)	Measured Volume	Coefficient of Linearity
			Coarsening Rate Constant (m^3/hr)	
Al_3Zr	375*	1.0	1.22×10^{-27}	0.92
Al_3Zr	400*	1.0	7.50×10^{-27}	0.99
Al_3Zr	425	1.0	2.49×10^{-28}	0.97
$Al_3(V_{0.9-5}Zr_{0.125})$	425	-0.1	1.63×10^{-28}	0.99
$Al_3(V_{0.2-25}Zr_{0.275})$	425**	0.46	2.26×10^{-28}	0.99

* Preaged for 0.5 hrs at 500°C prior to isothermal aging.

** Preaged for 1 hr at 500°C prior to isothermal aging.

FIGURE CAPTIONS

- Figure 1. Variation of lattice parameter of Al solid solution with Zr content. The horizontal dashed line is the lattice parameter for the Al(ss) in metastable equilibrium with cubic Al_3Zr which predicts by extrapolation a solubility limit of 0.0426 at.% Zr in Al at 425°C.
- Figure 2. Typical selected area electron diffraction patterns from cubic Ll_2 structures a) Al_3Zr , b) $\text{Al}_3(\text{V}_{0.725}\text{Zr}_{0.275})$, c) and d) $\text{Al}_3(\text{V}_{0.875}\text{Zr}_{0.125})$.
- Figure 3. Aging time dependence of the lattice parameters of cubic (Ll_2 - structure) Al_3Zr , $\text{Al}-\text{Al}_3(\text{V}_{0.725}\text{Zr}_{0.125})$, and $\text{Al}_3(\text{V}_{0.875}\text{Zr}_{0.125})$. The aging temperature was 425°C but the lattice parameter measurements were made at room temperature.
- Figure 4. Lattice parameter of cubic Ll_2 $\text{Al}_3(\text{Zr,V})$ versus vanadium concentration expressed as the V/Zr ratio in atom fraction.
- Figure 5. Typical transmission electron microscope micrographs showing discontinuous precipitation of cubic Ll_2 a) Al_3Zr and b) $\text{Al}_3(\text{V}_{0.875}\text{Zr}_{0.125})$ after aging at 375°C for 200 and 50 hrs, respectively.
- Figure 6. TEM micrographs showing stages of precipitation of Al_3Zr at 450°C following 95% cold rolling. Aging times are: a) shows cubic Ll_2 precipitates on dislocations after 5 hrs aging, b) shows an area where general precipitation of the cubic phase occurred after 10 hrs of aging, c) is a weak beam-dark field TEM showing precipitation of the cubic phase on dislocations after 13.5 hrs of aging, d) shows tetragonal DO_{23} Al_3Zr precipitates after 20 hrs of aging.

FIGURE CAPTIONS (continued)

Figure 7. TEM micrographs showing stages of precipitation of $\text{Al}_3(\text{V}_{0.875}\text{Zr}_{0.125})$ at 450°C : a) after 20 hrs of aging shows some rod-shaped as well as spherical cubic Ll_2 precipitates, b) after 100 hrs of aging shows tetragonal DO_{23} precipitates.

Figure 8. TEM micrographs documenting transformation of cubic $\text{Ll}_2 \text{Al}_3\text{Zr}$ to an imperfect tetragonal " DO_{23} " Al_3Zr structure during aging at 600°C after 95% cold rolling. Explanations are in text. a) and b) are after 12 hrs, c) is after 15 hrs and d) is after 25 hrs of aging.

Figure 9. Coarsening kinetics of cubic $\text{Ll}_2 \text{Al}_3\text{Zr}$ precipitates during isothermal aging at 375, 400, and 475°C . \bar{r} is the average particle radius at a particular time t . Specimens aged at 375°C and 400°C were pre-aged at 500°C to eliminate cellular precipitation. It was not necessary to pre-age the specimens aged at 425°C since cellular precipitation was not observed at this aging temperature. Coarsening kinetics of $\text{Al-Al}_3(\text{V}_{0.875}\text{Zr}_{0.125})$ at 425°C is also shown.

Figure 10. TEM micrographs documenting coarsening of cubic $\text{Ll}_2 \text{Al}_3\text{Zr}$ after 20 and 200 hrs of aging at a) and b) 400°C and c) and d) 425°C .

Figure 11. Normalized particle size distributions for cubic Al_3Zr aged for various times at 375, 400, and 425°C . The solid curve shows the predicted LSW distribution. For the 375 and 400°C aging, the specimens were pre-aged 0.5 hrs at 500°C . a) 20 hrs at 375°C , b) 200 hrs at 375°C , c) 200 hrs at 400°C , d) 400 hrs at 400°C , e) 100 hrs at 425°C , f) 400 hrs at 425°C .

Figure 12. TEM micrographs of cubic $\text{Al}_3(\text{V}_{0.875}\text{Zr}_{0.125})$ after aging 20 and 200 hrs at 425°C . The solid curve shows the predicted LSW distribution.

FIGURE CAPTIONS (continued)

Figure 13. Normalized particle size distributions for cubic $\text{Al}_3(\text{V}_{0.875}\text{Zr}_{0.125})$ aged from 1 to 400 hrs at 425°C.

Figure 14. Normalized particle size distributions for cubic $\text{Al}_3(\text{V}_{0.725}\text{Zr}_{0.275})$ aged for 20, 100, and 300 hrs at 425°C. In order to try to achieve a steady distribution, the specimens were pre-aged for 1 hr at 500°C. The solid curve shows the predicted LSW particle size distribution. Note the agreement between measurements and theory is much better than in Fig. 13 where the samples were not pre-aged.

Figure 15. Determination of the activation energy, Q , for the coarsening of cubic Al_3Zr precipitates from a plot of $\ln(KT/C_0)$ vs. $1/T$.

Figure 16. Comparison of volumetric coarsening rate of tetragonal $\text{DO}_{23}\text{Al}_3(\text{V}_{0.875}\text{Zr}_{0.125})$ with Al_3Zr during isothermal aging at 425°C. The particle size \bar{r} is defined as half the average thickness of the plate-like particles across the minor axis of the the image in the micrographs. The Al-Zr alloy was cold rolled 90% and pre-aged 50 hrs at 600°C. The Al-V-Zr alloy was cold rolled an additional 5% and annealed an additional 50 hrs at 600°C to convert it to the DO_{23} phase. Thus at short times particle size is much larger.

Figure 17. TEM micrographs showing tetragonal $\text{DO}_{23}\text{Al}_3\text{Zr}$ (a,b) and $\text{Al}_3(\text{V}_{0.875}\text{Zr}_{0.125})$ (c,d) precipitates after aging 20 (a,c) and 400 (b,d) hrs at 425°C. Pre-treatments are described in caption to Fig. 16.

Figure 18. Particle size distributions for tetragonal Al_3Zr (a,b) and $\text{Al}_3(\text{V}_{0.875}\text{Zr}_{0.125})$ (c,d) aged at 425°C for 20 (a,c) and 400 hrs (b,d). Particle size is defined in the caption for Fig. 16.

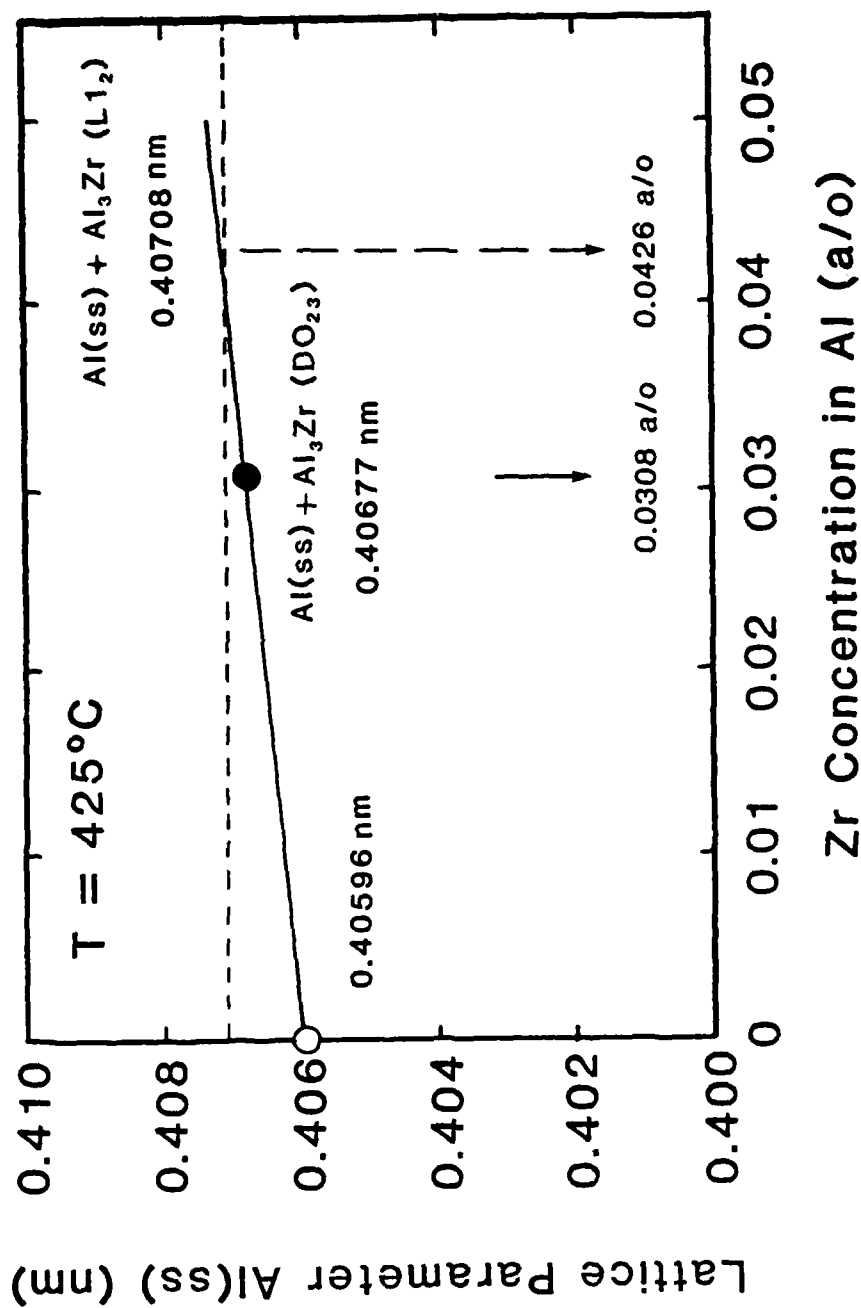
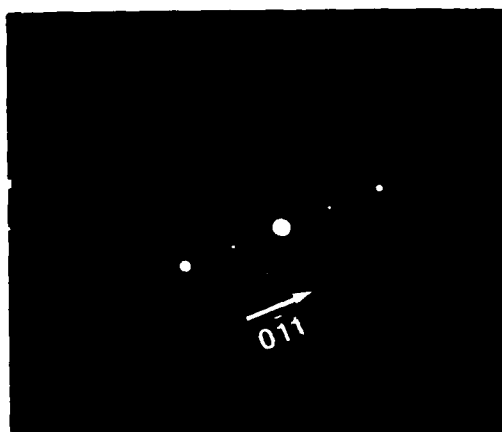
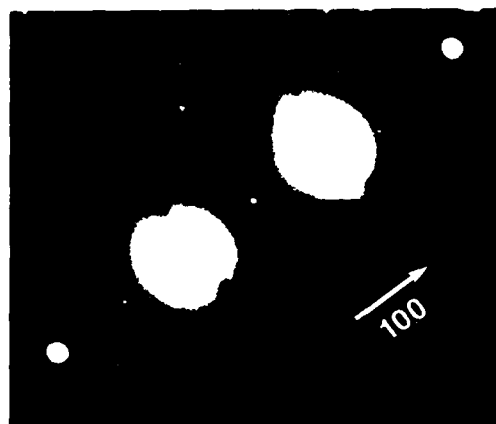


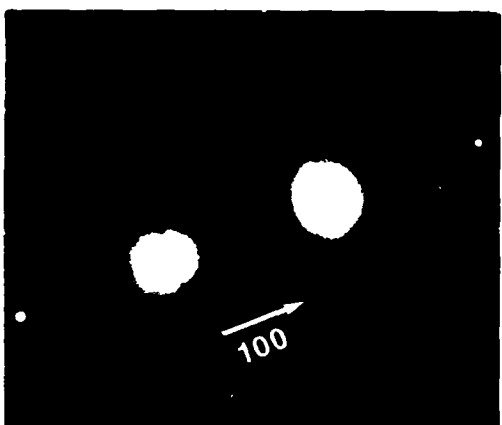
Fig. 1. Variation of lattice parameter of Al solid solution with Zr content. The horizontal dashed line is the lattice parameter for the Al(ss) in metastable equilibrium with cubic Al_3Zr which predicts by extrapolation a solubility limit of 0.0426 at.% Zr in Al at 425°C.



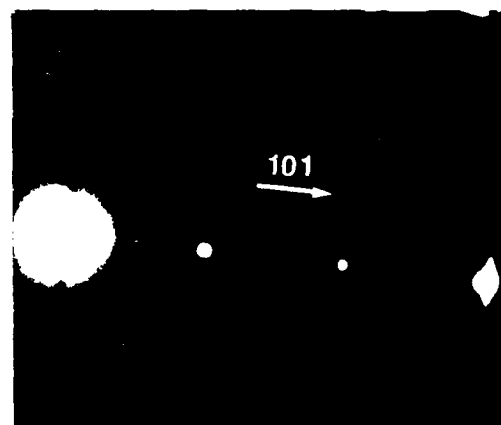
(a)



(b)



(c)



(d)

Fig. 2. Typical selected area electron diffraction patterns from cubic $L1_2$ structures: a) Al_3Zr , b) $Al_3(V_{0.725}Zr_{0.275})$, c) and d) $Al_3(V_{0.875}Zr_{0.125})$.

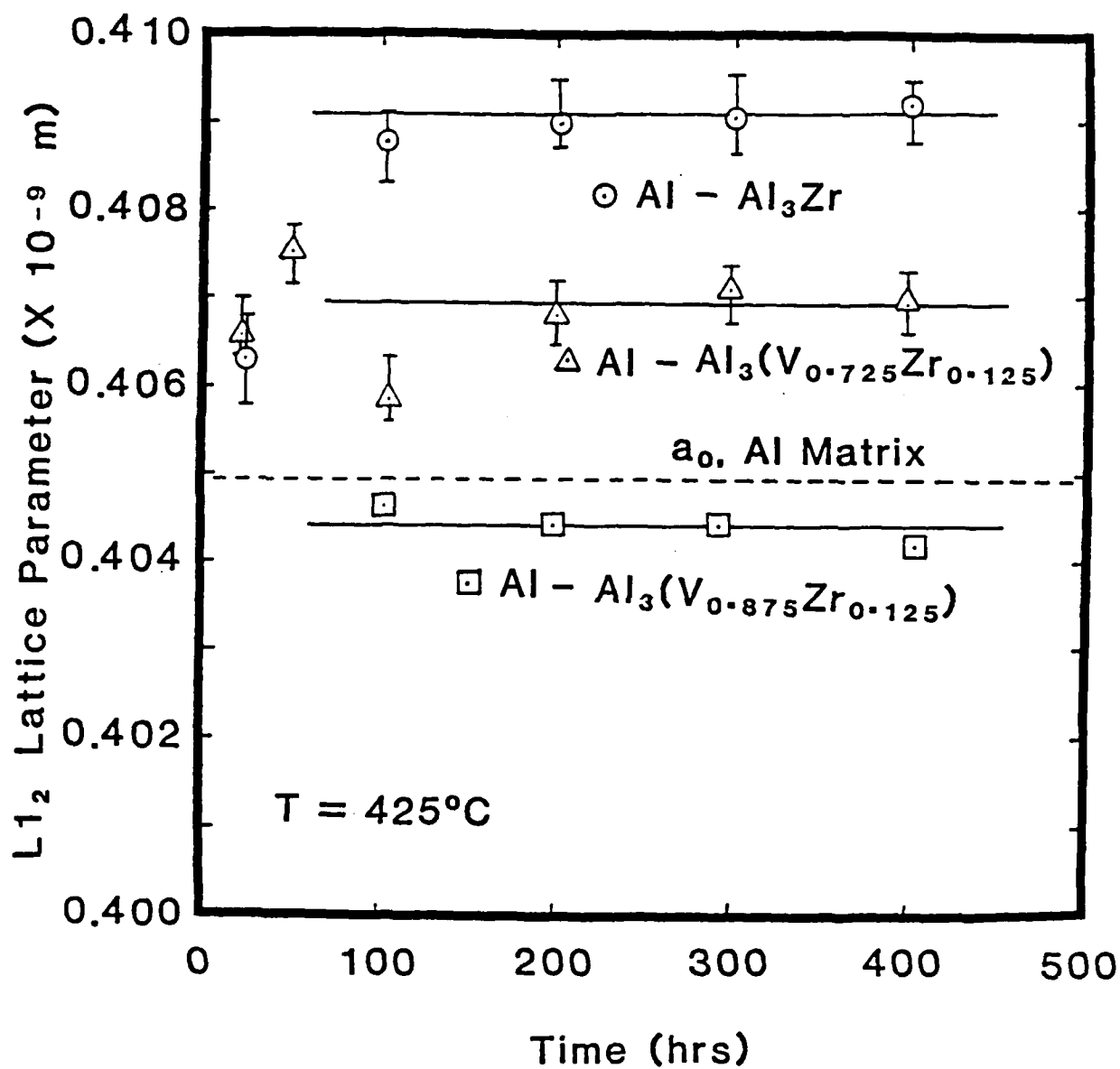


Fig. 3. Aging time dependence of the lattice parameters of cubic (L_{12} - structure) Al_3Zr , $\text{Al}-\text{Al}_3(\text{V}_{0.725}\text{Zr}_{0.125})$, and $\text{Al}_3(\text{V}_{0.875}\text{Zr}_{0.125})$. The aging temperature was 425°C but the lattice parameter measurements were made at room temperature.

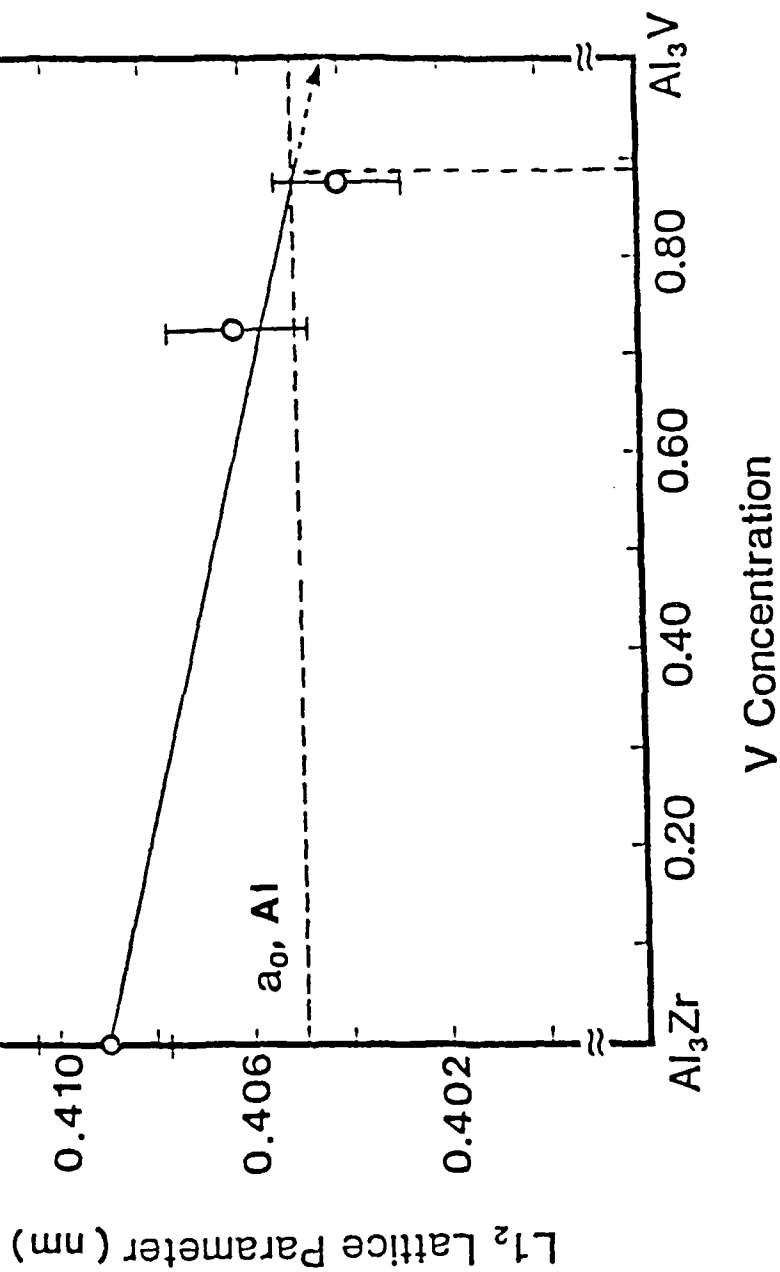
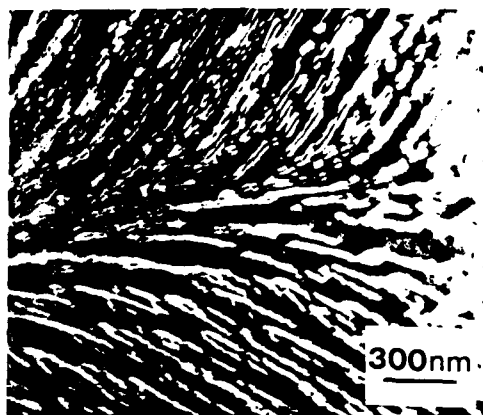
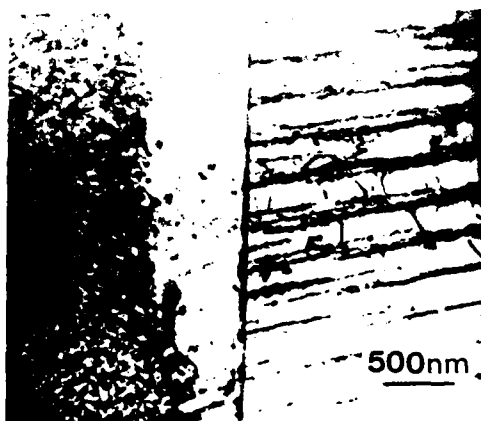


Fig. 4. Lattice parameter of cubic L₁₂ Al₃(Zr,V) versus vanadium concentration expressed as the V/Zr ratio in atom fraction.

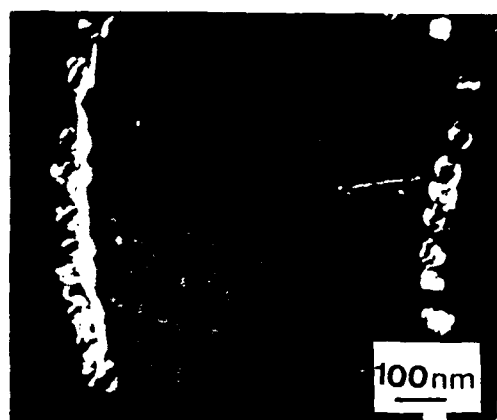


(a)

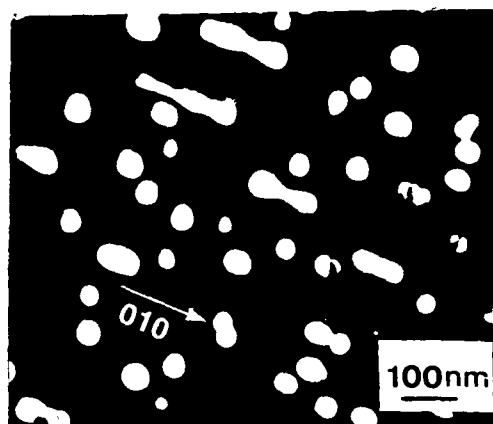


(b)

Fig. 5. Typical transmission electron microscope micrographs showing discontinuous precipitation of cubic LL_2 : a) Al_3Zr and b) $Al_3(V_{0.875}Zr_{0.125})$ after aging at $375^\circ C$ for 200 and 50 hrs, respectively.



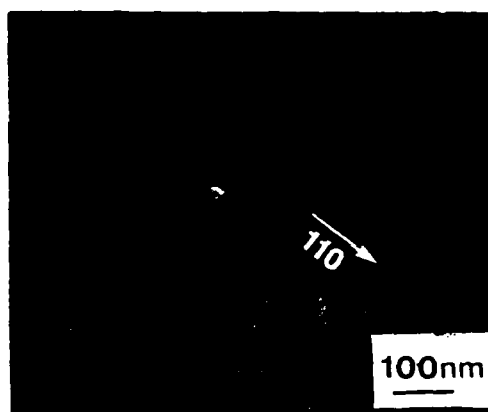
(a)



(b)

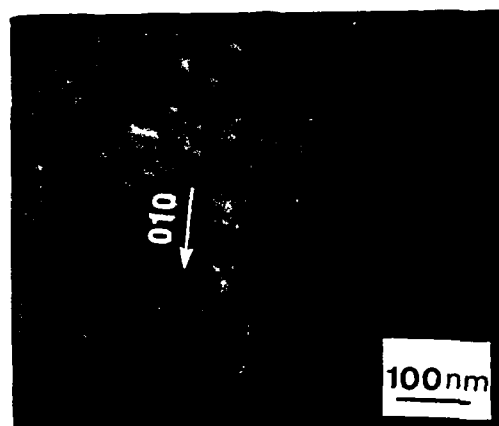


(c)

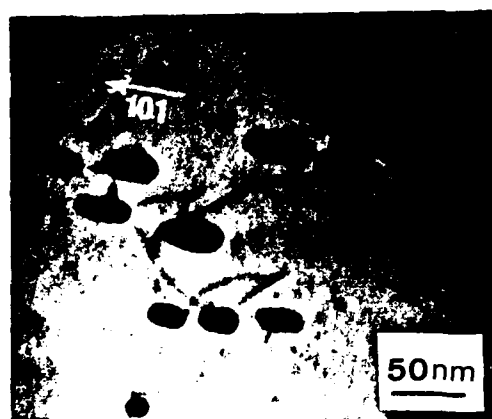


(d)

Fig. 6. TEM micrographs showing stages of precipitation of Al_3Zr at 450°C following 95% cold rolling. Aging times are: a) shows cubic LL_2 precipitates on dislocations after 5 hrs aging, b) shows an area where general precipitation of the cubic phase occurred after 10 hrs of aging, c) is a weak beam-dark field TEM showing precipitation of the cubic phase on dislocations after 13.5 hrs of aging, d) shows tetragonal DO_{23} Al_3Zr precipitates after 20 hrs of aging.

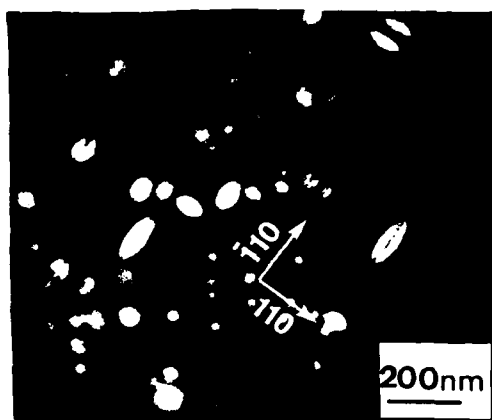


(a)

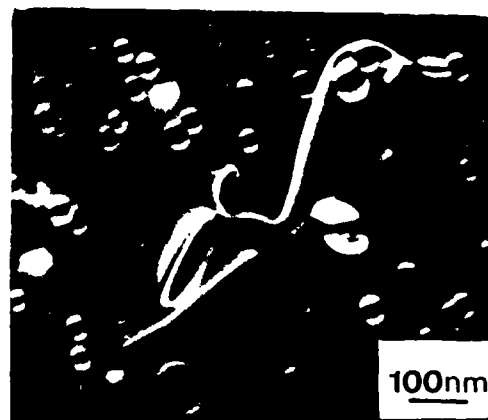


(b)

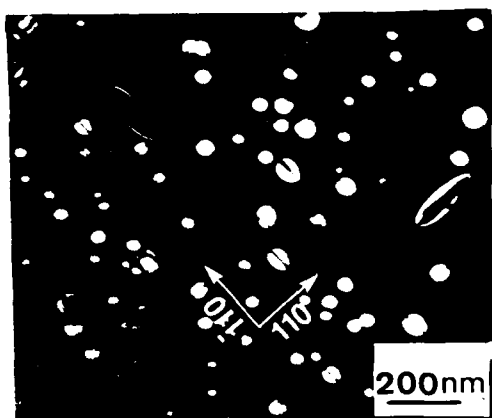
Fig. 7. TEM micrographs showing stages of precipitation of $\text{Al}_3(\text{V}_{0.275}\text{Zr}_{0.125})$ at 450°C : a) after 20 hrs of aging shows some rod-shaped as well as spherical cubic $\text{I}1_2$ precipitates, b) after 100 hrs of aging shows tetragonal DO_{23} precipitates.



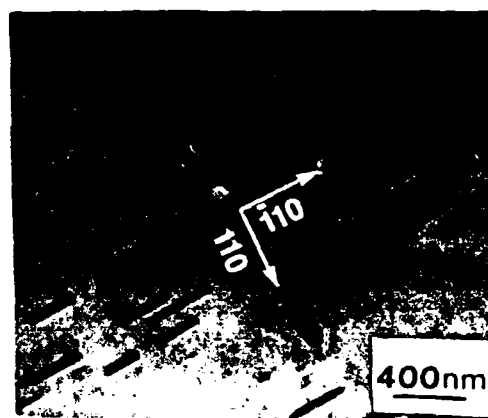
(a)



(b)



(c)



(d)

Fig. 8. TEM micrographs documenting transformation of cubic $L1_2$ Al_3Zr to an imperfect tetragonal " DO_{23} " Al_3Zr structure during aging at $600^\circ C$ after 95% cold rolling. Explanations are in text. a) and b) are after 12 hrs, c) is after 15 hrs and d) is after 25 hrs of aging.

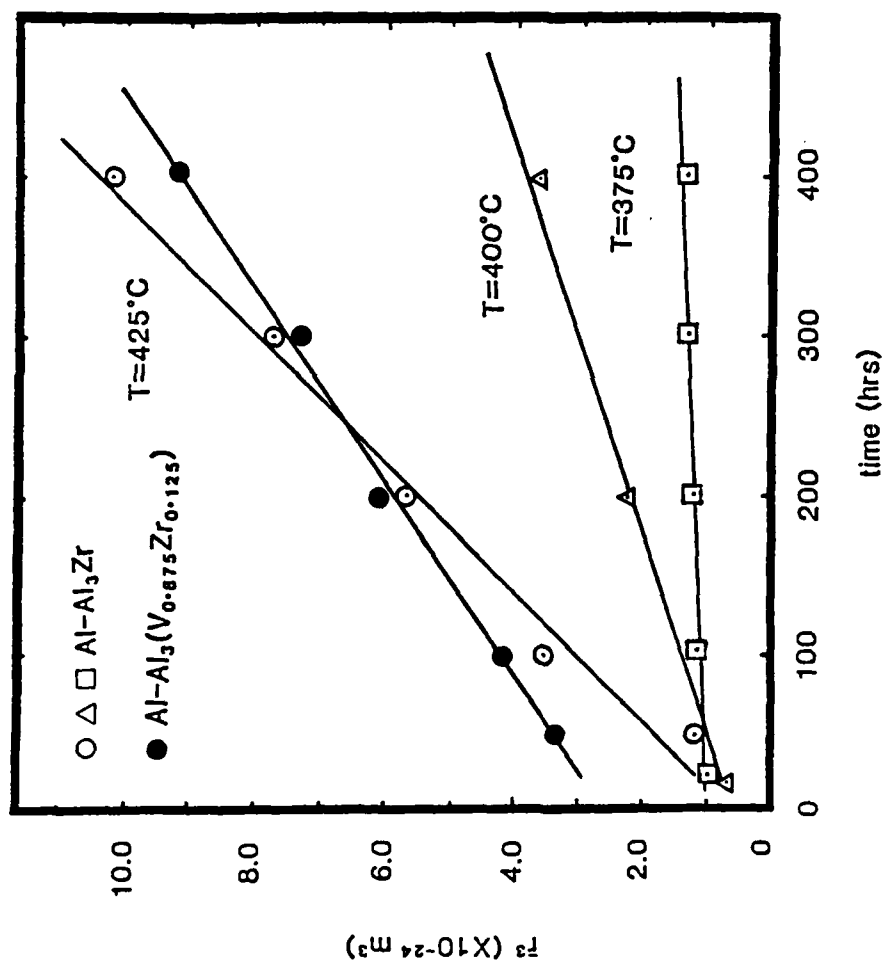
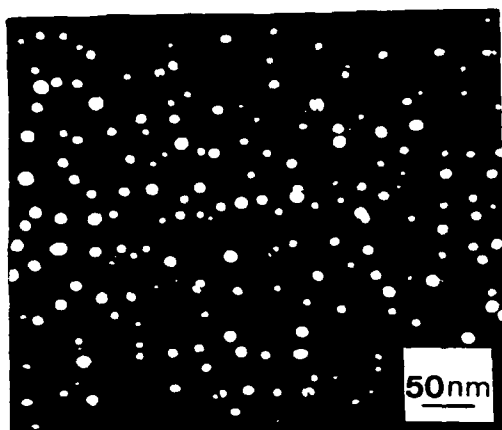
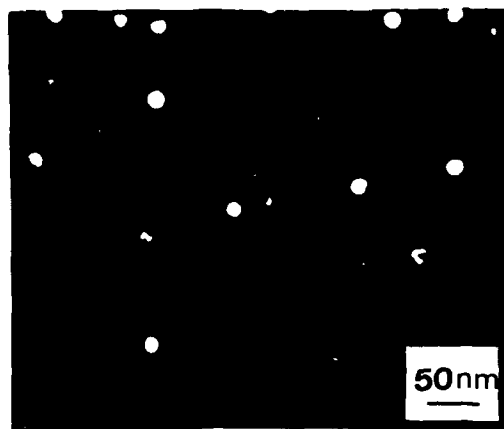


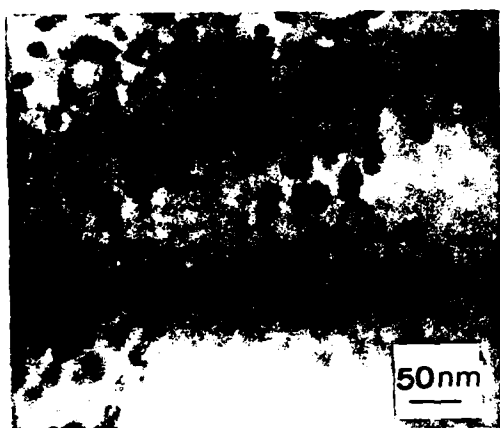
Fig. 9. Coarsening kinetics of cubic L1₂ Al₃Zr precipitates during isothermal aging at 375, 400, and 475°C. \bar{r} is the average particle radius at a particular time t . Specimens aged at 375°C and 400°C were pre-aged at 500°C to eliminate cellular precipitation. It was not necessary to pre-age the specimens aged at 425°C since cellular precipitation was not observed at this aging temperature. Coarsening kinetics of Al-Al₃(V_{0.975}Zr_{0.125}) at 425°C is also shown.



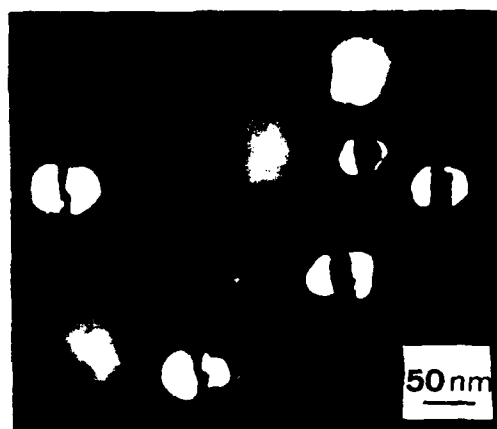
(a)



(b)



(c)



(d)

Fig. 10. TEM micrographs documenting coarsening of cubic $L1_2$ Al_3Zr after 20 and 200 hrs of aging at: a) and b) $400^\circ C$ and c) and d) $425^\circ C$.

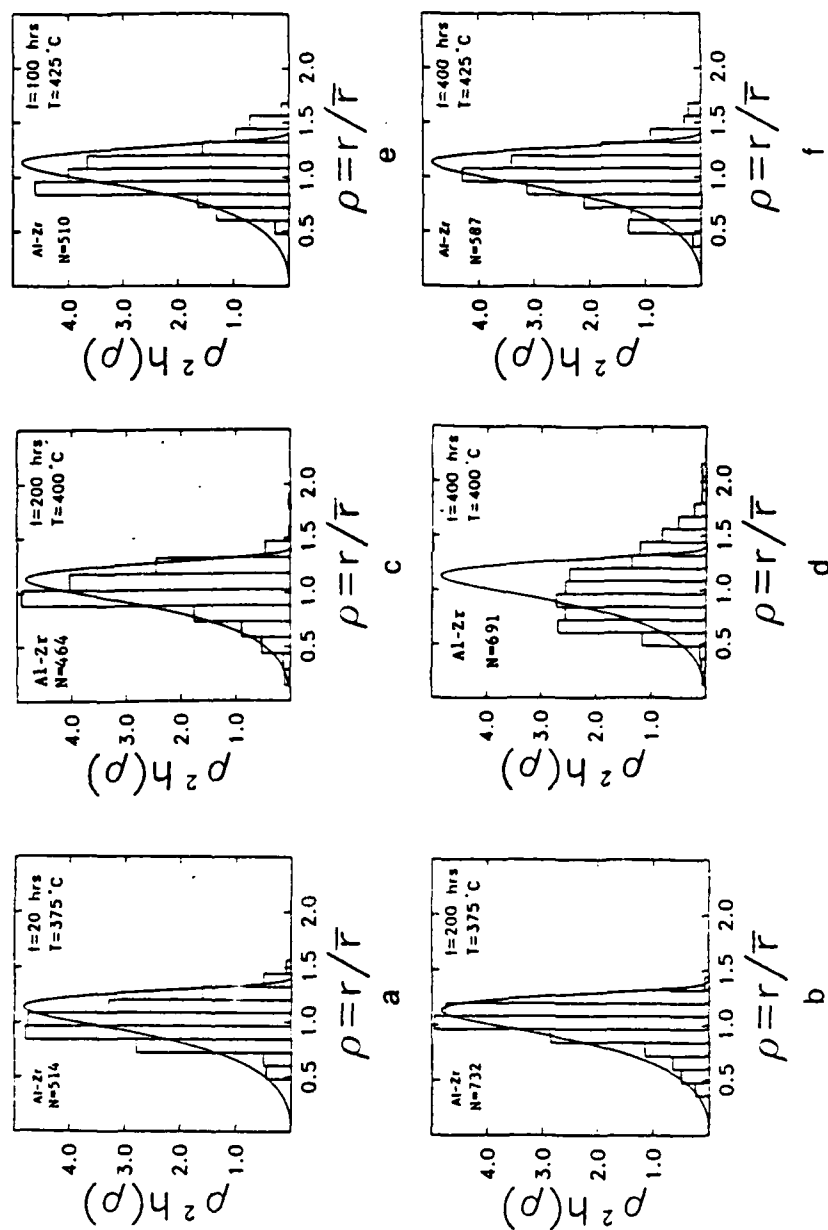


Fig. 11. Normalized particle size distributions for cubic Al_3Zr aged for various times at 375, 400 and 425°C. The solid curve shows the predicted LSW distribution. For the 375 and 400°C aging, the specimens were pre-aged 0.5 hrs at 500°C. a) 20 hrs at 375°C, b) 200 hrs at 375°C, c) 200 hrs at 400°C, d) 400 hrs at 400°C, e) 100 hrs at 425°C, f) 400 hrs at 425°C.

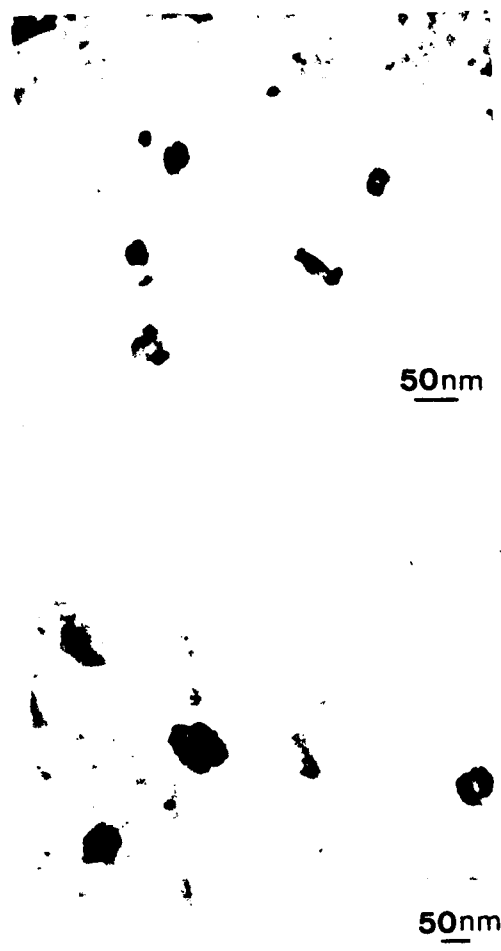


Fig. 12. TEM micrographs of cubic $\text{Al}_3(\text{V}_{0.875}\text{Zr}_{0.125})$ after aging 20 and 200 hrs at 425°C . The solid curve shows the predicted LSW distribution.

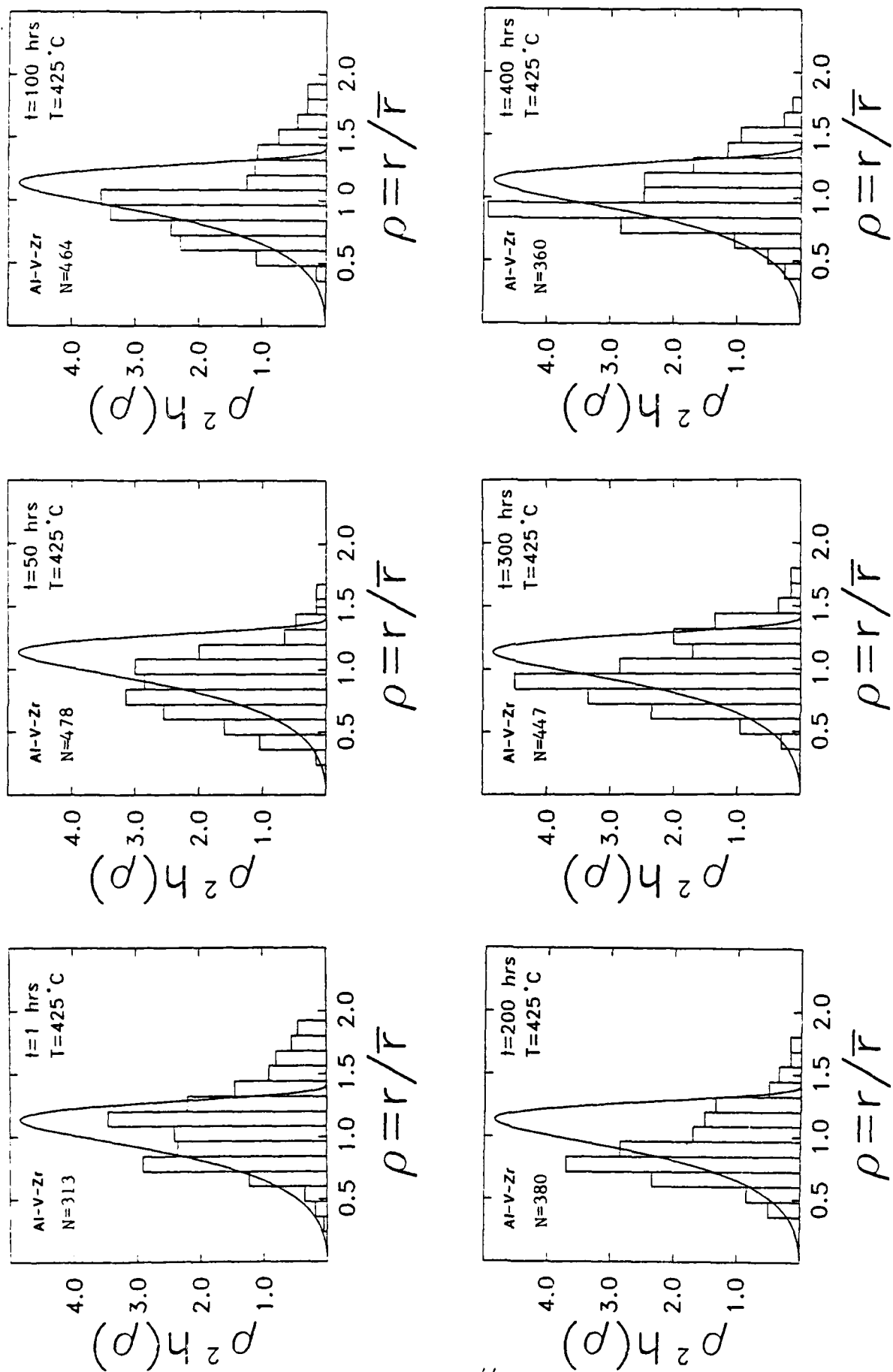


Fig. 13. Normalized particle size distributions for cubic $\text{Al}_3(\text{V}_{0.875}\text{Zr}_{0.125})$ aged from 1 to 400 hrs at 425°C .

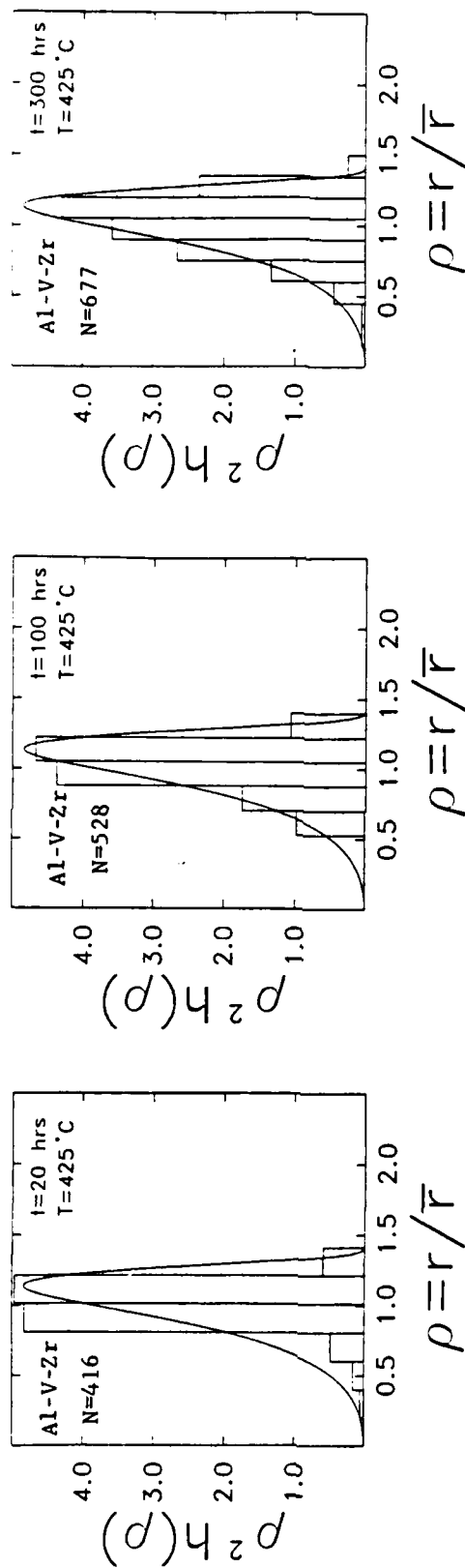


Fig. 14. Normalized particle size distributions for cubic $\text{Al}_3(\text{V}_{0.725}\text{Zr}_{0.275})$ aged for 20, 100, and 300 hrs at 425°C . In order to try to achieve a steady distribution, the specimens were pre-aged for 1 hr at 500°C . The solid curve shows the predicted LSW particle size distribution. Note the agreement between measurements and theory is much better than in Fig. 13 where the samples were not pre-aged.

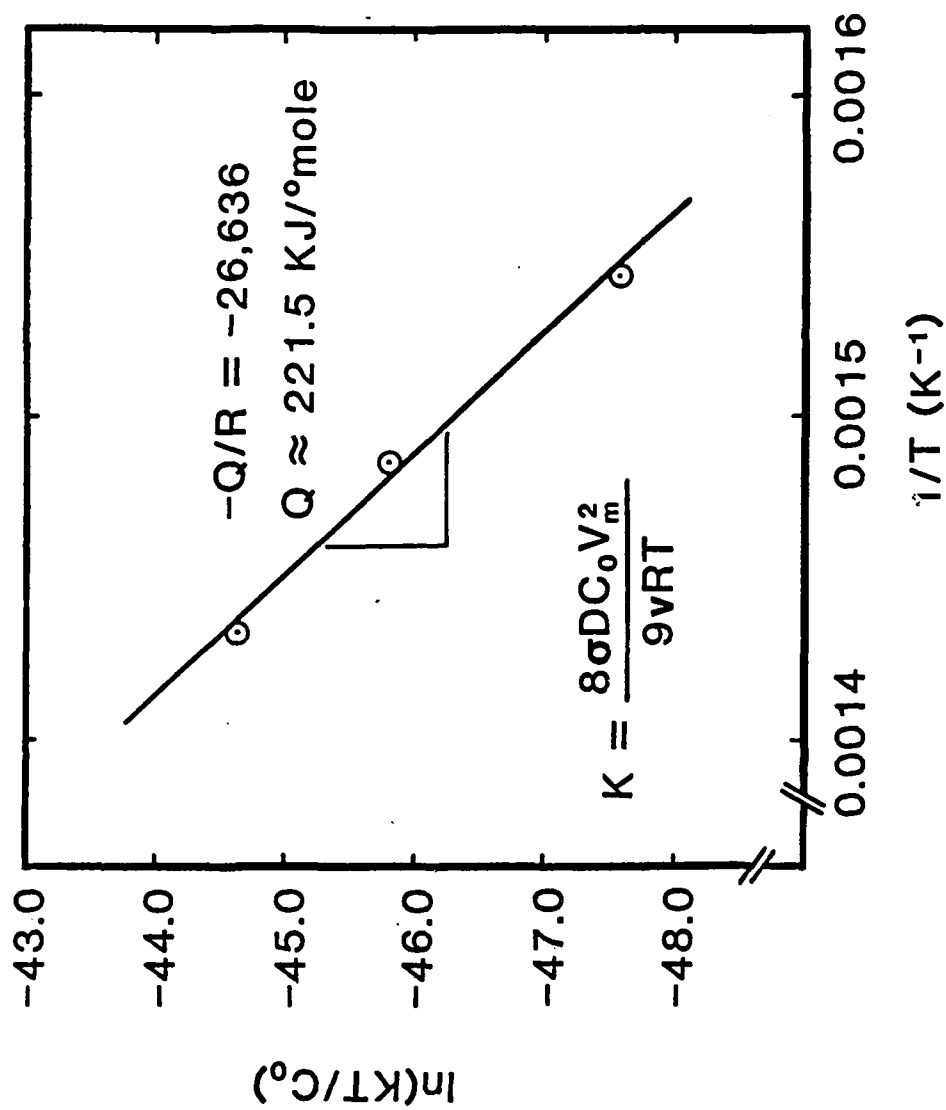


Fig. 15. Determination of the activation energy, Q , for the coarsening of cubic Ll_2 Al_3Zr precipitates from a plot of $\ln(KT/C_0)$ vs. $1/T$.

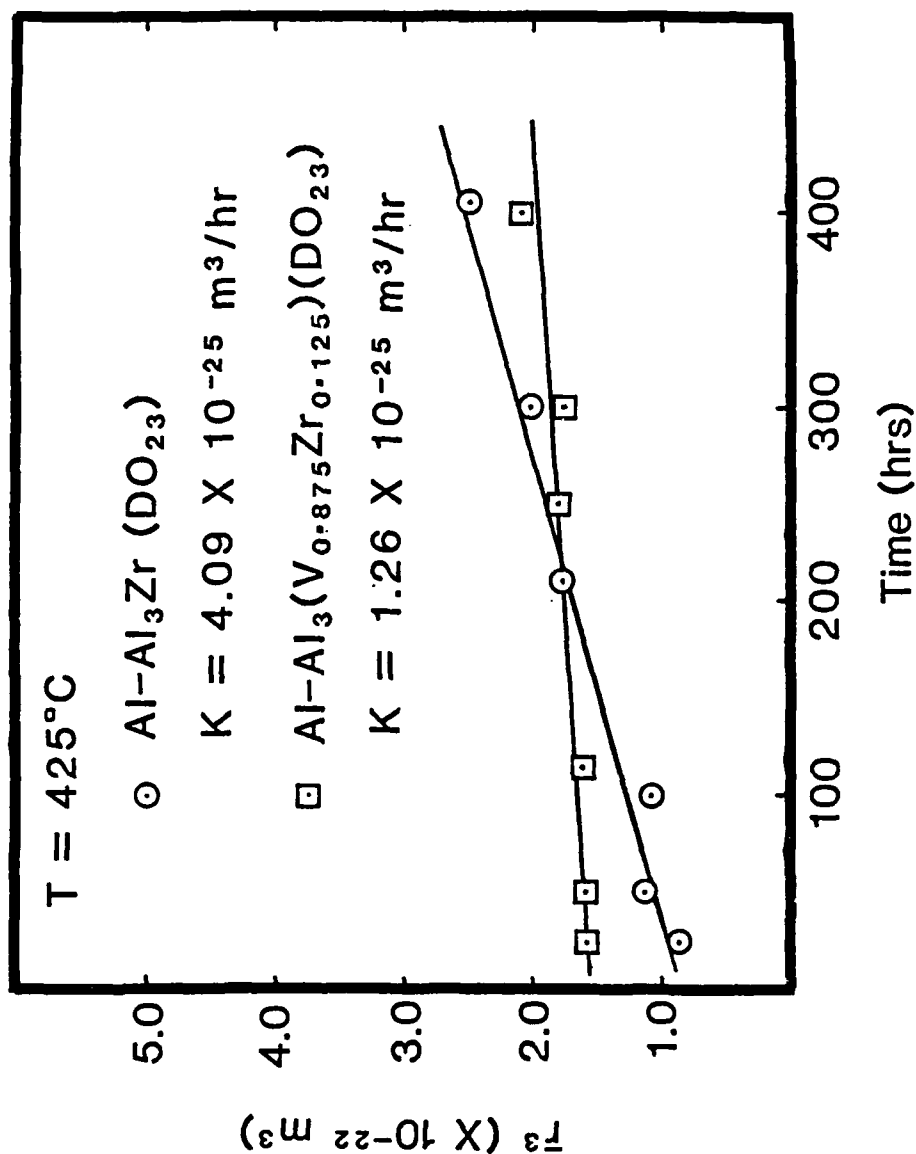
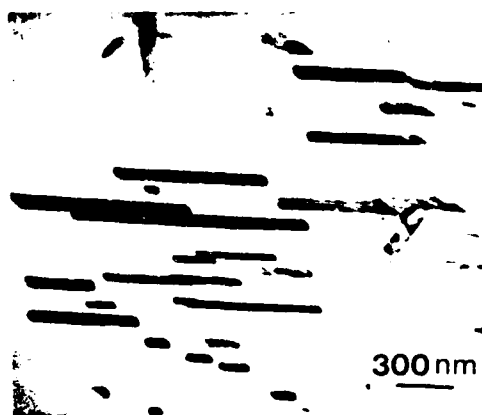
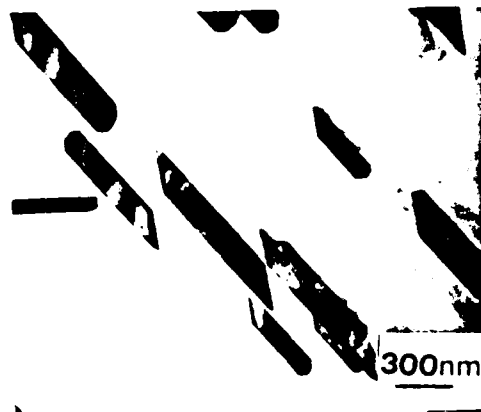


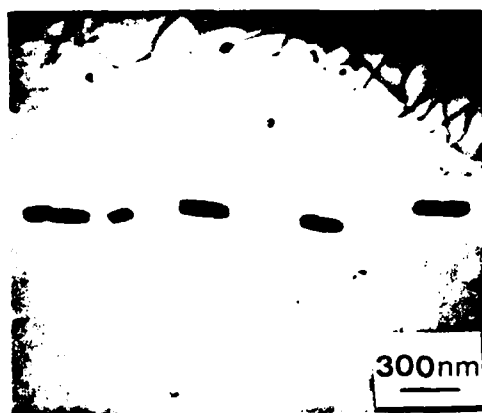
Fig. 16. Comparison of volumetric coarsening rate of tetragonal DO₂₃ Al₃(V_{0.875}Zr_{0.125}) with Al₃Zr during isothermal aging at 425°C. The particle size \bar{r} is defined as half the average thickness of the plate-like particles across the minor axis of the image in the micrographs. The Al-Zr alloy was cold rolled 90% and pre-aged 50 hrs at 600°C. The Al-V-Zr alloy was cold rolled an additional 5% and annealed an additional 50 hrs at 600°C to convert it to the DO₂₃ phase. Thus at short times particle size is much larger.



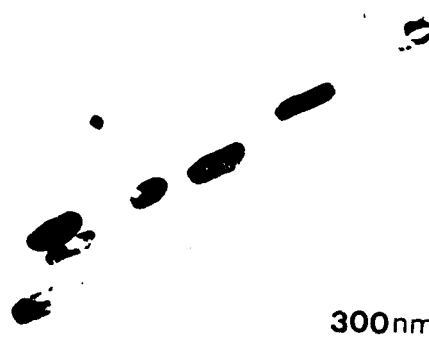
(a)



(b)

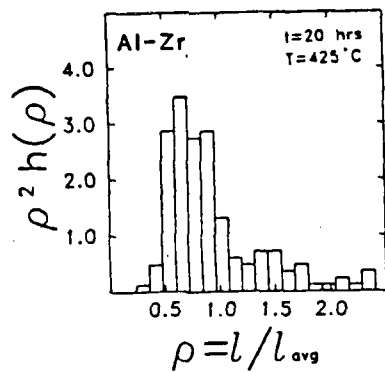


(c)

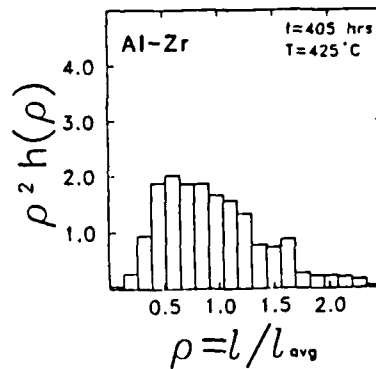


(d)

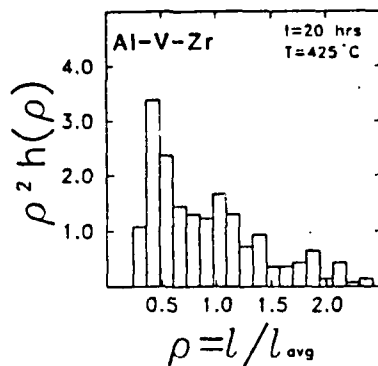
Fig. 17. TEM micrographs showing tetragonal DO_{23} Al_3Zr (a,b) and $Al_3(V_{0.3-0.5}Zr_{0.125})$ (c,d) precipitates after aging 20 (a,c) and 400 (b,d) hrs at $425^\circ C$. Pre-treatments are described in caption to Fig. 16.



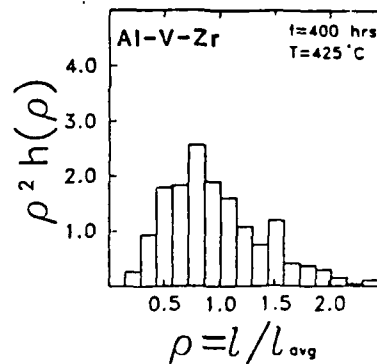
(a)



(b)



(c)



(d)

Fig. 18. Particle size distributions for tetragonal Al_3Zr (a,b) and $\text{Al}_3(\text{V}_{0.035}\text{Zr}_{0.125})$ (c,d) aged at 425°C for 20 (a,c) and 400 hrs (b,d). Particle size is defined in the caption for Fig. 16.

PARTICLE COARSENING STUDIES OF AN RSP P/M Al-Fe-Ce ALLOY

L. Angers*, M. E. Fine and J. R. Weertman

Department of Materials Science & Engineering and
Materials Research Center, Northwestern University
Evanston, IL 60201 USA

ABSTRACT

A study has been carried out of the coarsening kinetics of the dispersed phase particles in a rapidly solidified Al-7.5 wt.% Fe-3.4 wt.% Ce alloy subjected to isothermal annealing for various times at 475°C and above. Two dispersed phases appear to be present at equilibrium, $\text{Al}_{13}\text{Fe}_4$ and $\text{Al}_{10}\text{Fe}_2\text{Ce}$. They constitute 23 percent of the volume. The data are discussed in terms of the Lifshitz-Slyozov-Wagner theory for diffusion controlled coarsening modified for high volume fractions of dispersed phase. The modified theory (MLSW) applies to binary systems containing one kind of dispersed phase which is present in the form of spheres. Extension of the MLSW theory to the present system is discussed. While the expected linear relation between time and the cube of the average particle radius is observed, the dispersed phases coarsen at rates which are orders of magnitude greater than predicted. The origin of this difference is discussed.

* Present address: Alcoa Technical Center, Alcoa Center, PA 15069.

I. INTRODUCTION

Rapid solidification powder (RSP) technology is a highly promising avenue for the development of high temperature aluminum alloys. The necessary high volume fractions of suitably sized dispersoids can be obtained with alloys having high liquid solute solubilities but low solid solute solubilities. Furthermore, solutes may be selected which have low solid state diffusion rates in binary solution with aluminum.¹ Such alloys should exhibit a low rate of Ostwald ripening. The microstructure even after consolidation and fabrication is fine grained and all dispersed phases are quite small in size. Of a large number of candidate high temperature RSP ternary alloys prepared at Alcoa, an Al-Fe-Ce alloy containing approximately 7.5 wt.% Fe and 3.4 wt.% Ce was found to be one of the most promising in terms of elevated temperature yield and tensile strengths, ductility and creep resistance.² This alloy is suggested for applications requiring good strength for long periods of time at temperatures up to approximately 315°C.

According to the 500°C isotherm of the ternary Al-Fe-Ce diagram reported by Zarechnyuk et al.³, the phases in equilibrium with aluminum in the Al-7.5Fe-3.4Ce alloy are $Al_{13}Fe_4$ and $Al_{10}Fe_2Ce$. The $Al_{13}Fe_4$ phase is monoclinic having 100 atoms per unit cell with dimensions $a = 1.5489$ nm, $b = 0.80831$ nm, $c = 1.2476$ nm and $\beta = 107.71^\circ$.⁴ Convergent beam electron diffraction studies carried out on the $Al_{10}Fe_2Ce$ phases have shown the structure to be orthorhombic having 52 atoms per unit cell with dimensions $a = 0.894$ nm, $b = 1.022$ nm and $c = 0.906$ nm.⁵ Rapid solidification often produces metastable phases and therefore an RSP alloy may be expected to contain such non-equilibrium phases.

The purpose of the present research was to investigate the stability of the dispersoids in several Al-Fe-Ce alloys with respect both to phase change

and to Ostwald ripening. The particles present after various aging treatments were identified using x-ray diffraction. Quantitative metallography was used in conjunction with TEM examination of thin foils and shadowed replicas to obtain quantitative information on particle sizes and shapes. For several reasons, the temperatures chosen for this study were considerably higher than the intended maximum operating temperature of the Al-Fe-Ce alloy. Since coarsening at the higher temperatures is much faster, the kinetics are easier to study and, of course, equilibrium is approached more rapidly. Certain material parameters required for subsequent analysis of the results are available only for the higher temperatures. In addition, x-ray diffraction patterns from material aged at 475°C and higher reveal well defined peaks while the patterns from material aged at 315°C show only low intensity broad peaks similar to those from the as-received material. Finally, the average particle size varies from place to place in samples aged at 315°C.

II. EXPERIMENTAL PROCEDURE

An Al-7.5Fe-3.4Ce alloy, developed at Alcoa under AFML Grant No. F33615-77-C-5086 and obtained from Wright Patterson Air Force Base, was used for the study of coarsening during isothermal anneals. The Al-7.5Fe-3.4Ce alloy billet from which samples were obtained had been prepared by gas atomization, cold isostatic pressing, hot isostatic pressing and finally forging.

Small pieces of the forging were isothermally aged in 1.1×10^{-3} Pa vacuum at temperatures of 475 or 575°C for varying lengths of time up to 240 hours. Particle size measurements were made from TEM micrographs of shadowed two stage replicas of polished specimen surfaces. A point counting technique was used to calculate the volume fraction, V_v , taken up by the dispersed phases.⁶ The surface area, S_v , per unit volume of particle-matrix interface

was calculated from the number of intersections of precipitates with grid lines.⁶ A value for the particle mean intercept length, \bar{L} , for each aging time and temperature combination, was obtained from the volume fraction and surface area per unit volume⁶ using the formula

$$\bar{L} = 4V_v/S_v \quad [1]$$

The relationship of Eq.(1) is independent of particle shape and is valid for particles having both convex and concave regions of particle/matrix interface. Intercept length distribution histograms were constructed for various aging conditions from the intersection lengths of particles with grid lines. Over 400 particles were measured in the construction of each histogram. The intercept lengths, L , corresponding to the intervals ΔL in a histogram were normalized with respect to \bar{L} . The relative frequencies of occurrence of intercept lengths in each interval, $f(L/\bar{L})$ were normalized such that

$$\sum_{\text{all } \Delta L} f(L/\bar{L}) \Delta f(L/\bar{L}) = 1$$

X-ray diffraction using Cu-K α radiation was employed to gain information about the identity of dispersed phases as a function of aging time and temperature.

III. RESULTS AND DISCUSSION

A. X-ray Diffraction

X-ray diffraction revealed the same sets of d-spacings for the Al-7.5Fe-3.4Ce specimens aged at 575 and at 475°C (despite morphological differences observed by TEM). Table I lists these d-spacings after deletion of the Al lines. The relative intensities, I/I_0 , listed in Table I for each spacing represent the ratio of the peak height to the height of the strongest peak

attributed to a dispersed phase spacing. Several of the low intensity lines do not have well defined positions, and these varied somewhat from pattern to pattern. On the right side of Table I, the measured spacings are compared to the spacings of $\text{Al}_{13}\text{Fe}_4$ as given by the JCPDS file 29-42 and to the spacings calculated for $\text{Al}_{10}\text{Fe}_2\text{Ce}$ using the crystallographic results given in the introduction.⁵ Relative intensity information was available only for the $\text{Al}_{13}\text{Fe}_4$ phase. All experimentally obtained spacings may be attributed to at least one or the other of the two phases, supporting the phase diagram reported by Zarechnyuk et al.³ and indicating that aging at 475°C gives the equilibrium phases. Several $\text{Al}_{13}\text{Fe}_4$ peaks are missing from the pattern. Nevertheless, it is quite evident that there is more than one distinct dispersed phase coarsening in the Al-Fe-Ce system. As subsequently discussed, analytical results using a STEM confirm this conclusion.

If it is assumed that both monoclinic $\text{Al}_{13}\text{Fe}_4$ and orthorhombic $\text{Al}_{10}\text{Fe}_2\text{Ce}$ are present, the available phase diagram³ may be used to predict the constitution of the Al-7.5Fe-3.4Ce forging in this study: 81.5% Al(ss), 9.6% $\text{Al}_{13}\text{Fe}_4$ and 8.9% $\text{Al}_{10}\text{Fe}_2\text{Ce}$ by volume. The alloy should contain a total of about 19 vol.% dispersed phase. The volume fraction of the dispersed phases was determined metallographically to be 23%, as shown later.

B. Particle Growth Rates During Isothermal Annealing

Figure 1 shows a series of TEM micrographs of the replicas of specimens of the forged alloy aged at 575°C. The dispersed particles are non-spherical. Many are more or less equiaxed but some appear needle or plate-like. The shape of many of the particles indicates that coalescence events have occurred after even short times of aging at 575°C. Micrographs representing the coarsening process at 475°C are shown in Fig. 2. Aging at the lower temperature appears to produce many more needle or plate-like particles. The TEM

micrographs shown in Fig. 3 of thin foils made from aged specimens illustrate the morphological differences caused by changing the aging temperature from 475 to 575°C.

The volume fraction of the dispersed phase was monitored during aging at both temperatures. Figure 4 shows the volume fraction determined by quantitative microscopy as a function of time. Error bars in this figure and in all subsequent figures indicate 95% confidence intervals of the mean value. The dispersed phase volume fraction remained essentially constant at 23% during aging at both 475 and 575°C. This value is somewhat higher than the estimate (19%) from the Al-Fe-Ce diagram but the agreement is good considering the approximations made in making the estimate.

The results of measurements of particle mean intercept length after aging at 575 and 475°C are presented in Table II. The \pm again indicates the 95% confidence interval about the average value of mean intercept length calculated for different regions of the same specimen and does not refer to the distribution of particle sizes.

A number of theories⁷⁻¹⁰ modelling the coarsening of dispersed phase particles, after some aging time, predict equations having the form

$$\bar{r}^n = A + B_n t \quad [2]$$

where \bar{r} is the average particle radius after time t of aging and A and B_n are constants. The exponent n is generally an integer between 2 and 5. Its value depends on the rate controlling mechanism of growth, i.e., growth limited by reaction at the interface ($n=2$)⁸, by bulk diffusion ($n=3$)^{7,8}, by grain boundary diffusion ($n=4$)⁹, or by dislocation pipe diffusion ($n=5$).¹⁰ All models require a number of simplifying assumptions. Binary alloys containing an infinitely dilute dispersion of a single phase may be treated

easily. The Al-Fe-Ce system, however, is a ternary system with a high volume fraction of two types of non-spherical particles. Nevertheless, the mean intercept length data of this study were inserted into Eq.[2] for the cases of $n = 1, 2, 3, 4$ and 5 . A least squares analysis was used to obtain a "rate constant" B_n for each case. In addition, a correlation coefficient, R , was calculated to obtain a quantitative measure of the deviation from linearity for each value of n . The correlation coefficient R is given by the expression:

$$R = \frac{m \sum_{i=1}^m \bar{L}_i^n t_i - (\sum \bar{L}_i^n)(\sum t_i)}{\sqrt{\{m(\sum \bar{L}_i^{2n}) - (\sum \bar{L}_i^n)^2\} \{m(\sum t_i^2) - (\sum t_i)^2\}}} \quad [3]$$

where m is the number of data points available and \bar{L}_i represents an individual data point taken at time t_i .

Values of R closest to unity represent the most nearly linear fit. In Fig. 5, the coefficient R is plotted versus the exponent n for the data taken from specimens aged at 475 and 575°C . The plots clearly show that at both temperatures the exponent $n=3$ results in the best fit of a straight line to the data although the R 's for $n=2$ or $n=4$ are nearly as good, particularly at 475°C . Thus the data in this respect are consistent with volume diffusion control of Ostwald ripening at 575 and 475°C but do not exclude coarsening by other mechanisms.

The results of Table II have been plotted in Fig. 6 as mean intercept length cubed, \bar{L}^3 , versus aging time to conform with the analysis of Fig. 5 for the data taken at 475 and 575°C . Aside from the expected initial transient the fit is reasonably good, as indicated by the high R value for $n=3$. The particle volumetric growth rate, or rate constant k , is given by the slope of the \bar{L}^3 versus t line. A mean intercept length may be converted to an effective radius by calculating the radius of a sphere which, when

intercepted by random lines across a planar probe, would lead to the measured mean-intercept length. Rate constants based on this conversion for coarsening at 575 and 475°C are listed in Table III.

The Lifshitz-Slyozov-Wagner (LSW) theory^{7,8} for coarsening of spherical particles in a dilute binary system controlled by bulk diffusion leads to the following equations for coarsening behavior once an initial transient phase has past:

$$\begin{aligned} \bar{r}^3 - \bar{r}_0^3 &= K t \\ K &= 8\sigma D C_0 \Omega^2 / 9kTx_B^\beta \end{aligned} \quad [4]$$

where \bar{r} is the average particle radius at time t , \bar{r}_0 is a constant, σ is the interfacial energy, D is the diffusivity of the solute in the matrix, C_0 is the equilibrium solubility limit of the solute in the matrix, Ω is the atomic volume of the solute in the second phase, x_B^β is the atom fraction of solute in the dispersed phase made up of β type particles, and k and T have their usual meanings.

As already stated, the LSW theory applies to a dilute binary system having spherical particles of one dispersed phase. The ternary system under consideration has a high volume fraction of two different types of non-spherical dispersoids. Being a ternary system poses no obvious problem in the use of the LSW theory since the Gibbs-Thompson expression, from which the LSW theory is derived, is applicable to ternary as well as binary systems. The diffusivity and atom fraction refer to the rate controlling component. However, the diffusivity of the controlling element in its composition gradient may be affected by the presence of the third element and in addition cross terms in the diffusion expression must be included.

Several modifications of the LSW theory for non-dilute dispersions are

available in the literature¹¹⁻¹⁴ with volume fraction of particles as a variable. The Brailsford and Wynblatt¹² modified LSW theory (MLSW) considers the radial growth of a particle embedded in a random array of particles of like nature but of varying sizes. The theory neglects the possibility of particle coalescence. It predicts an increase over the LSW rate constant by a factor of 2.6 for a system containing 23 volume % dispersed phase. The Davies, Nash and Stevens model¹⁴, based on the Lifshitz-Slyozov Encounter Model (LSEM), considers the effect on particle growth for the case in which the diffusion fields of the particles encounter one another. It predicts coarsening rates 1.5 times faster than the LSW theory for systems with 23 volume percent dispersed phase.

Further analysis is more tractable if it is assumed that dispersoids are spherical, with an effective average radius calculated from the mean intercept length. This assumption may be reasonable for discussing kinetics at 575°C, where the dispersoids are primarily equiaxed, but is somewhat less reasonable for the needle or plate-like particles present after aging at 475°C. However, it has been suggested that if scale factor coarsening is occurring, all assumptions of spherical morphology drop out of the LSW derivation.¹⁵

For comparison of the observed rate constants to the rate constants predicted by the MLSW theory, the presence of two different phases coarsening simultaneously in the RSP Al-Fe-Ce alloy of the present study remains a problem. It may be proposed that the rate of growth of the $Al_{13}Fe_4$ particles will be limited by the solid state diffusion of Fe in Al and that the $Al_{10}Fe_2Ce$ particle growth will be limited by the slow diffusion rate of Ce in Al. It is also expected that the measured growth rate will be an average of the growth rates of the two types of particles and therefore the measured rate constant K is a weighted average of the rate constants calculated for each separate phase.

An attempt was made to calculate the rate constants for each of the two species using a typical value of 1 J/m^2 for the incoherent particle-matrix interfacial energy. The remaining constants necessary for these calculations have been obtained from the literature. Diffusivities of Fe in Al^{16} and Ce in Al^{17} have been reported to be $0.12 \times 10^{-4} \exp(-16.2 \times 10^3/T) \text{ m}^2/\text{s}$ and $1.9 \times 10^{-10} \exp(-13.3 \times 10^3/T) \text{ m}^2/\text{s}$, respectively, in the temperature range of interest. Solid solubility of Fe in Al^{18} is reported to be approximately 0.0085 at.% at 575°C and 0.0021 at.% at 475°C and that of Ce in Al^{19} is approximately 0.0035 at.% at 575°C and 0.0017 at.% at 475°C . These values were used in the coarsening calculations for the ternary alloy. Atomic volumes were obtained from the lattice parameters.^{4,5} The atomic volume of Fe in $\text{Al}_{13}\text{Fe}_4$ was calculated to be $1.49 \times 10^{-29} \text{ m}^3/\text{atom}$ and that of Ce in $\text{Al}_{10}\text{Fe}_2\text{Ce}$ to be $1.60 \times 10^{-29} \text{ m}^3/\text{atom}$. The rate constants calculated for the growth of $\text{Al}_{13}\text{Fe}_4$ and $\text{Al}_{10}\text{Fe}_2\text{Ce}$ are referred to as $K_{\text{calc}}^{\text{Al}_{13}\text{Fe}_4}$ and $K_{\text{calc}}^{\text{Al}_{10}\text{Fe}_2\text{Ce}}$ and are listed in Table III. The Brailsford and Wynblatt volume fraction correction factor for the predicted volume fraction of each phase was used in the calculations. It is evident from a comparison of the measured and calculated rate constants that the dispersoids are ripening much more rapidly than predicted by the MLSW theory using the approximations previously mentioned. The value of the measured rate constant is 20 to 80 times greater than $K_{\text{calc}}^{\text{Al}_{13}\text{Fe}_4}$ and about four and one-half orders of magnitude greater than $K_{\text{calc}}^{\text{Al}_{10}\text{Fe}_2\text{Ce}}$. Considering the approximations made, the agreement for $\text{Al}_{13}\text{Fe}_4$ is perhaps as good as can be expected; however, the large discrepancy for $\text{Al}_{10}\text{Fe}_2\text{Ce}$ indicates something is drastically wrong in the calculation. The calculation predicts that a bimodal particle size distribution will evolve: large $\text{Al}_{13}\text{Fe}_4$ and small $\text{Al}_{10}\text{Fe}_2\text{Ce}$ particles. Such a distribution was not observed, as discussed in the next section. The particle size distributions,

as shown in Figs. 7 and 8 do not appear to be bimodal. STEM composition analysis confirmed that the $\text{Al}_{10}\text{Fe}_2\text{Ce}$ particles are about the same size as the $\text{Al}_{13}\text{Fe}_4$. Coarsening rates in a somewhat similar alloy, a centrifugally atomized Al-Fe-Mo-V alloy where only one dispersed phase ($\text{Al}_{13}(\text{Fe},\text{Mo},\text{V})_4$) is present, also were found to be much faster than predicted by the MLSW calculation.²⁰ If it is assumed that the slow diffusion of Mo in aluminum is rate limiting, the measured growth rates are two and a half orders of magnitude faster than predicted. Thus the presence of two different dispersed phases is not a necessary condition for the observed accelerated Ostwald ripening.

Possible origins of the discrepancy between the calculated and measured rates need to be examined: 1) inaccurate literature values for solubilities and diffusivities in the binary systems, 2) changes in solubilities or diffusivities from binary system values, 3) rate controlled by interface reaction rather than diffusion, 4) accelerated diffusion due to excess vacancies, dislocations, and grain boundaries, and 5) inapplicability of the MLSW theory with the present assumptions to this Ostwald ripening system.

Inaccurate or inappropriate values for the solubility limits and/or diffusivities could, of course, explain why Ostwald ripening is so much more rapid than predicted by the MLSW equation. The actual solubility limits of Fe and Ce in Al in the ternary alloy under study are not known; however, it is highly unlikely that the solubility of Ce in the (ss) Al is orders of magnitude greater in the ternary alloy than in the binary Al-Ce system. The diffusivity data for Ce in Al used in the calculation are suspect because an oxide barrier could have given an erroneously low experimental value.¹⁷ Further, the value in the ternary system could be much greater.

If the coarsening rate were actually controlled by the reaction at the interface, a growth rate even slower than predicted for the bulk diffusion

controlled case is expected. A few particles had regions of negative curvature on their surfaces suggesting solute or impurity drag at these regions but again this does not explain why the Ostwald ripening rate is much more rapid than predicted for a bulk diffusion process.

It has been predicted that coarsening controlled by grain boundary diffusion¹⁰ should follow a linear relationship between \bar{r}^4 and t ; dislocation pipe diffusion control should produce an \bar{r}^5 linear dependence on t .¹⁰ The rapid solidification and subsequent compaction processes lead to a very small grain size and high defect density. Therefore, such sources of enhanced diffusivity should not be ruled out even though an \bar{r}^3 versus t relationship gives the best fit to the data. As already mentioned, the correlation factor for \bar{r}^4 versus t is nearly as high as for \bar{r}^3 versus t . Furthermore, particles may be coarsening by several mechanisms whose relative contributions may be time dependent.

An expression representing growth of particles in an infinitely dilute system by diffusion along grain boundaries has been given by Kirchner⁹:

$$\bar{r}^4 - \bar{r}_0^4 = K' t \quad [5]$$

$$K' = 9C_0 D_G w \Omega^2 \sigma / 64 X Y k T .$$

Here D_G is the grain boundary diffusion coefficient and w is the grain boundary width. The constant $X = (2-3m + m)/3$, where m is half the ratio of the grain boundary energy to the particle-matrix interfacial energy and $Y = 0.5 \ln(1/f)$, where f is the average area fraction occupied by particles on the grain boundaries. The quantity Y has also been expressed by Speight²¹ as $\ln(d/\bar{r})$, where d is the grain size. All other constants in Eq.[5] have been defined earlier.

For subsequent use of Eq.[5], dispersoids were assumed spherical, with an

effective average radius calculated from the mean intercept length. The term X_B^B was inserted into the denominator of the expression for K' by the present authors in studying the growth of A_mB_n -type particles. No attempt was made to consider the effect of overlapping diffusion fields on the coarsening rate predicted by Kirchner.

A value for the grain boundary diffusion of Fe in Al was obtained from the work of Hirano²² et al.: $D_G = 5.0 \times 10^{-6} \exp (-7.04 \times 10^3/T) \text{ m}^2/\text{s}$. The grain boundary width was taken to be $5 \times 10^{-10} \text{ m}$ and the grain size was taken to be 1 micrometer. A typical value of 1 J/m^2 was used for the particle-matrix interfacial energy in the calculation of the growth rate of the $\text{Al}_{13}\text{Fe}_4$ particles by diffusion along grain boundaries. Since data were unavailable for the grain boundary diffusion of Ce in Al, the calculation was not made for the $\text{Al}_{10}\text{Fe}_2\text{Ce}$ particles.

Table IV compares predicted and measured values of K' for the growth of $\text{Al}_{13}\text{Fe}_4$ particles at 575 and 475°C. (The range of calculated values reflects the slowly changing value of γ as the particles increase in size.) The comparison suggests that grain boundary diffusion is sufficiently rapid to explain the particle growth rate observed during aging at 575°C. The measured growth rate during aging at 475°C is somewhat greater than predicted. This may indicate that dislocation pipe diffusion is important at the lower temperature. Alternatively, the discrepancy may be attributed to the approximations made in the analysis and to the fact that overlapping diffusion fields were not considered.

It is evident that grain boundary diffusion plays a significant role in the coarsening of particles in the Al-Fe-Ce RSP alloy over the temperature range used in this investigation. Particles situated on grain boundaries benefit from the rapid grain boundary diffusion while particles in grain

interiors require pipe diffusion and/or volume diffusion to grow. The TEM micrographs of Fig. 3 show a number of very fine particles in the grain interiors. As the average size of the grain boundary particles becomes larger, these fine particles become increasingly less stable and disappear.

C. Particle Size Distributions

In addition to predicting average particle growth rates, the LSW and MLSW theories state that the shape of the particle size distribution becomes independent of time. This steady state size distribution for the dilute dispersion case is skewed to the left, has its maximum at a particle size 1.135 times the average size and has a cutoff at a particle size 1.5 times the average. The MLSW and LSEM modifications predict similar distributions which broaden with increasing volume fraction of dispersed phase. Kirchner's analysis of coarsening by diffusion along grain boundaries also predicts a quasi-stationary particle size distribution for long aging times. That distribution is also skewed to the left; its maximum occurs at a particle size 1.14 times the average and has a cutoff at a particle size 1.33 times the average. The effect of volume fraction dispersoid on the steady state particle size distribution which evolves during coarsening by this mechanism has not been investigated. Therefore, comparisons between measured and theoretical size distributions will be limited to the case of curves predicted by the MLSW treatment.

For a comparison of experimental histograms to the distribution predicted by the MLSW theory for a system containing 23 volume percent dispersed phase, it was necessary to convert the distribution of the normalized radii of the MLSW theory into a distribution of normalized intercept lengths. Details of the conversion are given in the Appendix. Because the particles of the current study are non-spherical, the experimental histograms representing the coarsening process at 575 and 475°C are compared in Figs. 7 and 8 to the distribution

of intercept lengths expected if random test lines intercept an MLSW assembly of oblate spheroids having aspect ratios of 1.4 and 2.25 at 575 and 475°C, respectively. The aspect ratio was assumed time independent for each assembly; values of 1.4 and 2.25 were chosen because measurements from TEM micrographs of thin foil specimens aged 240 hrs at 575 or 475°C indicated that these were the appropriate averages. Error bars on the experimental histograms were established by taking the square root of the number of intercept lengths measured for each size class and normalizing these by the same factor used to normalize $f(L/\bar{L})$.

The experimental and theoretical distributions both have a log normal shape but the experimental histograms have longer tails at the large intercept length sides than predicted. The B-W theory is, of course, based on spherical particles thus poor agreement with experimental data is not unexpected; however, the tails may be caused by the presence of particles which lie along dislocations or grain boundaries and hence receive a greater supply of solute. The experimental histograms also have their peaks at smaller values of L/\bar{L} than expected. Some error may have been introduced into the theoretical distribution by assuming that all the oblate spheroids in an assembly have the same aspect ratio. Choice of a larger value for the aspect ratio would lead to a better match of the experimental and theoretical distributions. While use of a normalized intercept length distribution is advantageous in systems having non-spherical particles because one is able to obtain histograms from raw data and easily assign error bars to the histograms, it is much less discriminating than a normalized distribution of radii. This point is illustrated in Fig. 9. The $f(L/\bar{L})$ versus L/\bar{L} distribution generated by passing random test lines through a Brailsford and Wynblatt distribution

of spheres (curve A) is compared to the $f(L/\bar{L})$ versus L/\bar{L} distribution generated by passing random test lines through a very different distribution of spheres (curve B). The particle size distribution used to generate curve B is triangular; on a plot of $f(\rho)$ versus ρ , the distribution is defined by the equation

$$f(\rho) = -\frac{2\rho}{\rho_{\max}^2} + 2/\rho_{\max} \quad [6]$$

where ρ_{\max} is the value of ρ above which $f(\rho)$ in the Brailsford and Wynblatt distribution is zero. To obtain Fig. 9, ρ_{\max} was taken to be 1.75, the value appropriate for a system containing 23 volume percent dispersed phase. Curve A and curve B are very similar despite the fact that the actual particle size distributions are very different.

IV. CONCLUSIONS

1. At least two equilibrium dispersed phases are present in the Al-Fe-Ce system: $Al_{13}Fe_4$ and $Al_{10}Fe_2Ce$.
2. Coarsening of the dispersed phases in the RSP P/M Al-Fe-Ce alloys occurs much more rapidly than calculated from bulk diffusion controlled theory using published values for diffusivity and solubility of Fe and Ce in Al. However, the expected linear relation between particle dimension cubed and time is found for aging temperatures of 475 and 575°C. Grain boundary diffusion plays a significant role in coarsening at these temperatures.
3. Experimental histograms of intercept length differ somewhat from the distributions of intercept lengths generated by random test lines passing through an MLSW distribution of oblate spheroids. The shape of a histogram of intercept lengths is seen to be insensitive to the form of the actual particle size distribution. STEM analysis of the dispersed phase

particles shows no evidence for a bimodal distribution of particle sizes.

APPENDIX

For an oblate spheroid with $2a \geq 2b$, where $2a$ is the length along the major axis and $2b$ is the length along the minor axis, the surface area is given by²³:

$$\bar{S} = 2\pi a^2 + \pi(b^2/\epsilon) \ln [(1+\epsilon)/(1-\epsilon)] \quad . \quad [A.1]$$

The term ϵ is defined as $\epsilon = [1 - (b/a)^2]^{\frac{1}{2}}$. For a distribution of spheroids, $N_V(D)$, where $N_V(D)dD$ is the number of spheroids per unit volume with a length along the major axis of $D \pm dD/2$, the expected number of interceptions of a probe with a body, \bar{N}_L , is related to the surface area, \bar{S} , by the following expression²³:

$$\bar{N}_L = N_V \bar{S} / 4 \quad . \quad [A.2]$$

The distribution $N_V(D)$ is the MLSW distribution for which an analytical expression is available.¹² To determine the probability that the interception will be of length $L + dL/2$, a single spheroid is considered.

The intercept length distribution obtained when a linear probe passes through a single spheroid, $g(L)$ versus L , was determined by running a Monte Carlo simulation for each of the two aspect ratios considered. The direction of the probe, defined by θ and ϕ , was randomly varied. Simultaneously, its position defined by x and y was randomly varied.

The probability for each intercept length was summed over the entire MLSW distribution of spheroid sizes using the expression:

$$N(L) = A \int_L^D g(L) \{ [2\pi a^2 + \pi(b^2/\epsilon) \ln [(1+\epsilon)/(1-\epsilon)]] / 4 \} N_V(D) dD \quad . \quad [A.3]$$

The numerical integration is taken from L to D since the smallest spheroid which can contribute an intercept length of L has a length along the major axis

of L. The constant A serves to normalize the distribution.

ACKNOWLEDGEMENTS

The authors are grateful for the support of this work by the Air Force Office of Scientific Research through Grant No. AFOSR-82-0005B. In this research extensive use was made of the facilities of Northwestern University's Materials Research Center, supported in part under the NSF-MRL program (Grant No. DMR82-16972). One of the authors (L.A.) would like to thank the Zonta Organization for their gift of the Amelia Earhart Fellowship Award. The alloys were kindly provided by the Air Force Materials Laboratory through Ms. S. Kirchoff and Dr. W. M. Griffith, Jr. We thank Dr. G. J. Hildeman of Alcoa Research Laboratories for the many helpful discussions during the course of the research.

REFERENCES

1. W. M. Griffith, Jr., R. E. Sanders, Jr. and G. J. Hildeman: High Strength Powder Metallurgy Aluminum Alloys, M. J. Koczak and G. J. Hildeman, eds., Conf. Proceedings, TMS-AIME, 1982, p. 209.
2. R. E. Sanders, Jr. and G. J. Hildeman: Elevated Temperature Aluminum Alloy Development, AFWAL-TR-8-4076, September 1981, Alcoa Technical Center, PA.
3. O. S. Zarechnyuk, M. G. Mys'kiv and V. R. Ryabov: Russian Metallurgy, 1969, No. 2, p. 133.
4. P. J. Black: Acta crystallogr., 1955, vol. 8, p. 175.
5. L. Angers, M. E. Fine, M. Raghavan and J. R. Weertman: Northwestern University, Evanston, IL and Exxon Research & Engineering Co., Annandale, NJ, unpublished research, 1985.
6. E. E. Underwood: in Quantitative Stereology, Addison-Wesley Pub. Co., Reading, MA, 1970, pp. 25-35.
7. I. M. Lifshitz and V. V. Slyozov: Phys. Chem. Solids, 1961, vol. 19, p. 35.
8. C. Wagner: Z. Electrochem., 1961, vol. 65, p. 581.

9. H. O. K. Kirchner: Metall. Trans., 1971, vol. 2, p. 2861.
10. H. Kreye: Z. Metallkde., 1970, vol. 61, p. 108.
11. A. J. Ardell: Acta Metall., 1972, vol. 20, p. 61.
12. A. D. Brailsford and P. Wynblatt: Acta Metall., 1979, vol. 27, p. 489.
13. K. Tsumuraya and V. Miyata: Acta Metall., 1983, vol. 31, p. 437.
14. C. K. L. Davies, P. Nash and R. N. Stevens: Acta Metall., 1980, vol. 28, p. 179.
15. D. Janoff and M. E. Fine: Mat. Sci. Eng., 1984, vol. 64, p. 67.
16. K. Sorenson and G. Trumpy: Phys. Rev. B1, 1973, vol. 7, p. 1791.
17. S. P. Murarka and R. P. Agarwala: Indian Atomic Energy Commission Rept. BARC-368, 1968.
18. L. A. Willey: in Metals Handbook - Metallurgy, Structures and Phase Diagrams, Vol. 8, 1973, p. 260.
19. L. F. Mondolfo: in Aluminum: Structure and Properties, Butterworths, London-Boston, 1976, p. 242.
20. T. Wilkinson: M.S. Thesis, Northwestern University, Evanston, IL, 1983.
21. M. V. Speight: Acta Metall., 1968, vol. 16, p. 133.
22. K. I. Hirano, R. P. Agarwala and M. Cohen: Acta Metall., 1962, vol. 10, p. 857.
23. J. E. Hilliard: Northwestern University, Evanston, IL, unpublished research, 1985.

Table I. Interplanar Spacings for Dispersed Phases in the Al-7.5Fe-3.4Ce
RSP P/M Alloy Aged at 475°C and 575°C for Times from 24 to 240 Hrs

d (nm)	I/I ₀	d (nm)*	I/I ₀ *	Compound
0.690	10	0.7089	16	Al ₁₃ Fe ₄
0.671	10	0.6729		Al ₁₀ Fe ₂ Ce (110)
0.652	10	0.6523	22	Al ₁₃ Fe ₄
0.543-0.551	10	0.5402		Al ₁₀ Fe ₂ Ce (111)
0.511-0.519	10-20	0.5110		Al ₁₀ Fe ₂ Ce (020)
0.431-0.452	10-20	0.4530		Al ₁₀ Fe ₂ Ce (002)
		0.4470		Al ₁₀ Fe ₂ Ce (200)
		0.4510		Al ₁₀ Fe ₂ Ce (021)
0.405-0.410	10-35	0.4064	29	Al ₁₃ Fe ₄
0.401	10-15	0.4008		Al ₁₀ Fe ₂ Ce (201)
		0.4001	75	Al ₁₃ Fe ₄
0.391-0.396	10-45	0.3872	8	Al ₁₃ Fe ₄
0.381-0.386	15-45	0.3826	3	Al ₁₃ Fe ₄
0.367-0.377	10-35	0.3758		Al ₁₀ Fe ₂ Ce (112)
		0.3682	60	Al ₁₃ Fe ₄
0.324-0.327	10	0.3268	30	Al ₁₃ Fe ₄
0.3225	20	0.3234	7	Al ₁₃ Fe ₄
0.317-0.320	10-30	0.3183		Al ₁₀ Fe ₂ Ce (130)
		0.3182		Al ₁₀ Fe ₂ Ce (202)
		0.3154		Al ₁₀ Fe ₂ Ce (221)
0.3005-0.303	10-15	0.3003		Al ₁₀ Fe ₂ Ce (131)
0.290-0.288	10	0.2861		Al ₁₀ Fe ₂ Ce (310)
0.275-0.277	10-15	0.2755		Al ₁₀ Fe ₂ Ce (113)
0.261-0.262	30-35	0.2605		Al ₁₀ Fe ₂ Ce (132)
0.258	15-30	0.2600		Al ₁₀ Fe ₂ Ce (023)
		0.2561	6	Al ₁₃ Fe ₄
0.243-0.244	25	0.2465	5	Al ₁₃ Fe ₄
		0.2419		Al ₁₀ Fe ₂ Ce (312)
0.228	10-20	0.2276	3	Al ₁₃ Fe ₄
0.2265-0.227	70	0.2265		Al ₁₀ Fe ₂ Ce (004)
		0.2261	17	Al ₁₃ Fe ₄
0.223-0.224	100	0.2247		Al ₁₀ Fe ₂ Ce (223)
		0.2243		Al ₁₀ Fe ₂ Ce (330)
		0.2235		Al ₁₀ Fe ₂ Ce (400)
0.220	15	0.2177		Al ₁₀ Fe ₂ Ce (331)
		0.2174	3	Al ₁₃ Fe ₄
		0.2170		Al ₁₀ Fe ₂ Ce (401)
0.211	30	0.2120	85	Al ₁₃ Fe ₄
0.209-0.210	30-70	0.209	138	Al ₁₃ Fe ₄
		0.2077		Al ₁₀ Fe ₂ Ce (313)
0.206	30	0.2056	111	Al ₁₃ Fe ₄
		0.2071		Al ₁₀ Fe ₂ Ce (024)
		0.2048		Al ₁₀ Fe ₂ Ce (420)
0.201	10-20	0.2020		Al ₁₀ Fe ₂ Ce (204)
		0.2010		Al ₁₀ Fe ₂ Ce (332)
		0.2004	131	Al ₁₃ Fe ₄
		0.2004		Al ₁₀ Fe ₂ Ce (402)
		0.2000		Al ₁₀ Fe ₂ Ce (421)
0.194	20-25	0.1951		Al ₁₀ Fe ₂ Ce (043)
		0.1938	24	Al ₁₃ Fe ₄

CONTINUED

Table I. Interplanar Spacings for Dispersed Phases in the Al-7.5Fe-3.4Ce
RSP P/M Alloy Aged at 475°C and 575°C for Times from 24 to 240 Hrs

d (nm)	I/I ₀	d (nm)*	I/I ₀ *	Compound
0.1834	10	0.1846	2	Al ₁₀ Fe ₂ Ce (134)
0.1828	10	0.1827		Al ₁₃ Fe ₄
0.160	10	0.1594		Al ₁₀ Fe ₂ Ce (334)
0.159	30	0.1591		Al ₁₀ Fe ₂ Ce (404)
0.158	10	0.1585		Al ₁₀ Fe ₂ Ce (244)
0.157	10	0.1577		Al ₁₀ Fe ₂ Ce (442)

* Interplanar spacings and relative intensities obtained from references
4 and 5.

Table II. Values of Mean Particle Intercept Length after Isothermal Annealing in the Al-7.5Fe-3.4Ce RSP Alloy

Temperature (°C)	Time (hrs)	Mean Intercept Length* (μm)
575	2	$0.43 \pm .06$
575	12	$0.70 \pm .05$
575	24	$0.87 \pm .09$
575	120	$1.10 \pm .08$
575	240	$1.48 \pm .19$
475	2	$0.24 \pm .02$
475	12	$0.33 \pm .04$
475	24	$0.34 \pm .02$
475	120	$0.53 \pm .05$
475	240	$0.67 \pm .07$

* \pm refers to 95% confidence intervals about the mean value

Table III. Measured and Calculated Values of Coarsening Rate Constants in the Al-7.5Fe-3.4Ce RSP Alloy

Temperature	K Measured ($\mu\text{m}^3/\text{hr}$)	$K^{\text{Al}_{13}\text{Fe}_4}$ Calculated* ($\mu\text{m}^3/\text{hr}$)	$K^{\text{Al}_{10}\text{Fe}_2\text{Ce}}$ Calculated* ($\mu\text{m}^3/\text{hr}$)
575°C	3.17×10^{-3}	1.68×10^{-4}	1.07×10^{-7}
475°C	3.07×10^{-4}	3.64×10^{-6}	7.12×10^{-9}

* Diffusion control approximation

Table IV. Measured and Calculated Values of Coarsening Rate Constants for Growth by Diffusion Along Grain Boundaries in the Al-7.5Fe-3.4Ce RSP Alloy

Temperature	K' Measured ($\mu\text{m}^4/\text{hr}$)	$K'^{\text{Al}_{13}\text{Fe}_4}$ Calculated ($\mu\text{m}^4/\text{hr}$)
575°C	3.3×10^{-2}	1.0×10^{-2} to 2.1×10^{-1}
475°C	2.2×10^{-3}	6.9×10^{-4} to 1.5×10^{-3}

FIGURE CAPTIONS

- Figure 1. TEM micrographs of replicas of samples aged at 575°C in vacuum of 1.1×10^{-3} Pa: (a) 2 hrs, (b) 12 hrs, (c) 24 hrs, and (d) 120 hrs.
- Figure 2. TEM micrographs of replicas of samples aged at 475°C in vacuum of 1.1×10^{-3} Pa: (a) 2 hrs, (b) 12 hrs, (c) 24 hrs, and (d) 240 hrs.
- Figure 3. TEM micrographs of thin foils of Al-7.5Fe-3.4Ce: (a) aged 2 hrs at 575°C, (b) aged 12 hrs at 475°C.
- Figure 4. Volume fraction of the dispersed phases versus aging time for the Al-7.5Fe-3.4Ce alloy aged at 475°C and 575°C.
- Figure 5. Least squares correlation coefficient, R , versus exponent, n , for aging of the Al-7.5Fe-3.4Ce alloy at 475°C and 575°C.
- Figure 6. Particle mean intercept length cubed, \bar{L}^3 , versus aging time for the Al-7.5Fe-3.4Ce alloy aged at 475°C and 575°C.
- Figure 7. Normalized intercept length histograms during the aging of the Al-7.5Fe-3.4Ce alloy at 575°C: (a) 2 hrs, (b) 12 hrs, (c) 24 hrs and (d) 120 hrs. Dashed curve is the normalized intercept length distribution predicted for the steady state case by the Brailsford and Wynblatt modification to the LSW theory.
- Figure 8. Normalized intercept length histograms during the aging of the Al-7.5Fe-3.4Ce alloy at 475°C: (a) 2 hrs, (b) 12 hrs, (c) 24 hrs and (d) 120 hrs. Dashed curve is the normalized intercept length distribution predicted for the steady state case by the Brailsford and Wynblatt modification to the LSW theory.
- Figure 9. Normalized intercept length distributions predicted for a Brailsford and Wynblatt distribution of spheres (curve A) and a triangular distribution of spheres (curve B).



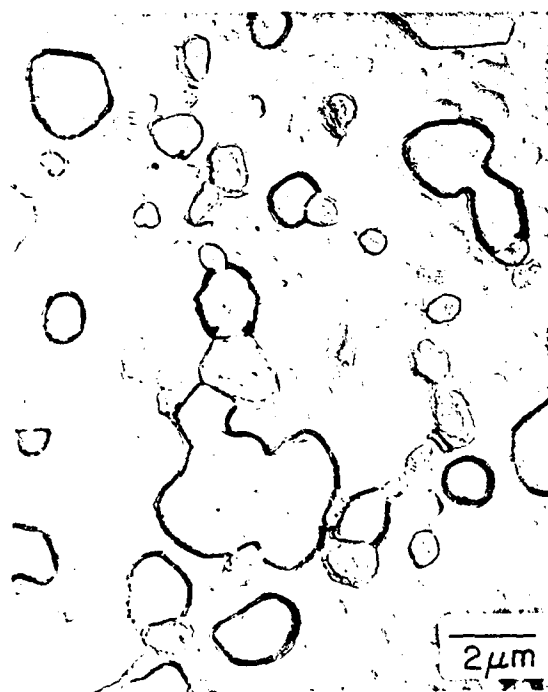
(a)



(b)



(c)



(d)

Fig. 1. TEM micrographs of replicas of samples aged at 575°C in vacuum of 1.1×10^{-5} Pa: (a) 2 hrs, (b) 12 hrs, (c) 24 hrs, and (d) 120 hrs.



(a)



(b)



(c)



(d)

Fig. 2. TEM micrographs of replicas of samples aged at 475°C in vacuum of 1.1×10^{-5} Pa: (a) 2 hrs, (b) 12 hrs, (c) 24 hrs, and (d) 240 hrs.

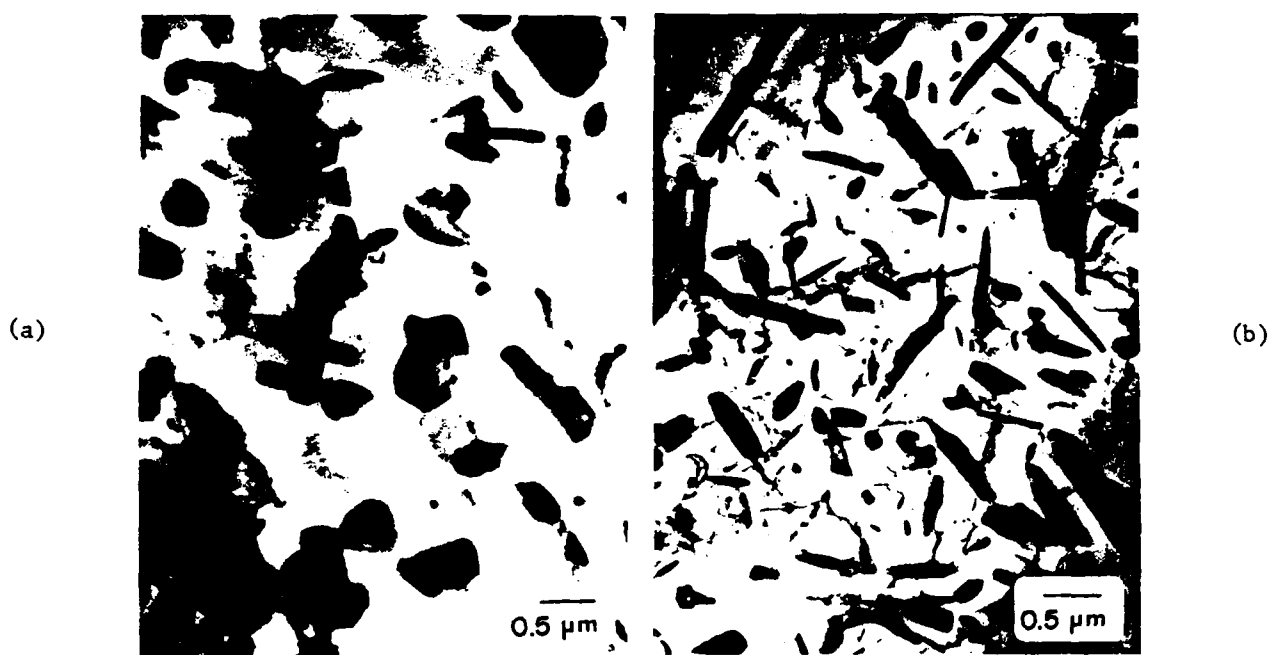


Fig. 3. TEM micrographs of thin foils of Al-7.5Fe-3.4Ce: (a) aged 2 hrs at 575°C, (b) aged 12 hrs at 475°C.

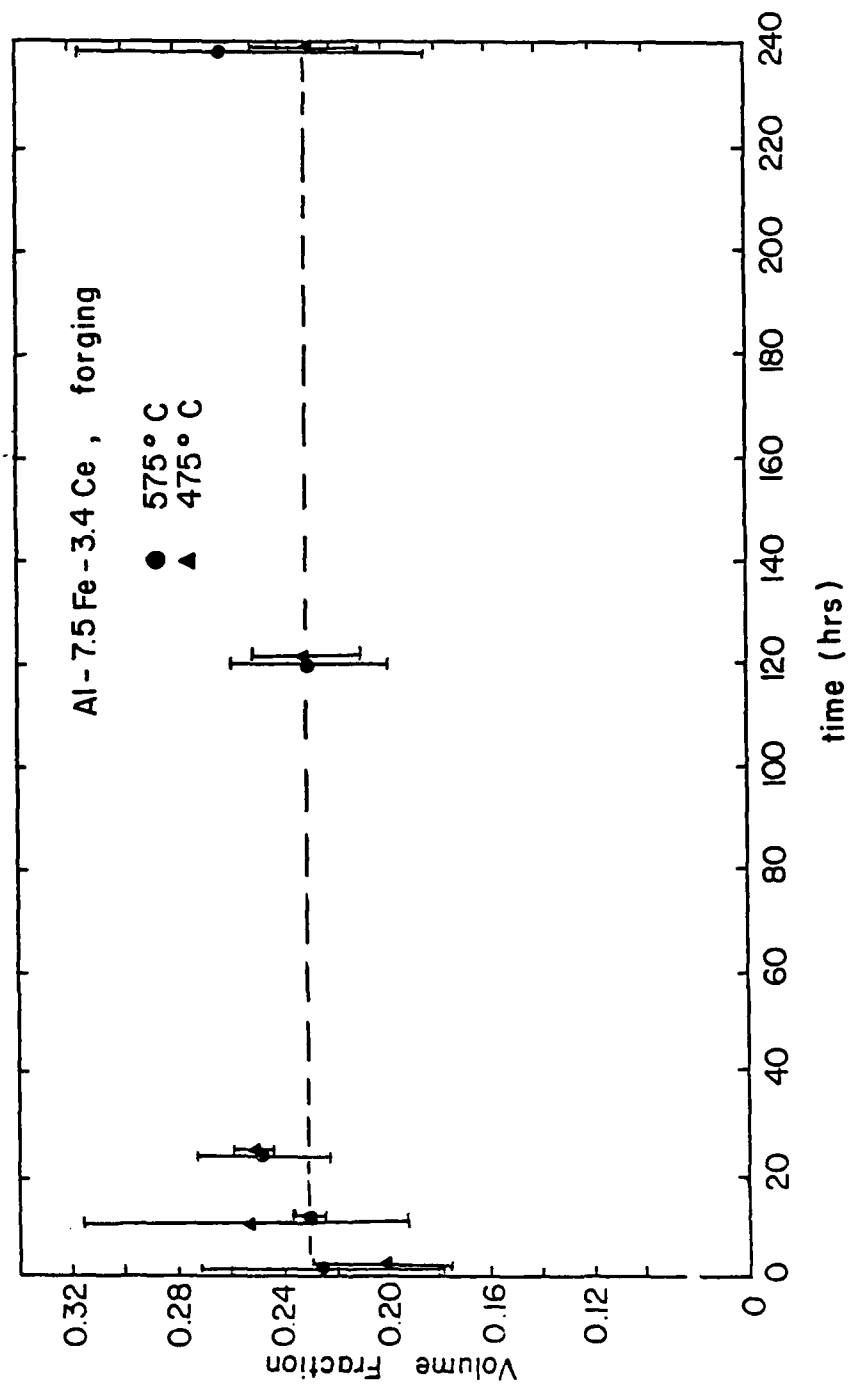


Fig. 4. Volume fraction of the dispersed phases versus aging time for the Al-7.5Fe-3.4Ce alloy aged at 475°C and 575°C.

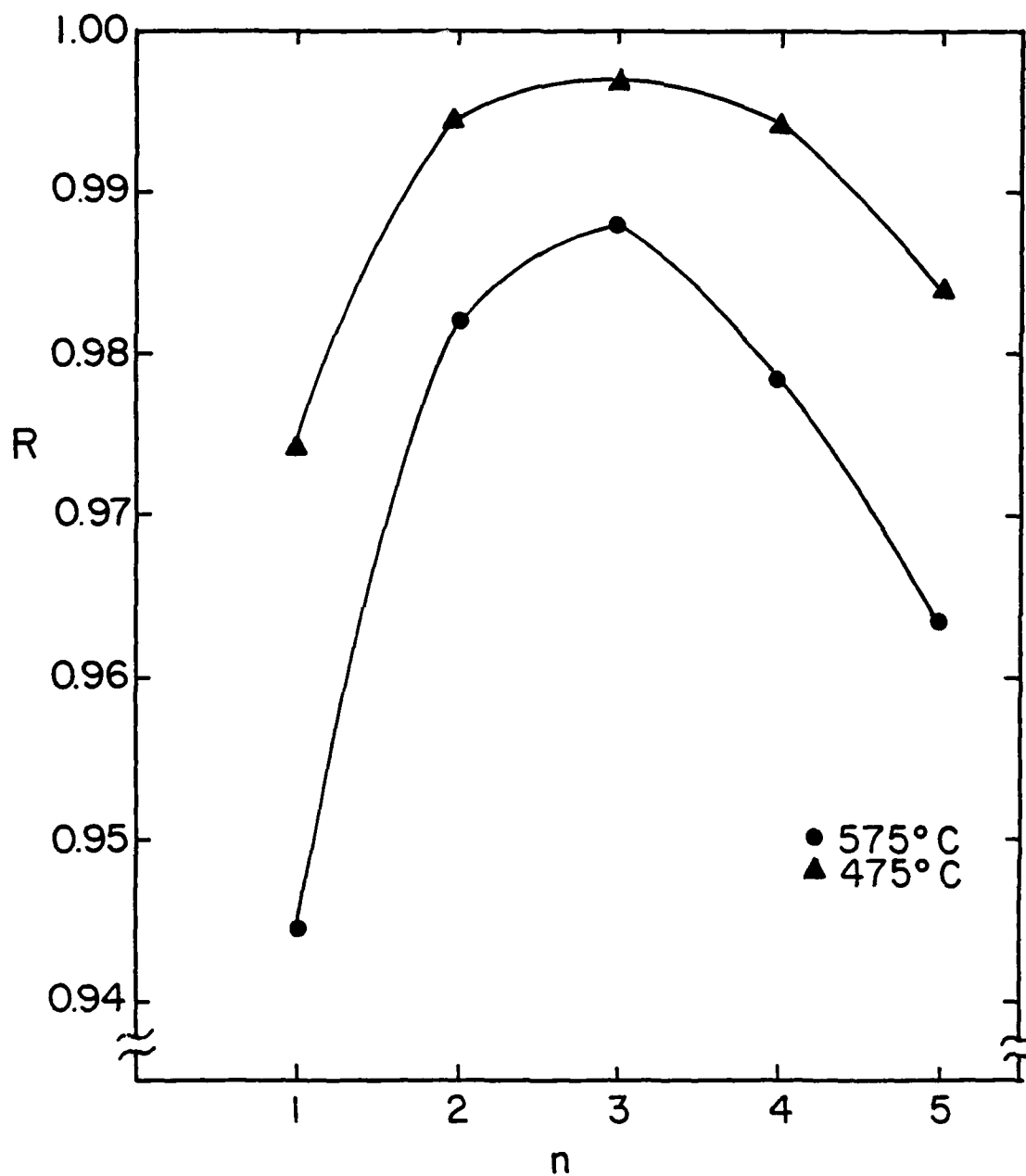


Fig. 5. Least squares correlation coefficient, R , versus exponent, n , for aging of the Al-7.5Fe-3.4Ce alloy at 475°C and 575°C.

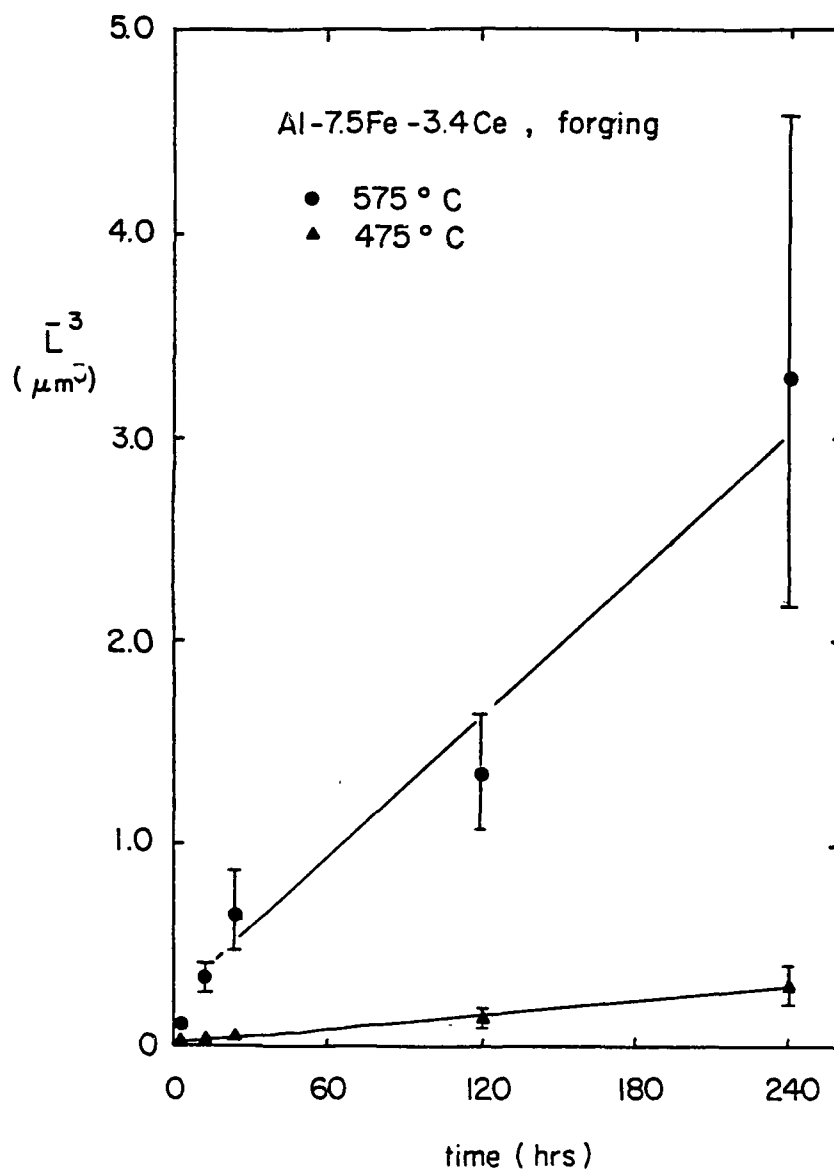


Fig. 6. Particle mean intercept length cubed, \bar{L}^3 , versus aging time for the Al-7.5Fe-3.4Ce alloy aged at 475°C and 575°C.

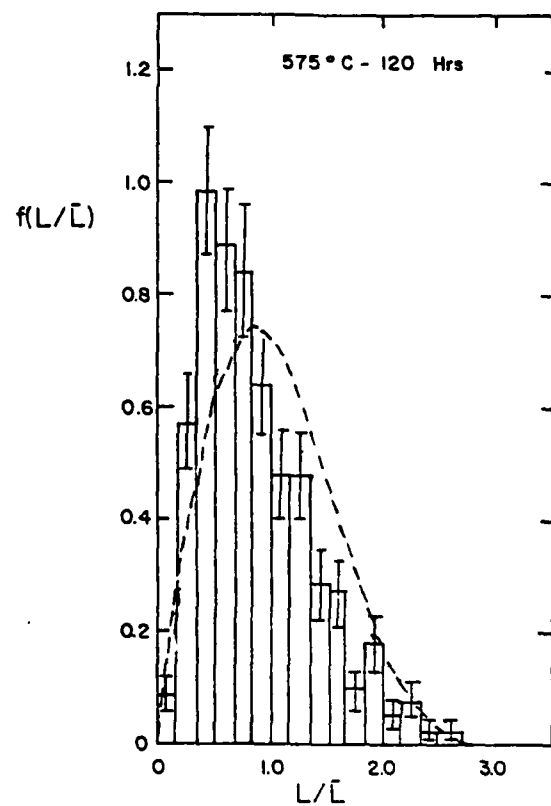
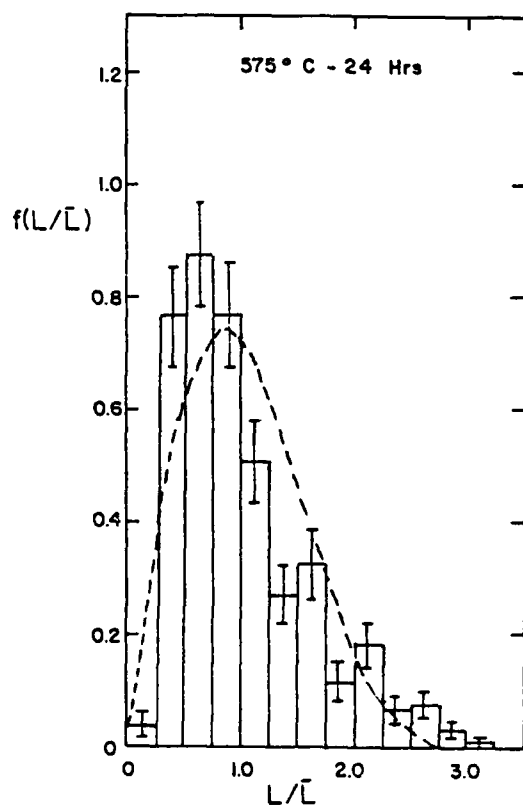
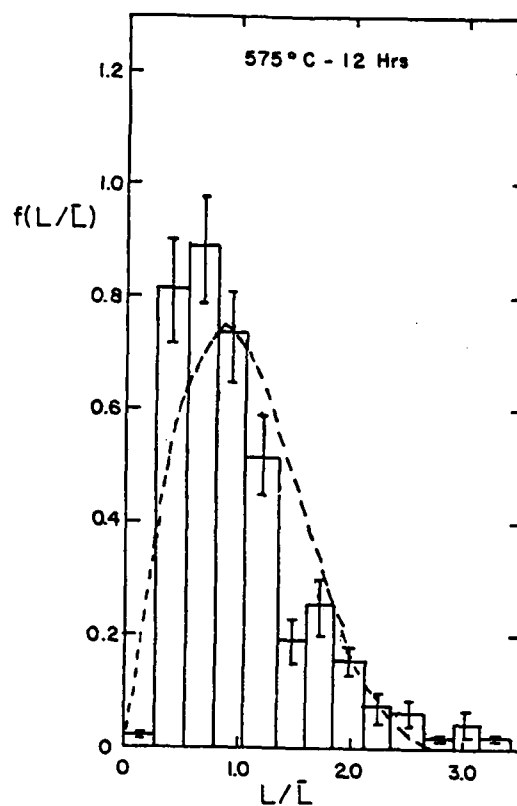
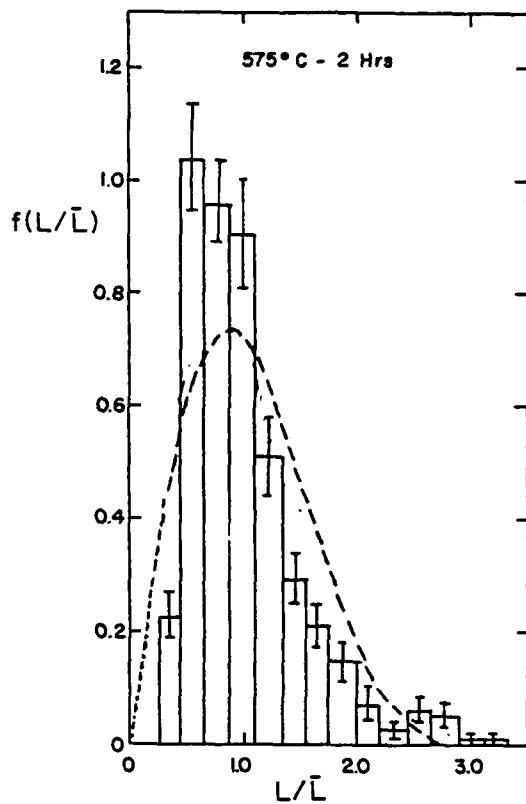


Fig. 7. Normalized intercept length histograms during the aging of the Al-7.5Fe-3.4Ce alloy at 575°C: (a) 2 hrs, (b) 12 hrs, (c) 24 hrs and (d) 120 hrs. Dashed curve is the normalized intercept length distribution predicted for the steady state case by the Brailsford and Wynblatt modification to the LSW theory.

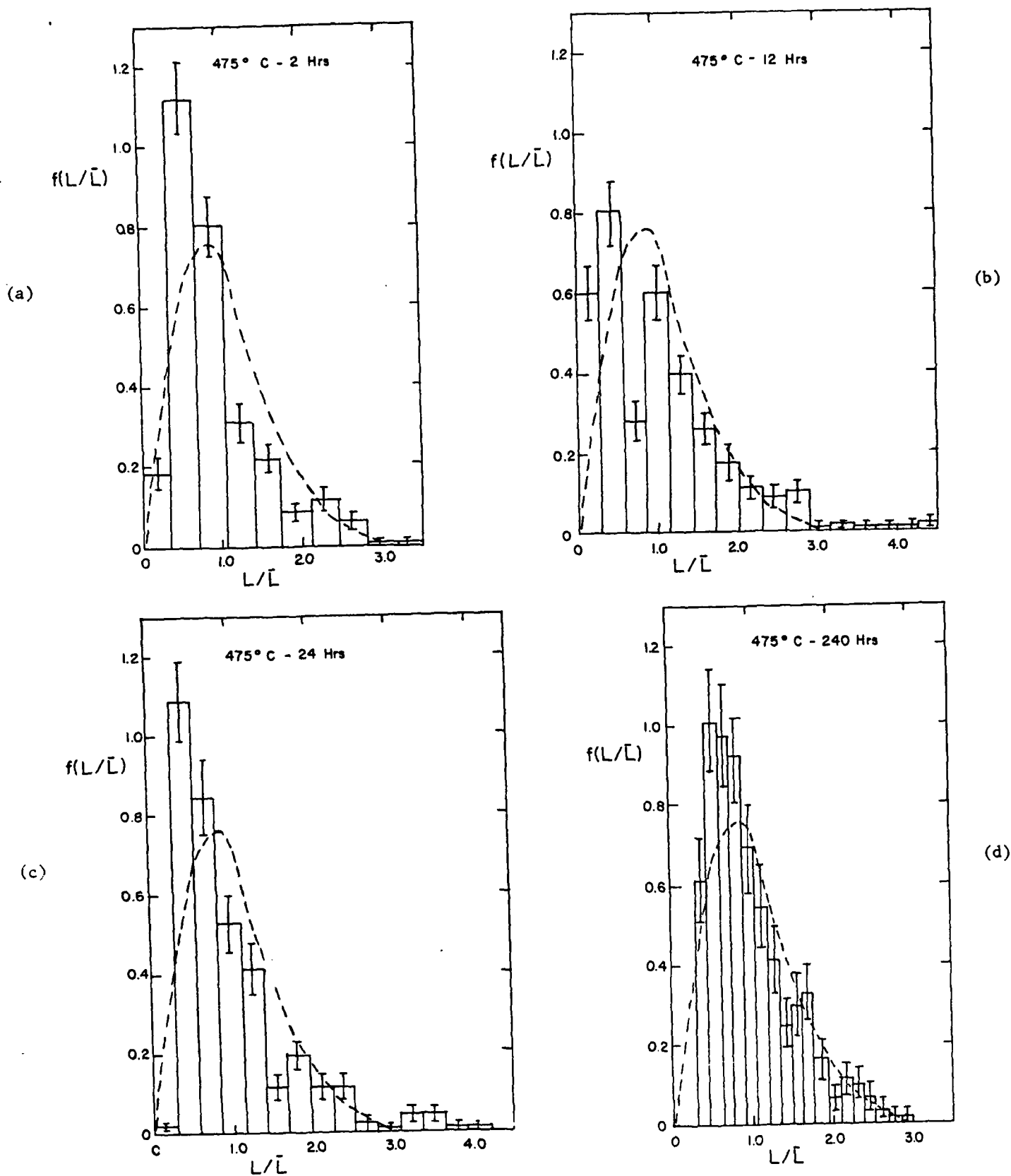


Fig. 8. Normalized intercept length histograms during the aging of the Al-7.5Fe-3.4Ce alloy at 475°C: (a) 2 hrs, (b) 12 hrs, (c) 24 hrs and (d) 120 hrs. Dashed curve is the normalized intercept length distribution predicted for the steady state case by the Brailsford and Wynblatt modification to the LSW theory.

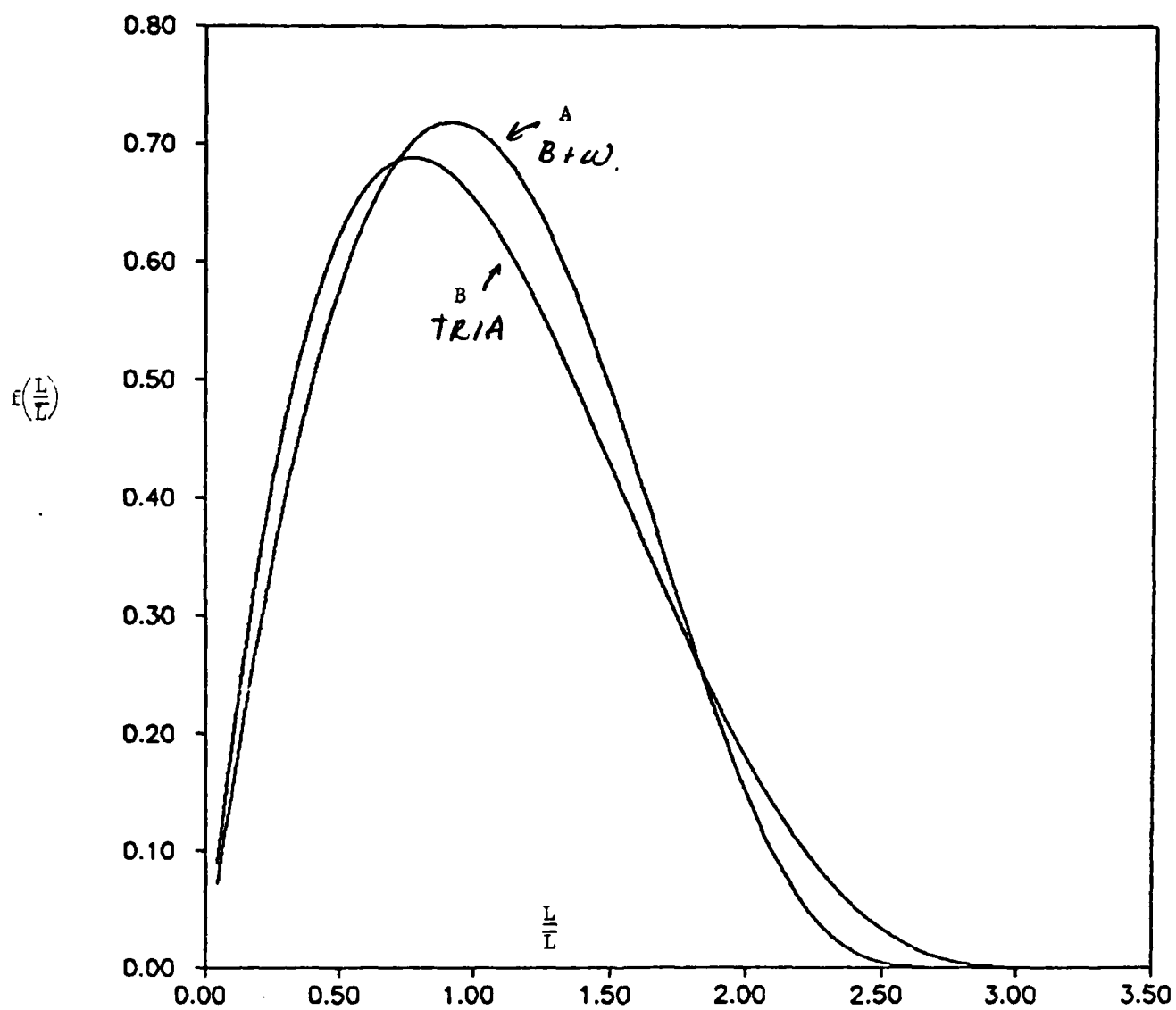


Fig. 9. Normalized intercept length distributions predicted for a Brailsford and Wynblatt distribution of spheres (curve A) and a triangular distribution of spheres (curve B).

EFFECT OF PLASTIC DEFORMATION ON THE COARSENING KINETICS
OF DISPERSOIDS IN A RAPIDLY SOLIDIFIED Al-Fe-Ce ALLOY

L. Angers*, M. E. Fine and J. R. Weertman
Department of Materials Science & Engineering and
Materials Research Center, Northwestern University
Evanston, IL 60201 USA

ABSTRACT

Particle coarsening has been studied in a rapidly solidified Al-8.8 wt.% Fe-3.7 wt.% Ce alloy subjected to isothermal annealing for various times at 425°C. The effect of static and dynamic loading on the particle coarsening rates at the same temperature also has been examined. The dispersed particles in all specimens of the present study are the equilibrium $\text{Al}_{13}\text{Fe}_4$ and $\text{Al}_{10}\text{Fe}_2\text{Ce}$ phases. They are incoherent with the matrix and constitute 23 percent of the total volume.

The coarsening rate in isothermally annealed specimens is orders of magnitude greater than predicted by the modified Lifshitz-Slyozov-Wagner theory for volume diffusion controlled coarsening but can be explained using Kirchner's model for coarsening by diffusion along grain boundaries. Creep loading is seen to cause a significant enhancement of the coarsening kinetics. Fatigue testing with a hold period at the maximum tensile stress also accelerates coarsening whereas continuous cycling appears to initially retard particle growth. Dislocations connecting dispersed phase particles are observed more frequently in crept specimens and specimens fatigued with a hold period than in specimens fatigued with no hold period. The effects of plastic deformation on particle coarsening rates are discussed in terms of excess vacancy generation, short circuiting along dislocations and fine precipitation during fatigue.

* Present address: Alcoa Technical Center, Alloy Technology Division,
Alcoa Center, PA 15069

I. INTRODUCTION

Aluminum alloys produced by rapid solidification processing (RSP) have great potential for elevated temperature applications. These alloys contain a high volume fraction of dispersed phases which provide higher room temperature strength and elastic modulus than are obtainable by conventional ingot metallurgy. In addition, the RSP alloys retain their desirable properties up to higher temperatures than do the ingot metallurgy alloys. One such RSP alloy, the Al-8 wt.% Fe-4 wt.% Ce alloy prepared at Alcoa, exhibits promising mechanical properties at temperatures up to 316°C.¹ Exposure to higher temperatures leads to significant coarsening, transformation of metastable phases, and subsequent loss of strength.

Plastic deformation may affect the stability of the dispersed phases by increasing diffusion rates and assisting in the nucleation of more stable phases. Diffusion rates may be increased by the generation of excess vacancies or by short circuiting along dislocations and grain or sub-grain boundaries. While the subject of strain enhanced diffusion has received much discussion in past years²⁻⁴, little attention has been paid to the influence of plastic deformation on particle coarsening rates. Therefore, the effect of static and cyclic deformation at 425°C on microstructural stability in an Al-8.8 wt.% Fe-3.7 wt.% Ce alloy was examined. Coarsening rates in these specimens have been compared to the coarsening rates in specimens isothermally annealed at the same temperature. The coarsening kinetics at even higher temperatures in an RSP Al-Fe-Ce alloy of similar composition have been reported in a companion paper.⁵

II. EXPERIMENTAL PROCEDURE

An Al-8.8 wt.% Fe-3.7 wt.% Ce alloy, developed at Alcoa under AFML

Grant No. F33615-77-C-5086, was obtained from Wright-Patterson Air Force Base in plate form prepared by gas atomization, cold isostatic pressing, hot vacuum pressing and finally extrusion. To study the effect of deformation on the coarsening kinetics in this system, isothermal annealing and both creep and load control fatigue tests were done. Creep specimens were flat with gage section dimensions of 6 mm length \times 2.8 \times 2 mm² cross section. Round threaded fatigue specimens had both a gage diameter and gage length of 4.77 mm. Prior to testing, all specimens were polished to a 0.3 μ m finish. Preliminary creep tests were run at 316, 375 and 425°C to determine whether any effect of deformation on the coarsening rate could be detected. To obtain a quantitative measure of the extent of the enhancement, a series of specimens were either isothermally aged at 425°C, crept at 425°C under an initial stress of 17.2 MPa or fatigued in load control at 425°C and stress amplitudes of 34.4 or 68.8 MPa and frequencies of 0.1 Hz. Creep elongation was monitored using an LVDT. Two specimens were fatigued 120 hrs at 425° with a hold period at the maximum tensile stress of 15 seconds and 120 seconds.

After the tests, TEM micrographs of shadowed two stage replicas of surfaces of sectioned specimens were obtained for observation and subsequent quantitative metallography. A point counting technique was used to calculate the volume fraction, V_v , taken up by the dispersed phases.⁶ The surface area, S_v , per unit volume of particle-matrix interface was calculated from the number of intersections of precipitates with grid lines.⁸ A value for the particle mean intercept length, \bar{L} , for each aging time and temperature combination, was obtained from the volume fraction and surface area per unit volume using the formula⁶:

$$\bar{L} = 4V_v/S_v \quad [1]$$

Equation [1] is valid for any particle shape. Additionally, thin foil

specimens were prepared by jet polishing in a 20% nitric acid-methanol solution cooled by a dry ice-methanol bath. The current density used to provide a polished surface was 3 A/cm^2 . These specimens were examined for evidence of dislocation-particle interactions. Microhardness measurements for each specimen were taken using a 300 gram load with a Vickers hardness indenter. X-ray diffraction scans were done to determine whether dispersed phase structures were changing with time.

III. RESULTS AND DISCUSSION

A. Particle Growth Rates During Isothermal Annealing at 425°C

Figure 1 shows TEM micrographs of thin foil specimens of Al-8.8 wt.% Fe-3.7 wt.% Ce after aging 24 and 240 hrs at 425°C . After 24 hrs of aging, both coarse grain boundary particles and fine particles within grain interiors are observed. Some particles are equiaxed while others are elongated. After 240 hrs of aging, the average particle size is obviously larger. Figure 2 shows the particle mean intercept length, \bar{L} , as a function of aging time at 425°C . The error bars in this figure and in all subsequent figures were established by obtaining a measure of \bar{L} from several regions of the same specimen and determining the 95% confidence interval about the mean value. After an initial rapid increase in \bar{L} , particle growth slows down. Grain size has been plotted as a function of aging time in Figure 3. A small degree of grain growth is observed initially but the grain size stabilizes to 1 micrometer during aging at this temperature.

The particle mean intercept length data obtained from specimens aged at 425°C were examined using a number of theoretically predicted growth laws. A number of models for Ostwald ripening, after an initial transient, predict an equation of the form

$$\bar{r}^n - \bar{r}_0^n = Kt \quad [2]$$

where \bar{r} is the appropriate average particle size, \bar{r}_0 is an integration constant, and n and K depend on the model. The Lifshitz-Slyozov-Wagner (LSW) theory for volume diffusion control of coarsening for small volume fractions of spherical particles^{7,8} predicts n of 3 and a proportionality constant

$$K_3 = \frac{8D_v \sigma C_o \Omega^2}{9kT} \quad [3]$$

Here, σ is the interfacial energy, D_v is the bulk diffusivity of solute in the matrix, C_o is the equilibrium solid solubility limit of solute in the matrix, Ω is the atomic volume of solute in the dispersed phase and k and T have their usual meanings.

Kirchner's⁹ model for coarsening by diffusion along grain boundaries, also a dilute mixture model, predicts $n = 4$ and

$$K_4 = 9C_o D_G \sigma w \Omega^2 / 64 XY kT \quad [4]$$

Here, D_G is the grain boundary diffusion coefficient and w is the grain boundary width. The constant $X = (2-3m+m^2)/3$, where m is half the ratio of the grain boundary energy to the particle-matrix interfacial energy and $Y = 0.5 \ln(1/f)$, where f is the average area fraction occupied by particles on the grain boundaries. The quantity Y has also been expressed by Speight¹⁰ as $\ln(d/\bar{r})$, where d is the grain size.

For the coarsening of particles by diffusion along dislocation lines, Kreye¹⁰ obtained $n = 5$ and

$$K_5 = (4/5)^5 (5\sigma qz D_p \Omega^2 C_o) / 4\pi kT \quad [5]$$

Here, D_p is the coefficient for diffusion along dislocations, q is the transverse cross sectional area of a dislocation pipe and z is the number of dislocations attached to each particle.

For subsequent use of the preceding equations, the term x_B^β was inserted into the denominator of the expressions for K_i ($i = 3, 4, 5$) by the present authors¹² to consider the coarsening of particles containing more than one component. The term x_B^β is the atom fraction of B atoms in a β type particle. Since the volume fraction of particles in the present case is not small, a correction factor, obtained from the work of Brailsford and Wynblatt¹³, was applied to the VDC case Eq.3. This correction factor takes into account the overlapping of diffusion fields in a system containing a large volume fraction of particles (23%). Because Eqns. [4] and [5] were developed assuming a low volume fraction of dispersed phase, and because no treatment of the effect of volume fraction on the rate of coarsening by diffusion along grain boundaries or dislocations is available, the effect of overlapping diffusion fields has been neglected when using these equations.

Values for K_3 , K_4 and K_5 were calculated from Eqns. [2-5], modified as described above for comparison to the measured growth rates. The measured growth rates are the experimentally determined slopes of \bar{r}^3 versus t , \bar{r}^4 versus t and \bar{r}^5 versus t . The mean intercept lengths were converted to average effective radii using the relationship $\bar{r} = (2/\pi)\bar{L}$. A least squares analysis of the experimental data indicates that the relationship between \bar{r}^n and t is most nearly linear for $n = 5$, although the approximation to a linear fit is almost as good for n equal to 3 or 4¹⁴, all of these R values being larger than 0.95. This is in contrast to aging at 475 and 575°C where the best fit⁵ was for $n = 3$.

The quantities required for calculating particle growth rates were obtained from the literature. The atomic volumes of Fe in $Al_{13}Fe_4$ and of Ce in $Al_{10}Fe_2Ce$ were calculated from lattice parameter information^{15,16} to be 1.49×10^{-29} m³/atom and 1.60×10^{-29} m³/atom. The solid solubility limits

of Fe and Ce in aluminum were extrapolated from data available in the literature^{17,18} to be approximately 0.0011 at.% Fe and 0.00017 at.% Ce at 425°C. The bulk diffusivities of Fe in Al¹⁹ and Ce in Al²⁰ were reported as $0.12 \times 10^{-4} \exp(-16.2 \times 10^3/T) \text{ m}^2/\text{s}$ and $1.9 \times 10^{-10} \exp(-13.3 \times 10^3/T) \text{ m}^2/\text{s}$, respectively. A value for the grain boundary diffusion of Fe in Al was obtained from the work of Hirano²¹ et al.: $D_G = 5.0 \times 10^{-6} \exp(-7.04 \times 10^3/T) \text{ m}^2/\text{s}$. No information was available regarding grain boundary diffusion of Ce in Al. A general expression was proposed by Gjostein²² for diffusion of solute along undissociated dislocations: $D_p = 3.0 \times 10^{-5} \exp(-8.9 T_m/T) \text{ m}^2/\text{s}$. The grain boundary width was taken to be $5 \times 10^{-10} \text{ m}$ and the grain size was taken to be 1 micrometer. For calculating the transverse section of a dislocation pipe, a radius of $5b$ was used where b is the Burgers vector. The number of dislocations attached to each particle was left as a variable. For all calculations, a typical particle-matrix interfacial energy of 1 J/m^2 was assumed.

Table I compares experimentally measured growth rates and growth rates predicted by the three models. The table indicates that bulk diffusion of neither Fe nor Ce in Al is sufficiently rapid to account for the observed particle growth rates according to the B-W modified LSW theory. The measured particle growth rate is 140 times faster than the predicted rate of growth by bulk diffusion of $\text{Al}_{13}\text{Fe}_4$ particles and 10^5 times faster than the predicted rate of growth of $\text{Al}_{10}\text{Fe}_2\text{Ce}$ particles. Kirchner's model predicts an $\text{Al}_{13}\text{Fe}_4$ particle growth rate similar to the measured growth rate. (The range of calculated values for growth by this mechanism reflects the slowly changing value of γ as the particles increase in size.)

In order for the measured rate constant for growth by diffusion along dislocation pipes to be equal to the predicted growth rate, the calculation

suggests that the average particle must have 85 dislocations attached to it. Although careful examination of the TEM micrograph of Fig. 1(a) shows a smaller number of dislocations, the contribution from pipe diffusion cannot be dismissed, especially for the case of particles not sited on grain boundaries. Some dislocations which were present in the volume surrounding a particular particle are lost in foil preparation or are missed in TEM observation. Furthermore, if the effect of overlapping diffusion fields is taken into account, the number of dislocations required to make the measured and calculated growth rates equal would decrease.

In the absence of deformation, the dislocation density will decrease during aging. Hence, the contribution of pipe diffusion to coarsening becomes less important at long times. The TEM micrograph of the specimen aged 240 hrs at 425°C (Fig. 1(b)) shows fewer dislocations and fewer fine particles in grain interiors than the micrograph of the specimen aged 24 hrs at 425°C (Fig. 1(a)).

B. Effect of Elevated Temperature Deformation on the Particle Coarsening Rates

It is well known that the imposition of plastic deformation can increase the coarsening rate of second phase particles in metals if the mechanism for growth is bulk diffusion. Bulk diffusivity, D_v , is given by

$$D_v = D_0 C_v \exp(-Q/RT) \quad [6]$$

where D_0 is a constant, C_v is the concentration of vacancies, and Q is the energy of motion for the interchange of a diffusing atom with a vacancy. Any excess vacancies generated during deformation would thus enhance the diffusivity and consequently the particle coarsening rate. Further, any increase in dislocation density would increase the likelihood for pipe diffusion. It is important for application of an elevated temperature alloy that coarsening

kinetics both under no load and under static and dynamic loads be examined for they may be substantially different. In addition, such studies may help confirm the rate controlling mechanism for Ostwald ripening besides being of theoretical interest themselves.

Preliminary creep experiments indicated that creep deformation enhances coarsening kinetics in this alloy. Low test temperatures were selected because these had the best chance of showing an effect of creep on the coarsening rate. Table II lists creep conditions and measurements of particle mean intercept lengths in deformed and undeformed regions of five specimens. In all 5 cases creep deformation led to larger particle sizes. The first two specimens were unloaded after 50 hrs and examined. The last three specimens failed before this time and sections away from the fracture surface were examined. For all specimens, the degree of enhanced growth is comparable. The TEM micrographs of Fig. 4 represent deformed and undeformed regions of specimen 2.

Results of microhardness measurements for a series of specimens aged, crept or fatigued at 425°C are given in Fig. 5. The effect of imposed creep on the Al-Fe-Ce alloy is to markedly soften the material in comparison to pure isothermal annealing with the initial creep having the largest effect. Fatigue initially hardens the material but then softens it at about the same rate as isothermal annealing or creep.

Figure 6 shows that volume fractions of the dispersed phases remain reasonably constant in the specimens annealed, crept or fatigued. A truly constant volume fraction indicates coarsening without additional nucleation. The change of mean particle intercept length with time for the specimens of Fig. 6 are given in Fig. 7.

Particle mean intercept lengths in crept specimens are larger than in specimens isothermally annealed for the same length of time. On the other

hand, intercept lengths in fatigued specimens are somewhat smaller than in specimens isothermally annealed for the same length of time. As shown in Table IV, increasing the hold time at the maximum tensile stress of specimens fatigued for a fixed time increases the mean particle intercept length.

TEM observation of thin foil specimens showed dislocations connecting dispersed particles. While no quantitative measurements of dislocation density were undertaken, the incidence of dislocations connecting particles appeared to be more frequent in the crept specimens and hold time fatigue specimens than in specimens fatigued with no hold period. Figure 8 shows a TEM micrograph of a thin foil of the Al-8.8Fe-3.7Ce specimen fatigued 120 hrs at 425°C with a hold period of 15 seconds.

Three mechanisms may be considered in an attempt to explain these observations on the effect of deformation on coarsening: (1) generation of excess vacancies by plastic deformation, (2) short circuiting of diffusion along dislocations and (3) fine particle precipitation during fatigue.

As already mentioned, plastic deformation can increase the vacancy concentration above the equilibrium value. In a recent study of coarsening of β' -NiAl particles in a large grain iron base alloy, Calderon, Weertman and Fine²³ found that fatigue deformation substantially increased the β' particle growth rates. The coarsening behavior suggested that bulk diffusion was the principal mechanism responsible for growth of the particles, and that generation of excess vacancies during fatigue caused the acceleration in ripening during cyclic stressing. In the present case, the calculations presented in Table I indicate that it is unlikely that an increase in bulk diffusion controlled coarsening during deformation is responsible for the observed changes. The vacancy concentration would have to increase by more than two orders of magnitude to bring the bulk diffusion growth rate up to the measured value.

AD-A164 158

SYNTHESIS AND PROPERTIES OF ELEVATED TEMPERATURE P/M
ALUMINUM ALLOYS(U) NORTHWESTERN UNIV EVANSTON IL DEPT
OF MATERIALS SCIENCE AND E... H E FINE ET AL. 30 NOV 85

2/2

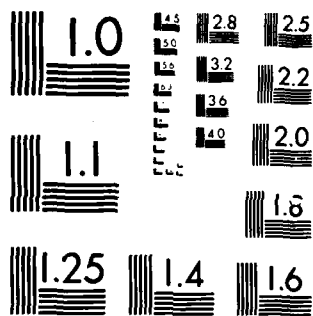
UNCLASSIFIED

AFOSR-TR-85-1258 AFOSR-82-0085

F/G 11/6

NL





MICROCOPY RESOLUTION TEST CHART
NATIONAL BUREAU OF STANDARDS 1963-A

However, the influence of excess vacancies on grain boundary diffusion may be responsible for the effect of creep deformation on coarsening in this fine grain alloy. The increase in dislocation density produced by deformation may also lead to accelerated ripening through a more significant contribution to coarsening from pipe diffusion.

At first sight it appears that while static deformation promotes ripening, particle growth in the Al-Fe-Ce alloy actually is retarded by cyclic stressing (Fig. 7). However, as seen from Fig. 5, fatiguing initially leads to an increase in hardening, which is followed by continuous softening. Only softening is observed in the cases of aging and creep deformation. It is known that fatigue deformation at elevated temperature can quickly cause additional precipitation of fine particles along dislocation lines. Whereas prolonged aging or static stressing produced little or no such effect (e.g., see reference 24). Such fine particles along dislocation lines were seen in micrographs of crept Al-Fe-Ce alloy, as illustrated in Fig. 9. They are suggested to be even a greater factor in fatigue in the absence of hold at maximum stress. These fine precipitates would increase the hardness and, because they are small, depress the average particle size. Meanwhile, deformation enhanced coarsening is taking place concurrently, and as the additional precipitation ceases the value of \bar{L} rises. Note that the fatigue datum point for \bar{L} at 120 hrs in Fig. 7 corresponds to a test run at only one half the stress amplitude used for the 6 and 60 hr tests. It is reasonable to expect that the value of \bar{L} at 120 hrs would have been even higher if the larger stress amplitude had been used. The new precipitates are so small that they contribute little to the particle volume fraction, which appears to remain substantially unchanged (Fig. 6).

The dislocation density was observed to be lower in the continuously fatigued specimens than in the crept specimens or in specimens fatigued with

a hold time. Therefore, it might be concluded that pipe diffusion would play a smaller role in the coarsening of the particles in fatigued material. It is likely that there is a substantial annihilation of dislocations during every fatigue cycle, hence the lower density seen in the micrographs. However, the fact that the fatigue strain rate was 10^3 times the creep rate indicates that during much of the fatigue cycle the dislocation density must be at least as great as during creep. (It is difficult to estimate the relative magnitudes of the dislocation density under the two types of loading because such quantities as the internal stress, the stress dependence of the dislocation velocity, and the ratio of mobile to immobile dislocations are not known.) An estimate can be made of the time t required for solute to travel from one particle to another by pipe diffusion. This time is of the order $t = \lambda^2/D_p$, where λ is the average spacing between particles and D_p is the diffusivity of solute along dislocation pipes. The value of λ may be obtained from a knowledge of \bar{L} and the average particle volume fraction. When the value of \bar{L} is 2×10^{-7} m, $\lambda = 3 \times 10^{-7}$ m. At 425°C the diffusivity along dislocation pipes, according to the expression already cited by Gjostein²², is 2×10^{-10} m²/s. Thus the time for solute to travel from one particle to another is about 5×10^{-4} s. Since this is a very short time compared to the fatigue cycle period, solute can be transported from one particle to another along a dislocation line during the time between its creation and annihilation within a single cycle. Thus it can be concluded that pipe diffusion may contribute to particle growth during fatigue despite the periodic annihilation of a significant fraction of the dislocation population.

IV. CONCLUSIONS

1. Solute diffusion along dislocations and grain boundaries are the predominant mechanisms for coarsening of the $Al_{13}Fe_4$ and $Al_{10}Fe_2Ce$ particles during isothermal annealing of the rapidly solidified Al-8.8Fe-3.7Ce alloy at 425°C. The contribution from pipe diffusion may be relatively more important for short aging times.
2. Crept material softens more rapidly than material aged under no load at the same temperature. At least one cause of the softening is an enhanced rate of particle coarsening.
3. Cyclic stressing has a much smaller effect than creep on the alloy hardness and particle coarsening rates during the initial stages of deformation.
4. Several fundamental questions remain regarding the mechanism for the effects of creep and fatigue deformation on coarsening of incoherent dispersed particles.

ACKNOWLEDGEMENTS

The authors are grateful for the support of this work by the Air Force Office of Scientific Research through Grant No. AFOSR-82-0005B. In this research extensive use was made of the facilities of Northwestern University's Materials Research Center, supported in part under the NSF-MRL program (Grant No. DMR82-16972). One of the authors (LA) would like to thank the Zonta Organization for their gift of an Amelia Earhart Fellowship Award. The alloys were kindly provided by the Air Force Materials Laboratory through Ms. S. Kirchoff and Dr. W. M. Griffith, Jr. We thank Dr. G. J. Hildeman of Alcoa Technical Center for the many helpful discussions during the course of the research.

REFERENCES

1. W. M. Griffith, Jr., R. E. Sanders, Jr. and G. J. Hildeman: High Strength Powder Metallurgy Aluminum Alloys, M. J. Koczak and G. J. Hildeman, eds., Conf. Proceedings, TMS-AIME, 1982, p. 209.
2. R. W. Balluffi and A. L. Ruoff: J. Appl. Phys., 1963, vol. 34(6), p. 1634.
3. R. W. Balluffi and A. L. Ruoff: J. Appl. Phys., 1963, vol. 34(7), p. 1848.
4. R. W. Balluffi and A. L. Ruoff: J. Appl. Phys., 1963, vol. 34(9), p. 2862.
5. L. Angers, M. E. Fine and J. R. Weertman: Northwestern University, Evanston, IL, unpublished research, 1985.
6. E. E. Underwood: in Quantitative Stereology, Addison-Wesley Pub. Co., Reading, MA, 1970, pp. 25-35.
7. I. M. Lifshitz and V. V. Slezov: J. Phys. Chem. Solids, 1961, vol. 19, p. 35.
8. C. Wagner: Z. Elektrochem., 1961, vol. 65, p. 581.
9. H. O. K. Kirchner: Metall. Trans. A, 1971, vol. 2, p. 2861. Also see I. Pontikakos and H. Jones: Metal Sci., 1982, vol. 16, p. 27.
10. M. V. Speight: Acta Metall., 1968, vol. 16, p. 133.
11. H. Kreye: Z. Metallkunde, 1970, vol. 61, p. 108.
12. M. E. Fine: Northwestern University, Evanston, IL, unpublished research, 1985.
13. A. D. Brailsford and P. Wynblatt: Acta Metall., 1979, vol. 27, p. 489.
14. L. Angers: Ph.D. thesis, Northwestern University, Evanston, IL, 1985.
15. P. J. Black: Acta Cryst., 1955, vol. 8, p. 43, 175.
16. L. Angers, M. E. Fine, M. Raghavan and J. R. Weertman: Northwestern University, Evanston, IL and Exxon Res. & Eng. Co., Annandale, NJ, unpublished research, 1985.
17. L. A. Willey: in Aluminum: Properties, Physical Metallurgy and Phase Diagrams, K. R. Van Horn, ed., ASM, Metals Park, OH, 1967, pp. 359-396.
18. L. F. Mondolfo: in Aluminum Alloys - Structure and Properties, Butterworth Publishers Inc., Boston, MA, 1972, p. 242.
19. K. Sorenson and G. Trumpy: Phys. Rev. B1, 1973, vol. 7, p. 1791.

REFERENCES (Contd.)

20. S. P. Murarka and R. P. Agarwala: Indian Atomic Energy Commission Rept. BARC-368, 1968.
21. K. I. Hirano, R. P. Agarwala and M. Cohen: Acta Metall., 1962, vol. 10, p. 857.
22. N. A. Gjostein: in Diffusion, ASM, Metals Park, OH, 1973, p. 241.
23. H. A. Calderon, J. R. Weertman and M. E. Fine: Scripta Metall., 1984, p. 249.
24. W. B. Jones and J. A. Van Den Avyle: Metall. Trans. A, 1980, vol. 11A, p. 1275.

Table I. Comparison of Growth Rates Measured in the RSP P/M Al-8.8Fe-3.7Ce Alloy at 425°C and Growth Rates Calculated for Bulk Diffusion Controlled Coarsening (n=3), Coarsening by Diffusion Along Grain Boundaries (n=4), and Coarsening by Diffusion Along Dislocation Pipes (n=5)

Exponent, n	Measured K ($\mu\text{m}^n/\text{hr}$)	Calculated K Al ₁₃ Fe ₄ ($\mu\text{m}^n/\text{hr}$)	Calculated K Al ₁₀ Fe ₂ Ce ($\mu\text{m}^n/\text{hr}$)
3	5.7×10^{-5}	4.1×10^{-7}	4.2×10^{-10}
4	2.3×10^{-4}	1.5×10^{-4} to 2.3×10^{-4}	-
5	3.5×10^{-6}	$4.1 \times 10^{-8} \times z^{\dagger}$	-

[†] z is the average number of dislocation lines attached to a particle

Table II. Creep Conditions and Measured Values of Mean Particle Intercept Length for Crept Al-8.8Fe-3.7Ce Specimens

Specimen	Creep Conditions	Mean Particle Intercept Length* (μm)
1	316°C, 32.7 MPa, 60 hr deformed region	$0.29 \pm .02$
	undeformed region	$0.19 \pm .02$
2	425°C, 17.2 MPa, 60 hr deformed region	$0.47 \pm .07$
	undeformed region	$0.40 \pm .04$
3	375°C, 32.7 MPa, 43 hr deformed region	$0.35 \pm .05$
	undeformed region	$0.28 \pm .03$
4	425°C, 32.7 MPa, 0.74 hr deformed region	$0.36 \pm .07$
	undeformed region	$0.26 \pm .04$
5	375°C, 68.2 MPa, 0.23 hr deformed region	$0.21 \pm .03$
	undeformed region	$0.17 \pm .02$

* \pm refers to 95% confidence intervals about the mean value

Table III. Values of Mean Particle Intercept Length in the Al-8.8Fe-3.7 Ce RSP Alloy after Isothermal Annealing, Creep and Fatigue at 425°C

Time (hrs)	Mean Intercept Length (μm)			
	Isothermal Annealing	Creep (17.2MPa)	Fatigue $\Delta\sigma/2 = 34.4\text{MPa}$	Fatigue $\Delta\sigma/2 = 68.8\text{MPa}$
6	-	-	-	0.19 + .02
24	0.17 \pm .01	0.33 \pm .04	-	-
60	0.24 \pm .01	0.47 \pm .07	-	0.21 \pm .01
120	0.34 \pm .04	0.57 \pm .06	0.27 \pm .03	-
168	0.35 \pm .02	-	-	-
240	0.37 \pm .02	0.58 \pm .03	-	-

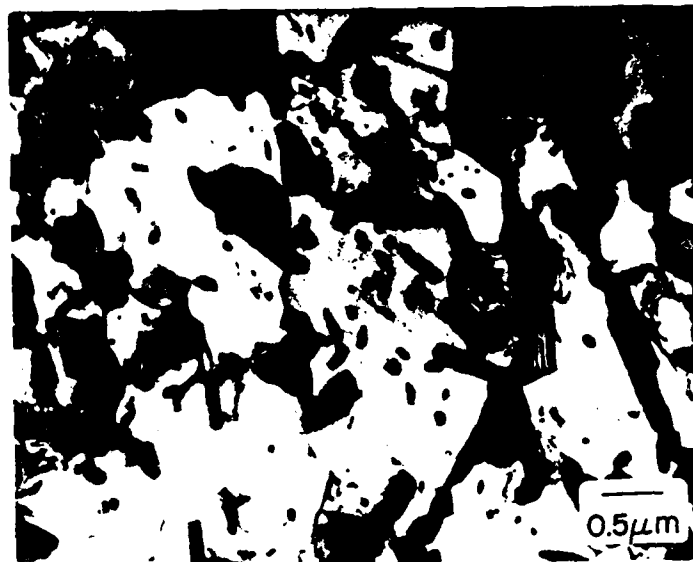
Table IV. Mean Particle Intercept Lengths in Al-8.8Fe=3.7Ce Specimens Deformed 120 Hrs at 425°C

Stress Amplitude (MPa)	Hold Time* (s)	Mean Particle Intercept Length (μm)
17.2	15	0.27 \pm 0.02
17.2	120	0.32 \pm 0.04
17.2	4.32 $\times 10^5$	0.57 \pm 0.06

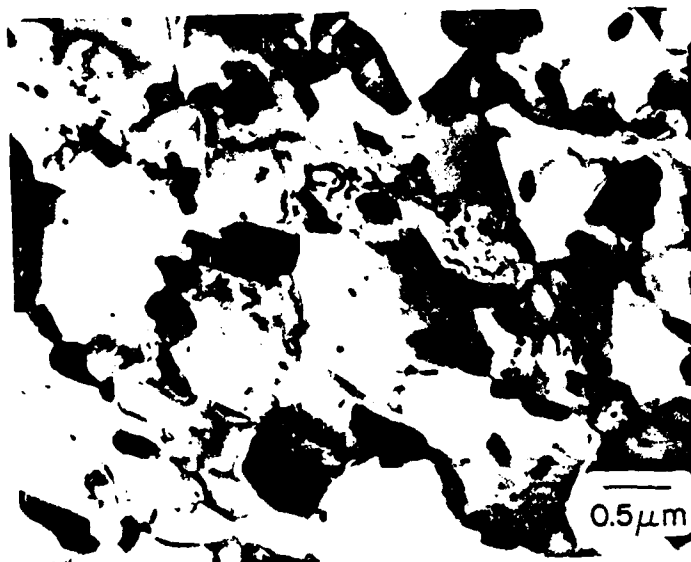
* at peak tensile stress

FIGURE CAPTIONS

- Figure 1. TEM micrographs of thin foils of Al-8.8Fe-3.7Ce specimens isothermally annealed at 425°C for (a) 24 hrs and (b) 240 hrs.
- Figure 2. Mean particle intercept length, \bar{L} , versus aging time for the isothermally annealed Al-8.8Fe-3.7Ce specimens.
- Figure 3. Grain size, d , versus aging time for the isothermally annealed Al-8.8Fe-3.7Ce specimens.
- Figure 4. TEM micrographs of replicas of Al-8.8Fe-3.7Ce specimen crept 60 hrs at 425°C under an initial stress of 17.2 MPa: (a) undeformed region and (b) deformed region.
- Figure 5. Vickers microhardness versus aging time for the isothermally annealed, crept and fatigued Al-8.8Fe-3.7Ce specimens.
- Figure 6. Volume fraction of the dispersed phases versus aging time for the isothermally annealed, crept and fatigued Al-8.8Fe-3.7Ce specimens.
- Figure 7. Mean particle intercept length, \bar{L} , versus aging time for isothermally annealed, crept and fatigued Al-8.8Fe-3.7Ce specimens.
- Figure 8. TEM micrograph of thin foil specimen of Al-8.8Fe-3.7Ce fatigued with a hold period of 15 seconds. Dislocations are seen connecting dispersed phase particles.
- Figure 9. TEM micrograph of an Al-8.8Fe-3.7Ce specimen crept 96 hrs at 425°C under an initial stress of 25 MPa illustrating region where dislocations are seen connecting dispersed phase particles.



(a)



(b)

Fig. 1. TEM micrographs of thin foils of Al-8.8Fe-3.7Ce specimens isothermally annealed at 425°C for (a) 24 hrs and (b) 240 hrs.

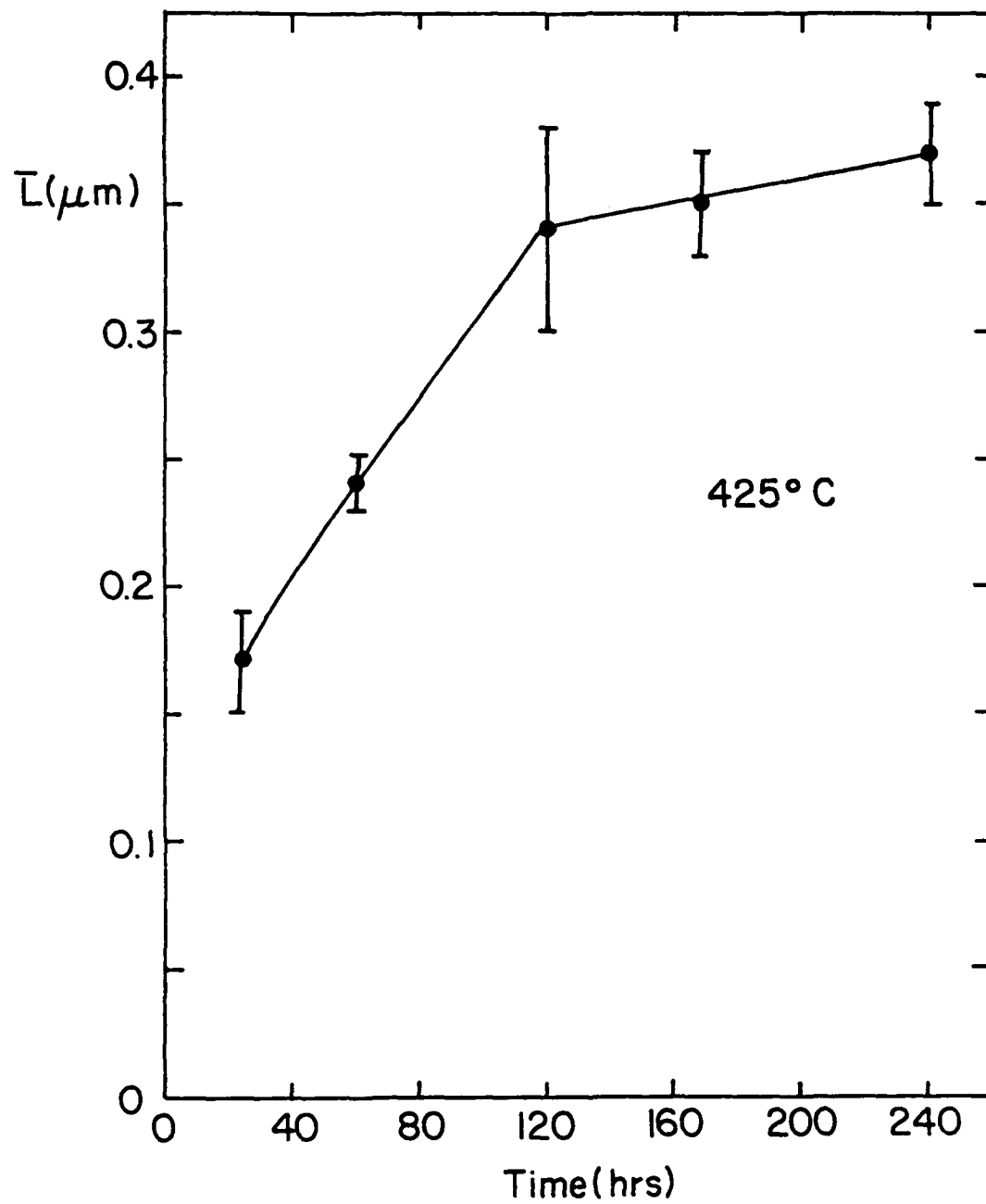


Fig. 2. Mean particle intercept length, \bar{L} , versus aging time for the isothermally annealed Al-8.8Fe-3.7Ce specimens.

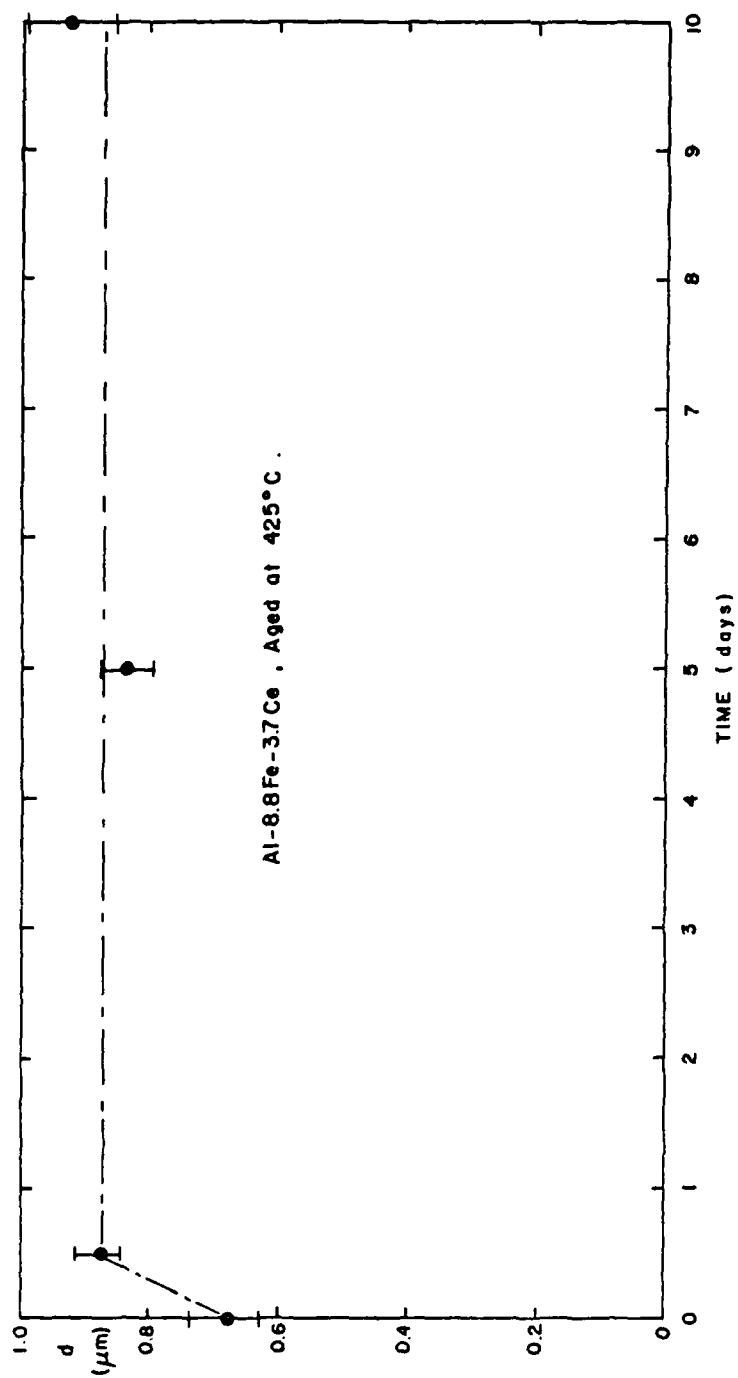
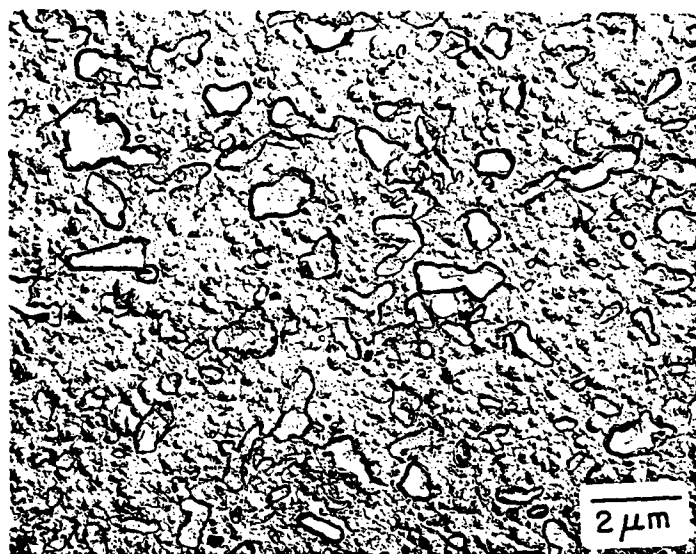


Fig. 3. Grain size, d , versus aging time for the isothermally annealed Al-8.8Fe-3.7Ce specimens.



(a)



(b)

Fig. 4. TEM micrographs of replicas of Al-8.8Fe-3.7Ce specimen crept 60 hrs at 425°C under an initial stress of 17.2MPa: (a) undeformed region and (b) deformed region.

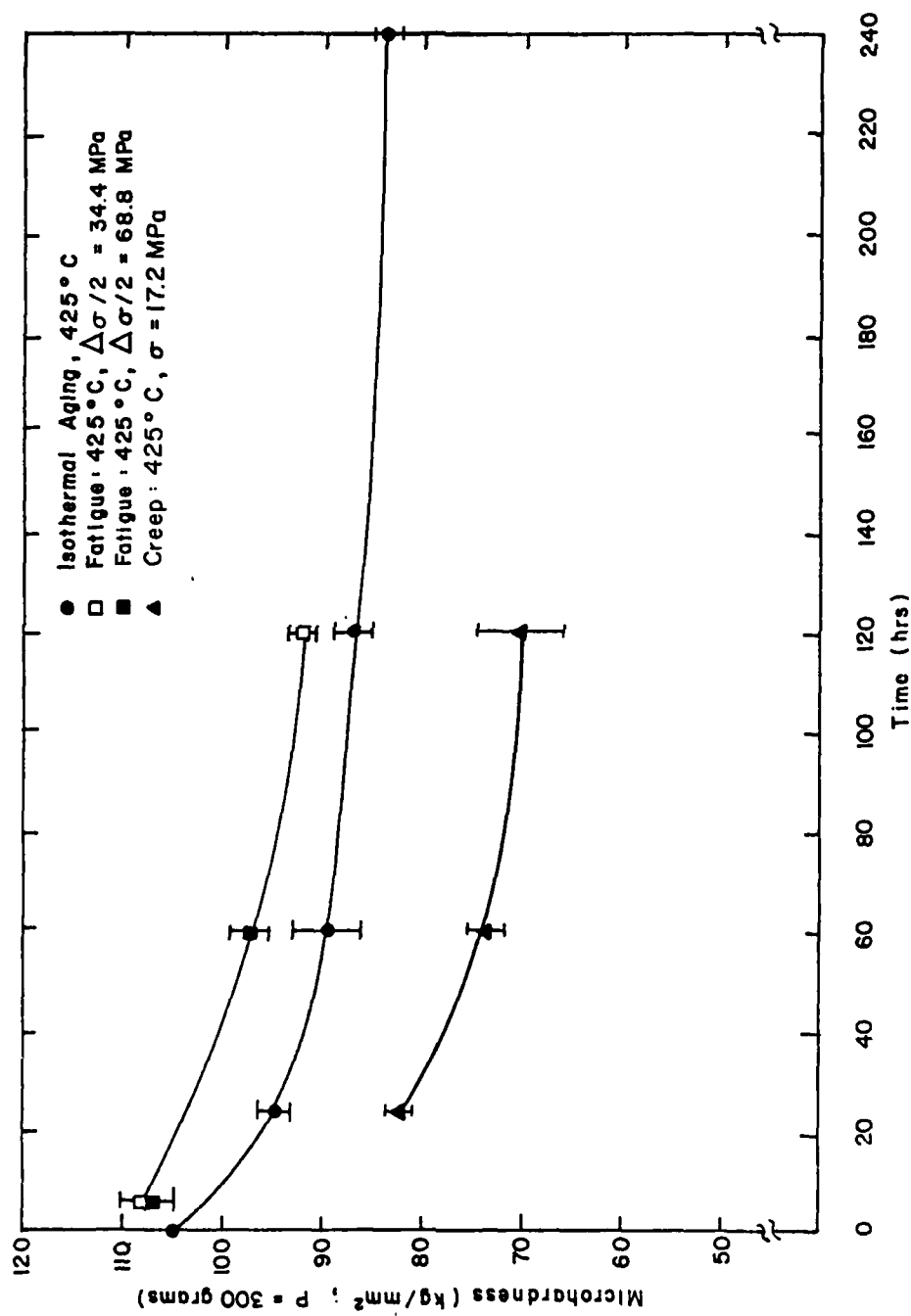


Fig. 5. Vickers microhardness versus aging time for the isothermally annealed, crept and fatigued Al-8.8Fe-3.7Ce specimens.

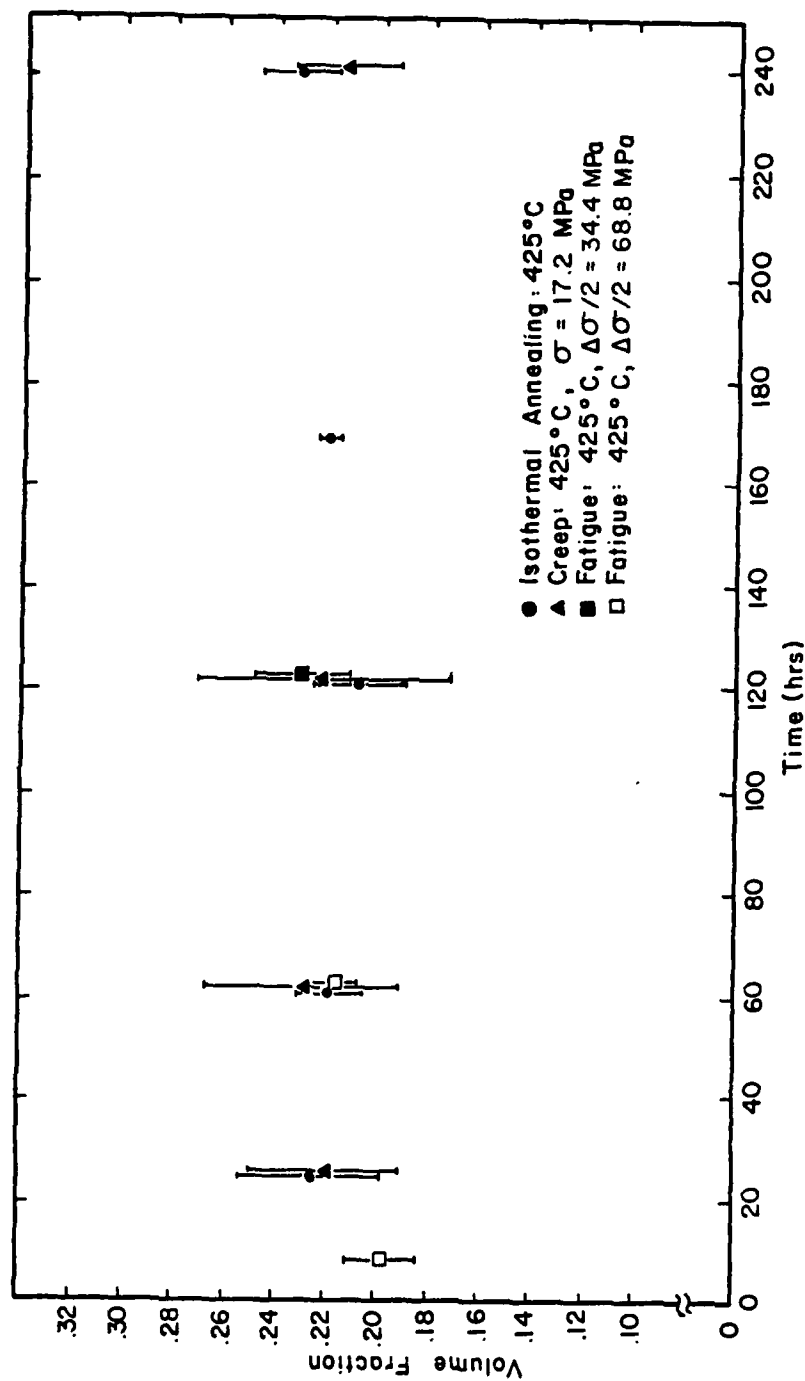


Fig. 6. Volume fraction of the dispersed phases versus aging time for the isothermally annealed, crept and fatigued Al-8.8Fe-3.7Ce specimens.

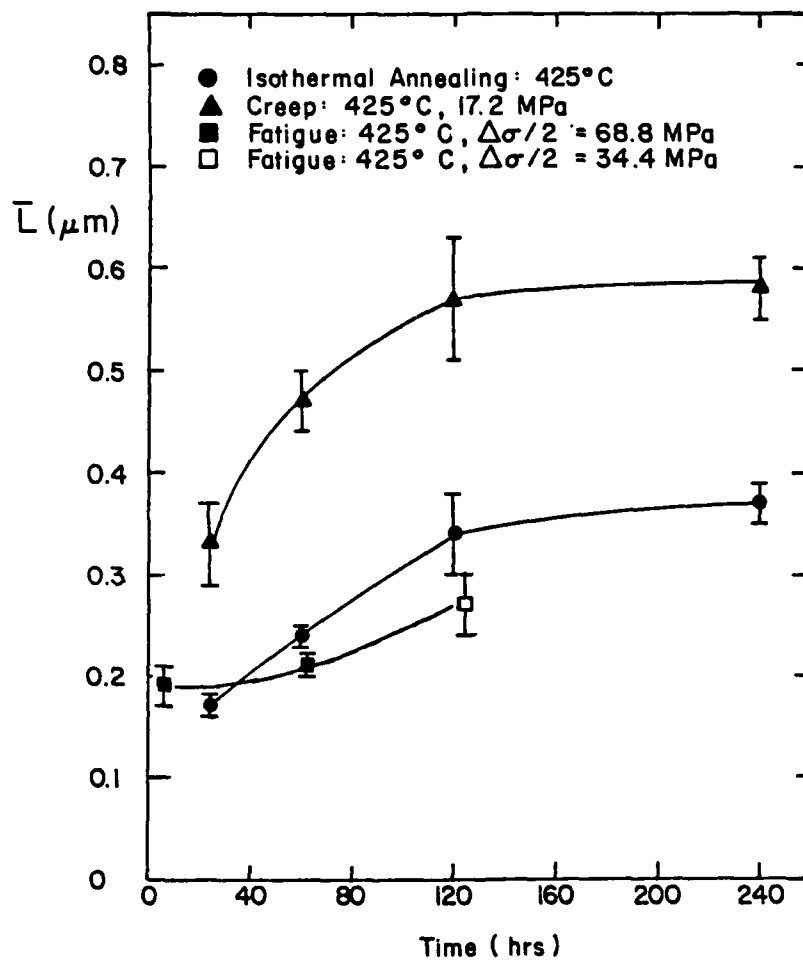


Fig. 7. Mean particle intercept length, \bar{L} , versus aging time for isothermally annealed, crept and fatigued Al-8.8Fe-3.7Ce specimens.

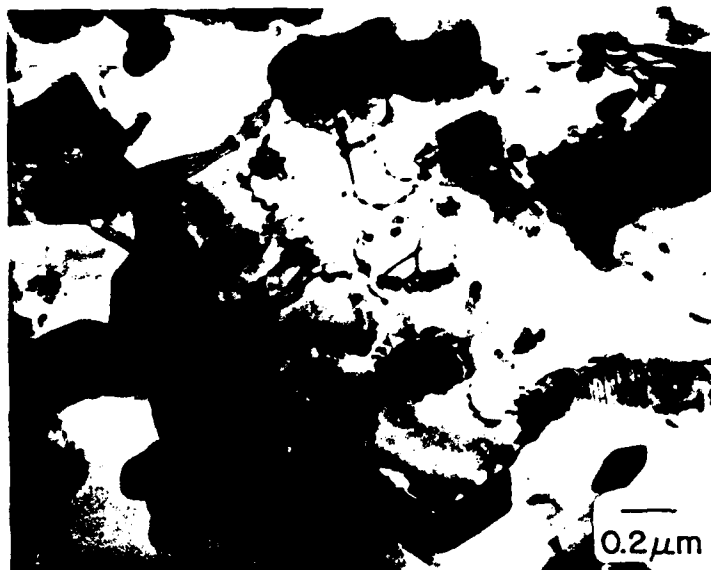


Fig. 8. TEM micrograph of thin foil specimen of Al-8.8Fe-3.7Ce fatigued with a hold period of 15 seconds. Dislocations are seen connecting dispersed phase particles.

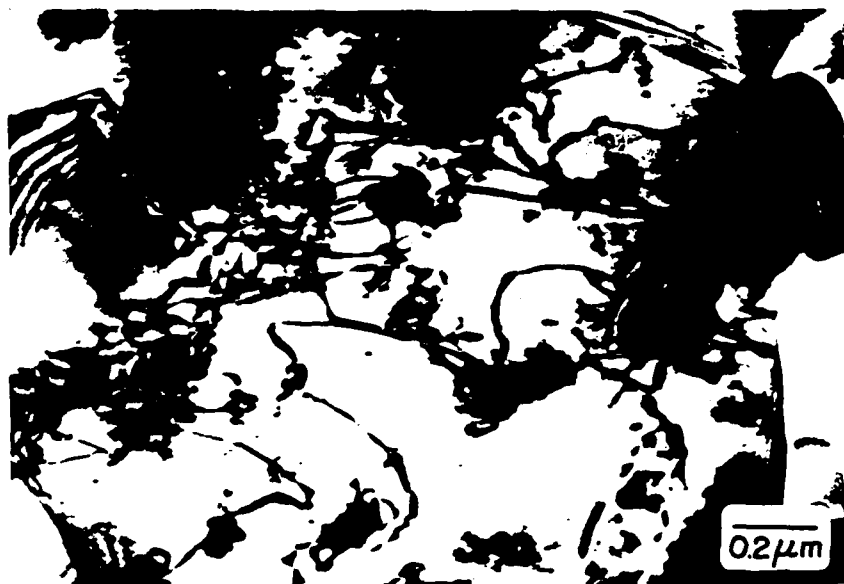


Fig. 9. TEM micrograph of an Al-8.8Fe-3.7Ce specimen crept 96 hrs at 425°C under an initial stress of 25 MPa illustrating region where dislocations are seen connecting dispersed phase particles.

LIST OF PROFESSIONAL PERSONNEL WHO PARTICIPATED IN THE RESEARCH

Principal Investigators

Morris E. Fine, Walter P. Murphy Professor of Materials Science and Engineering

Julia R. Weertman, Professor of Materials Science and Engineering

Research Fellow

S. I. Kwun, 9/1/83 - 8/16/84 ($\frac{1}{2}$ time)

Postdoctoral Research Associate

J. L. Horng, 7/1/84 - 11/30/84

Graduate Students

T. R. Wilkinson - Completed M.S. June 1984. Now at Rexnord Corporate Research and Innovation Group, Milwaukee, Wisconsin.

M. V. Ghatge - Completed M.S. June 1985. Currently Ph.D. student at Rensselaer Polytechnical Institute, Troy, New York.

M. S. Zedalis - Completed Ph.D. June 1985. Now at Allied Corporation, Morristown, New Jersey.

L. Angers - Completed Ph.D. August 1985. Now at Alcoa Technical Center, Alcoa Center, Pennsylvania.

Y. Chen, Ph.D. student - Research topic: precipitation and coarsening of Al-Zr-V alloys.

Secretary

J. Bell ($\frac{1}{2}$ time)

DISSERTATIONS

1. "The Coarsening of the Dispersed Phase in an Al-Fe-Mo-V Alloy", T. R. Wilkinson, M.S. awarded June 1984.
2. "The Effect of Variation of Volume Percent Intermetallic on the Elastic Modulus of Al-Al₃Zr Alloys as Measured by an Ultrasonic Technique", M. V. Ghatge, M.S. awarded June 1985.

DISSERTATIONS (Continued)

3. "Development of an Elevated Temperature Aluminum Alloy Containing Al_3X -type Dispersed Phases", M. S. Zedalis, Ph.D. awarded June 1985.
4. "Particle Coarsening in Rapidly Solidified Al-Fe-Ce Alloys", L. Angers, Ph.D. awarded August 1985.

END

FILMED

386

DTIC